Friedrich-Alexander-Universität
Naturwissenschaftliche Fakultät

Evidence of accretion in quiescence in Be X-ray binaries

Master's Thesis in Physics

Presented by
Nicolas Zalot
October 20, 2024

Dr. Karl Remeis-Sternwarte, Bamberg
Erlangen Centre for Astroparticle Physics
Friedrich-Alexander-Universität Erlangen-Nürnberg

Erlangen Centre for Astroparticle Physics

Supervisor: Prof. Dr. Jörn Wilms

Contents

List of Figures

List of Tables

You should think about the consequence
of your magnetic field bein' a little too strong
– Swift T. A., 2017

Abstract

The X-ray spectra of pulsars in Be X-ray binary systems at luminosities below $\sim 10^{34}\,\mathrm{erg\,s^{-1}}$ show a fundamentally different spectral shape than at higher luminosities associated with outbursts. In this low luminosity state, the observed X-ray spectra show a double-hump spectral shape. Theoretical works suggest that it consists of a thermal component in the soft X-ray band and a nonthermal component extending beyond 100 keV, on which deep cyclotron resonant scattering features are imprinted.

In this work I aim to collect a sample of X-ray spectra of high-mass X-ray binaries harboring neutron stars in the quiescent state exhibiting a double-hump shape. For the selected spectra I intend to obtain an empirical description of the X-ray spectrum, in particular the nonthermal component. I further aim to obtain a method to estimate the magnetic field strength based on the position of the two components and compare the obtained empirical relation with theoretical predictions.

I select eight observations of Be X-ray binaries and apply an empirical spectral model, which consists of a cutoff powerlaw for the thermal component and Wien hump $\propto E^2 \exp\left(-E/k_\mathrm{B}T\right)$ for the nonthermal component. I determine the intersection energy at which the two components' spectral contribution is equal, forming the basis for further investigation of its relation to the cyclotron line energy. For comparison, quiescent spectra with varying magnetic field strengths are simulated based on the physical model for emission at low mass-accretion rates (`polcap`), to which the same empirical model is applied.

I present a new method to estimate the magnetic field strength in accreting pulsars complementary to the well-known cyclotron lines. I show that there exists a positive correlation between the intersection energy and the cyclotron line energy.

For four sources with known cyclotron lines a linear relation between the two quantities is determined. For the simulated spectra, a broken linear model describes the relation well. Overall, the relations determined from theory and observations yield similar results. With the method presented in this work, magnetic field strengths can be estimated from observations with far less requirements on well-constrained data at high energies, even allowing to probe the magnetic field of accreting pulsars with observations in which no cyclotron lines are found.

1 | Introduction

Accreting neutron stars have been observed and studied in various regimes. While less sensitive past X-ray observatories primarily focused on bright sources, each new generation of observatories was able to observe less bright X-ray sources with ever more increasing sensitivity. In recent years therefore a part of the scientific community commenced the hunt for X-ray binaries at low luminosities, about which far less was known than about bright transient outbursts and persistent sources. Both theoretical works and observations of such sources have shown that the X-ray spectrum fundamentally changes in the quiescent state, where a simple powerlaw with high-energy cutoff fails to reproduce the broadband X-ray spectrum. Instead, the spectrum shows a wave-like double-hump structure, which theoreticians separate into a thermal component forming deep within the neutron star's atmosphere and a nonthermal component forming in the optically thin, hot layers of the atmosphere at temperatures of 10^7–10^8 K.

Regardless of their luminosity state, X-ray spectra often also contain apparent absorption features associated with quantisation of electron momenta in the present strong magnetic field, that allow to measure the magnetic field strength near the surface, which are called cyclotron lines. They are often present at energies between 10–100 keV and often only directly detectable up to ~60 keV with the space-based X-ray observatory *NuSTAR*, which is often the choice of instrument for broadband spectral analyses of accreting X-ray pulsars due to its large spectral range from 3.5–79 keV. Therefore, both strong magnetic fields, resulting in high cyclotron line energies, and background-dominated observations in quiescence hinder the investigation of the magnetic field strength with *NuSTAR* – a problem that I intend to address in the present work.

In this work, I focus on low luminosity observations of high-mass X-ray binaries harboring accreting pulsars and investigate their X-ray spectra and pulse profiles under various aspects. The goal of this work is to characterise the double-hump X-ray spectra sufficiently well to be able to estimate the magnetic field strength near the neutron star's surface and develop a reliable tool to estimate it without the need to measure it indirectly via cyclotron lines.

To this end, I will revisit empirical and physical models utilized for the description of their broadband X-ray spectra and apply them to a selected sample of sources. Finally, I investigate the relation between parameters of the obtained spectral model and the cyclotron line energy and characterise it with simple mathematical models. The same analysis strategy is applied to simulated spectra based on the `polcap` model developed by Sokolova-Lapa et al. (2021) in order to compare experimental and theoretical results and investigate whether they predict a similar relation between spectral shape and magnetic field strength.

2 | Theoretical foundation

In the following, I briefly introduce the general properties and history of accreting pulsars with high-mass companions, as well as the theoretical concepts that form the basis for this work. In Section 2.1, I introduce compact objects in general before focusing on such objects in binary systems in Sect. 2.2. Thereafter, I briefly describe the formation process of neutron stars in Sect. 2.3. In Sect. 2.4, I present the general properties and formation of high mass X-ray binaries harboring magnetized neutron stars. The accretion process in general is introduced in Sect. 2.5, before I focus on the spectral formation in Sect. 2.6. In Sect. 2.7, I discuss phenomenological and physical models typically used to describe the X-ray spectra of accreting neutron stars. Lastly, in Sect. 2.8, I introduce X-ray pulse profiles of accreting pulsars.

2.1 Compact objects

Before the age of satellite-based observational astronomy, compact objects were only a subject of theoretical research; in 1784 Michell postulated the existence of spherical objects of solar density with radii of $\sim 500\,R_{\odot}$. Such objects are obviously not what one would call *compact*, but they have the interesting property that the velocity required to overcome the gravitational pull of the object, the escape velocity, exceeds the speed of light. Michell (1784) argued that such objects could therefore emit no radiation and named them *dark stars*.

More than 100 years later, the theory of general relativity (Einstein, 1916) provided a theoretical framework capable of describing such objects mathematically. In general relativity, not only massive bodies, but also massless particles such as photons are subject to the gravitational force and are deflected by them. In essence, this can be understood as the result of warping of the four-dimensional space time due to the presence of massive bodies. The mathematical field equations that describe this process were studied extensively in the 20$^{\text{th}}$ century and, eventually, solutions were found that implied the existence of bodies that curved space-time so strongly that not even light quanta could escape. Such objects are known today as *black holes*. Although no radiation within the event horizon, a theoretical sphere surrounding the black hole, can escape, the environment surrounding black holes nevertheless emits electromagnetic radiation and particles due to different processes; Hawking (1975) showed that particles and their respective anti-particles can form near the event horizon of a black hole. The intensity of this radiation is, however, much too low to be detectable with current technology.

Black holes can be observed via interplay with a companion star in binary system. Black holes are classified based on their key parameter, their mass. Stellar black holes have masses on the order of few $M_{\odot}$, whereas supermassive black holes often found in the center of galaxies have masses of $\sim 10^6\,M_{\odot}$ or more (see, e.g., Schödel et al., 2002).

Another type of compact object, the prime focus of this thesis, are neutron stars. Following the discovery of the neutron by Chadwick in 1932, Baade & Zwicky (1934) tentatively suggested that regular stars transform into neutron stars during supernova explosions at the end of their lives. As discussed in detail by Yakovlev et al. (2013), Landau (1932) also pondered the concept of extremely dense stars that resemble one giant nucleus. Yakovlev et al. (2013) argue that the discussion that supposedly led to Landau's paper must have taken place in March 1931 – even before the discovery of the neutron. The first indirect observation of neutron stars was achieved few decades later, when Hewish & Okoye (1965) discovered a radio-emitting source of small angular diameter, which is today known as the Crab nebula. It is the remnant of a supernova explosion that occurred in 1054 AD, which was widely observed in China and East Asia (see, e.g., Stephenson & Green, 2003). Shortly after the detection of the radio source, Hewish's postgraduate student Jocelyn Bell detected the first source emitting pulsed radio emission (see Bell & Hewish, 1967). Hewish et al. (1968) subsequently report pulses lasting ~ 0.3 s with a repetition rate of 1.337 s. The 1974 Nobel Prize was awarded to Sir Martin Ryle and Anthony Hewish for their work in the field of radio astronomy; Ryle was awarded for his work on observations and inventions, Hewish for his role in the discovery of pulsars[1]. Bell was not awarded a Nobel Prize for her discovery.

Neutron stars and black holes alike have been found both as isolated objects and in binary systems with a second compact object or regular star, where gravitational interactions been the two bodies lead to various observable phenomena, which allow for the study of the compact object and its properties. Due to their intense emission at high energies, systems consisting of a massive-type star and compact object are known as X-ray binaries. In this thesis, I focus on neutron stars in binary systems with massive companion stars.

2.2 Binary systems

In the most general sense binary systems consist of two bodies in a gravitationally bound state. Both constituents orbit their common center of gravity, the barycenter. The dynamics of the system are determined by the masses of the constituents $m_{1/2}$ and their maximal distance from the barycenter $a_{1/2}$. They obey the relation (Hanslmeier, 2002, 323)

$$m_1 \cdot a_1 = m_2 \cdot a_2. \tag{2.1}$$

As the two objects move on ellipses with major axes $a_{1/2}$, their total separation is trivially given as the sum of the major axes

$$a = a_1 + a_2. \tag{2.2}$$

The orbital period P_{orb} of the system can be derived from the centripetal and gravitational force and is related to the total separation a via Kepler's Third Law

$$\frac{P_{\text{orb}}^2}{a^3} = \frac{4\pi^2}{G\,(m_1 + m_2)}, \tag{2.3}$$

where G is the gravitational constant. Binary systems containing two main-sequence stars are known as double stars. The Washington Double Star catalogue (Mason et al., 2001) lists more than 150 000 double star systems.

As massive stars often evolve into compact objects, binary systems can also contain one or even two compact objects. Binary systems including at least one compact component are known as degenerate systems, if both components are degenerate the system is called double degenerate. Double-degenerate systems are especially interesting for the comparably young field of gravitational wave physics: merger events of ever-faster spinning black holes (LIGO Scientific Collaboration and Virgo Collaboration, 2016) and neutron stars (LIGO Scientific Collaboration and Virgo Collaboration, 2017) emit measurable gravitational waves shortly before they collide.

[1] See https://www.nobelprize.org/prizes/physics/1974/summary/

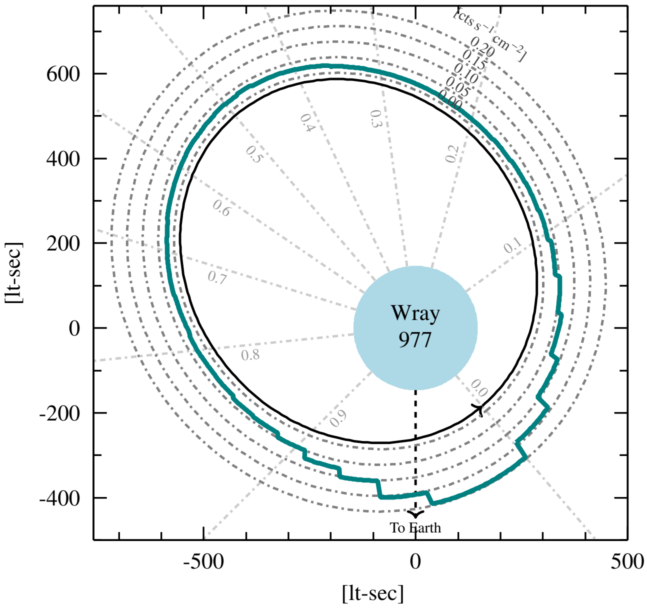

Figure 2.1: Orbital geometry of high-mass X-ray binary system GX 301−2. Shown in light blue is the hypergiant Wray 977, in black the orbit of the neutron star. The blue curve shows the orbital *Swift*/BAT rate (Krimm et al., 2013) with the notable increase in X-ray luminosity before the periastron passage, the pre-periastron flare. Orbital parameters obtained from Kaper et al. (2006), Koh et al. (1997), Leahy & Kostka (2008) and Doroshenko et al. (2010a). Figure adapted from Zalot et al. (2024).

These waves have that have been observed by the gravitational wave detectors LIGO in Hanford and Livingston.

In this work I focus on degenerate binary systems including neutron stars, where the second component is non-degenerate. They are often classified into low-mass X-ray binaries (LMXBs), where the mass of the companion star is comparable to that of the sun (i.e. $\lesssim 1\,M_\odot$) and high-mass X-ray binaries (HMXBs), where the companion is typically a star with mass typically $\gtrsim 8\,M_\odot$. As an example for the orbital geometry of a HMXB system, I show the system GX 301−2 in Fig. 2.1.

The mass of the hypergiant in this system, Wray 977, is on the order of $\sim 40\,M_\odot$ (Kaper et al., 2006), a factor of 30 higher than its neutron star companion. The neutron star orbits the barycenter on an eccentric orbit ($e = 0.462$, see Kaper et al., 2006). Before I discuss the general properties of HMXBs harboring neutron stars, it is vital to have a working understanding of the formation of neutron stars, which I briefly outline in the following.

2.3 Formation of neutron stars

At the end of their lifetime, massive stars undergo a spectacular explosion known as a supernova (SN). As supernova explosions play a vital part in the formation of neutron stars and high-mass X-ray binaries, but can be triggered by different progenitors, a way of distinguishing the types of supernovae is required. Historically, Minkowski (1941) suggested a classification of supernovae based on the presence (type II) or absence (type I) of hydrogen emission lines in their optical spectra. This classification system is still in use today, but as our knowledge of supernova processes has expanded, so too has the classification system. The subclass type Ia is associated with the explosion of white dwarf progenitors in binary systems, which undergo an explosion once their mass exceeds the Chandrasekhar limit of $\sim 1.44\,M_\odot$ (Seward & Charles, 1995, p. 100). Both the emitted energy of $10^{52}\,\mathrm{erg\,s^{-1}}$ (Seward & Charles, 1995, p. 101) and the light curve in the optical (see, e.g., Cadonau et al., 1985, their Fig. 1) are characteristic for this type of supernova explosion. Type Ia supernovae are therefore *standard candles*, which is the general term for astrophysical processes with known luminosity, that can be used to infer the distance based on the observed flux (see, e.g., Branch & Tammann, 1992). This is especially useful in cases where the distance cannot be inferred from parallax measurements. Such events can also be used to study the cosmos itself: Perlmutter et al. (1999) obtained values for the cosmological mass density Ω_M and the cosmological constant energy density Ω_Λ based on observations of 42 type Ia supernovae.

Whilst comparably light stars such as white dwarfs explode in type Ia supernovae, more massive stars with masses $\gtrsim 10\,M_\odot$ explode in type II supernovae (Seward & Charles, 1995, p. 101). Although far more massive, such stars have much shorter lifespans as the nuclear fusion within their cores is more efficient due to the higher gravitational pressure from the outer layers. For main-sequence stars, Demtröder (2014, p. 335) estimates that the lifetime of the star $\tau_{\mathrm{MS}} \propto M^{-2}$, which implies that the lifetime of a $10 M_\odot$ star is 100 times shorter than that of our sun.

In main sequence stars, the gravitational and gas pressures are in equilibrium with each other (Woosley et al., 2002). The change in pressure with radius r can be expressed as

$$\frac{\mathrm{d}P}{\mathrm{d}r} = -\frac{G\,M(r)\,\rho(r)}{r^2}, \tag{2.4}$$

where G is the gravitational constant, $M(r)$ the mass enclosed within the radius r and $\rho(r)$ the density at radius r. Once the hydrogen within the star's core is depleted it contracts and allows for the fusion of helium into carbon and oxygen (Seward & Charles, 1995, p. 102). In the outer shells, hydrogen is fused into helium (Hanslmeier, 2002, p. 429). Within the core, increasingly heavier elements up to ^{56}Fe are being fused. Heavier elements than iron are not fused as it is the element with the highest nuclear binding energy per baryon (see, e.g., Pourshahian, 2017, Fig. 2b). The fusion of heavier elements is therefore no longer an exothermic, but endothermic process. As a consequence of the cessation of fusion, the core can no longer balance the inward gravitational pressure of the outer layers and collapses. The temperature, on the order of 10^{11} K, within the collapsing core allows iron nuclei to dissociate to α particles (Helium nuclei) and free protons and neutrons (Janka, 2012; Tauris & van den Heuvel, 2023), so that the core predominantly consists of the latter two baryons.

The process of electron capture

$$p + e^- \longrightarrow n + \nu_e \tag{2.5}$$

further converts protons to neutrons within the core. The collapse continues until the core reaches nuclear density and can collapse no further due to the strong nuclear force (Tauris & van den Heuvel, 2023) and can be seen as incompressible. Due to its extreme density and abundance of neutrons, the collapsed core is called a *proto-neutron star*.

The infalling material collides with the core during the *core bounce*, as a consequence of which an outward propagating shock wave is formed (see, e.g., Janka, 2012). Whether the energy of the emerging shock wave ($\sim 10^{51}\,\mathrm{erg\,s^{-1}}$, Tauris & van den Heuvel, 2023) is strong enough to both stop the inward collapse of the outer shells, as well as disperse them in a large explosion, is still debated in the scientific community (see, e.g., Janka et al., 2007; Burrows & Vartanyan, 2021). A large fraction of the total energy released by the gravitational collapse of $\sim 10^{53}\,\mathrm{erg\,s^{-1}}$ is converted to neutrinos (Tauris & van den Heuvel, 2023).

Shortly after the core bounce, neutrinos transfer their high degeneracy energy to the stellar medium via thermal heating; this process is therefore called *neutrino heating* and is thought to be responsible for the re-acceleration of the stalled outward moving shock.

The inferred bolometric luminosities of some supernova explosions of $\sim 10^{52}\,\mathrm{erg\,s^{-1}}$, however, suggest that neutrino heating is not the sole driving mechanism for the SN explosion (Janka, 2012). Gamow & Schoenberg (1941) argue that the proto-neutron star eventually becomes transparent for neutrinos, which can then cool the neutron star with high efficiency via the URCA process[2]. The neutrino-induced cooling of the proto-neutron star is therefore called *neutrino cooling*. Lattimer et al. (1991) have shown that the most direct URCA process is only possible if the proton concentration within the proto-neutron star exceeds a critical value of 11–15%.

Especially relevant for the present work is the remnant of the supernova explosion, the proto-neutron star. For progenitor masses of $\gtrsim 25\,M_\odot$, the proto-neutron star eventually collapses into a black hole, otherwise it evolves into a neutron star (Janka et al., 2007). The mass of the remaining neutron star is typically close to the Chandrasekhar limit of $1.44\,M_\odot$; Tauris & van den Heuvel (2023) note however that much higher masses up to $\sim 2\,M_\odot$ have been found, for example $1.77 \pm 0.08 M_\odot$ for Vela X−1 (Rawls et al., 2011), that are thought to be the result of non-degenerate cores during the shell burning process. The progenitor core's angular momentum is thought to be conserved, its collapse therefore implies that the spin frequency drastically increases; Ott et al. (2006) perform 2D radiation-hydrodynamic simulations and obtain spin periods on the order of 1 ms for the proto-neutron star; which is however significantly faster than rotation periods observed for young pulsars of few 10-100 ms (see, e.g., Kaspi & Helfand, 2002). Similarly, the magnetic flux of the progenitor is also conserved, which causes neutron stars to have extremely high magnetic field strengths near their surface; values of 10^{11}–10^{13} G are common (see, e.g., Ferrario & Wickramasinghe, 2005).

2.4 High-mass X-ray binary systems

Following the above brief description of neutron star formation, I now turn to the description and classification of high-mass X-ray binary systems in Sect. 2.4.1. Thereafter I will discuss their formation in Sect. 2.4.2.

2.4.1 Properties and classifications of HMXBs

Here I present possible classifications of high-mass X-ray binaries, their characteristics, and formation. In general, the HMXB population can be divided based on the nature of the compact object, which is either a neutron star or a black hole. The two groups are often distinguished by the detection of pulsed X-ray emission that is expected to be produced by neutron stars only.

The population can further be sub-classified based on the nature of the companion. Chaty (2011) divide them into Be X-ray binaries, where the companion is a rapidly spinning main-sequence Be star and supergiant X-ray binaries, where the donor star is an early-type supergiant OB star with typical mass of 20–50 $M_\odot$. Be X-ray binary systems (BeXRBs) are often transient systems, which show periodic and irregular outbursts. Between outbursts their X-ray emission is often below the threshold of X-ray all-sky monitors. Supergiant X-ray binaries (SgXBs or SgXRBs) on the other hand are predominantly bright persistent sources, whose X-ray radiation is detected continuously. SgXBs can be subclassified based on the mass transfer mechanism:

[2]The URCA is named after the Urca casino in Rio de Janeiro, where according to Gamow & Schoenberg gambler's money disappears just as fast as the thermal energy of the proto-neutron star. For further information, see Gamow (1970).

evolutionary induced expansion of the donor star beyond its Roche lobe[3] allows mass transfer via Roche lobe overflow. The second subclass transfers mass via strong stellar winds (values of $\dot{M} \sim 10^{-6}\,M_\odot\,\mathrm{yr}^{-1}$ are common).

Walter et al. (2015) take the nature of compact object and companion as well as the temporal X-ray emission characteristic into account and classify the population of Galactic HMXBs as follows:

i. HMXBs harboring black holes. Three Galactic systems of this class (Cygnus X−1, Cygnus X−3 and SS 433 are) are known.

All following subclasses have neutron stars as the compact object.

ii. Persistent HMXBs including super-giant companions. This class contains well-known and intensively studied sources such as Vela X−1 and GX 301−2.

iii. Super-giant fast X-ray transients (SFXTs). Transient is here understood as showing X-ray fluxes >10 mCrab for short periods.

iv. Roche Lobe Overflow giant systems. Within the Galaxy only Centaurus X−3 is a confirmed member of this group.

v. HMXBs including Be star companions (BeXRBs). This class contains primarily transient systems, among them 4U 0115+63 (see, e.g., Heindl, 2000; Ferrigno et al., 2009), GX 304−1 (recently modeled at low luminosities by Sokolova-Lapa et al., 2021) and GRO J1008−57 (see, e.g., Kühnel et al., 2013; Tsygankov et al., 2023). With ~60 members it is the largest subclass of HMXBs.

vi. Gamma-ray emitting HMXBs. The optical companions of the three known systems of this class (LSI 61+303, PSR B1259−63, LS 5039) are Be stars.

vii. Giant and main-sequence systems. This class contains the HMXBs where the companion is not a supergiant or Be star, of which four are known within the Galaxy.

viii. "Other" systems: this group of 12 systems contains all those whose classification in the above categories has not been possible from previous observations.

It is evident that the vast majority of known Galactic HMXB systems contains neutron stars[4]. As this work focuses on pulsating HMXBs in quiescence, primarily the BeXRB subgroup is of high interest, as most SgXBs have too high mass-accretion rates, resulting in luminosities exceeding the quiescent state of interest at $\sim 10^{34}\,\mathrm{erg\,s^{-1}}$ by far. For HMXBs harboring black holes I refer to Albert et al. (2007), and to Liang & Nolan (1984) and Wilms et al. (2006) for discussions of Cygnus X−1.

HMXBs harboring magnetised neutron stars are further classified by two criteria: based on the X-ray emissivity of the systems, they are classified as either *persistent* or *transient* sources. Neumann et al. (2023) and Avakyan et al. (2023) published and maintain catalogues of both high-mass and low-mass X-ray binaries, respectively[5], which also distinguishes between persistent and transient sources. Examples of persistent high-mass X-ray binaries harboring NSs include

[3]The Roche lobe is the theoretical sphere-like volume around the star in which matter is gravitationally bound to it. It is discussed in more detail in Sect. 2.5.

[4]This statement does however *not* imply that the actual population of HMXBs harboring black holes is smaller. For discussions of the expected Galactic HMXB population, see, e.g., Iben et al. (1995).

[5]See `http://astro.uni-tuebingen.de/~xrbcat/HMXBcat.html` and `http://astro.uni-tuebingen.de/~xrbcat/LMXBcat.html`

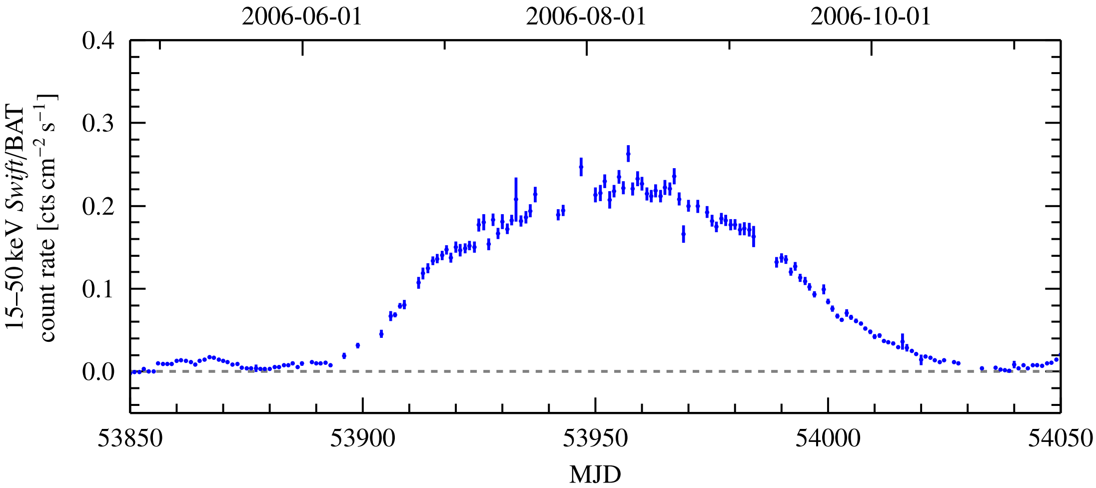

Figure 2.2: *Swift*/BAT light curve of EXO 2030+375 during its 2006 type II outburst. Data obtained from the *Swift*/BAT Hard X-ray Transient Monitor (See `https://swift.gsfc.nasa.gov/results/transients`).

the aforementioned system GX 301−2 (see, e.g., Doroshenko et al., 2010a; Zalot et al., 2024), Vela X−1 (see, e.g., Kreykenbohm et al., 2002; Kretschmar et al., 2021) and Cen X−3 (see, e.g., Naik et al., 2011; Tsygankov et al., 2022). For a list of persistent Galactic HMXBs as seen by *INTEGRAL*, see Lutovinov et al. (2013).

As the name suggests, transient sources show an altogether different behaviour; they appear very bright during outbursts and very dim, if detectable at all, between outbursts.

As the duration of outbursts is usually on the order of days to weeks close monitoring by All-Sky monitors such as the *Swift*/BAT (see Sect. 3.1.3) and the All-Sky monitor (ASM) are required to detect them in time to coordinate X-ray observations with broad-band instruments such as *NuSTAR* (see Sect. 3.1.2). Stella et al. (1986) proposed a classification of such outbursts where type I outbursts occur at regular intervals related to the orbital period of the NS with $\mathcal{L}_X \sim 10^{36}$–$10^{37}\,\mathrm{erg\,s^{-1}}$, whereas giant type II outbursts are less frequent and regular, but show X-ray luminosities $\gtrsim 10^{37}\,\mathrm{erg\,s^{-1}}$.

Many transient sources such as 4U 0115+63 and EXO 2030+375 show both regular type I and irregular type II outbursts. A more recent outburst of EXO 2030+375 occurred in 2022 and has been observed by multiple X-ray missions and studied in detail, see, e.g., Thalhammer et al. (2024) and Ballhausen et al. (2024). As Fig. 2.2 of EXO 2030+375's earlier outburst in 2006 shows, type II outbursts can last for multiple weeks, which allow to study the source during the rising and falling flanks of the outburst as well as its peak. For this study, the deep quiescent state between outbursts is especially interesting, as it allows to study sources at their lowest luminosities. In case a source is not detectable in this state, observations during the falling flank of outbursts are also of interest, as the X-ray luminosities are typically on the order of $\sim 10^{34}\,\mathrm{erg\,s^{-1}}$.

2.4.2 Formation of HMXBs

Following the brief description of core-collapse supernovae in Sect. 2.3 and the general properties of high-mass X-ray binary systems above, I now turn to the formation of high-mass X-ray binary systems containing one massive-type star and one neutron star. To accompany the description of HMXB formation in this section, I show the schematic evolution from a stellar binary system to a HMXB system in Fig. 2.3. Progenitors of HXMBs are naturally double stars.

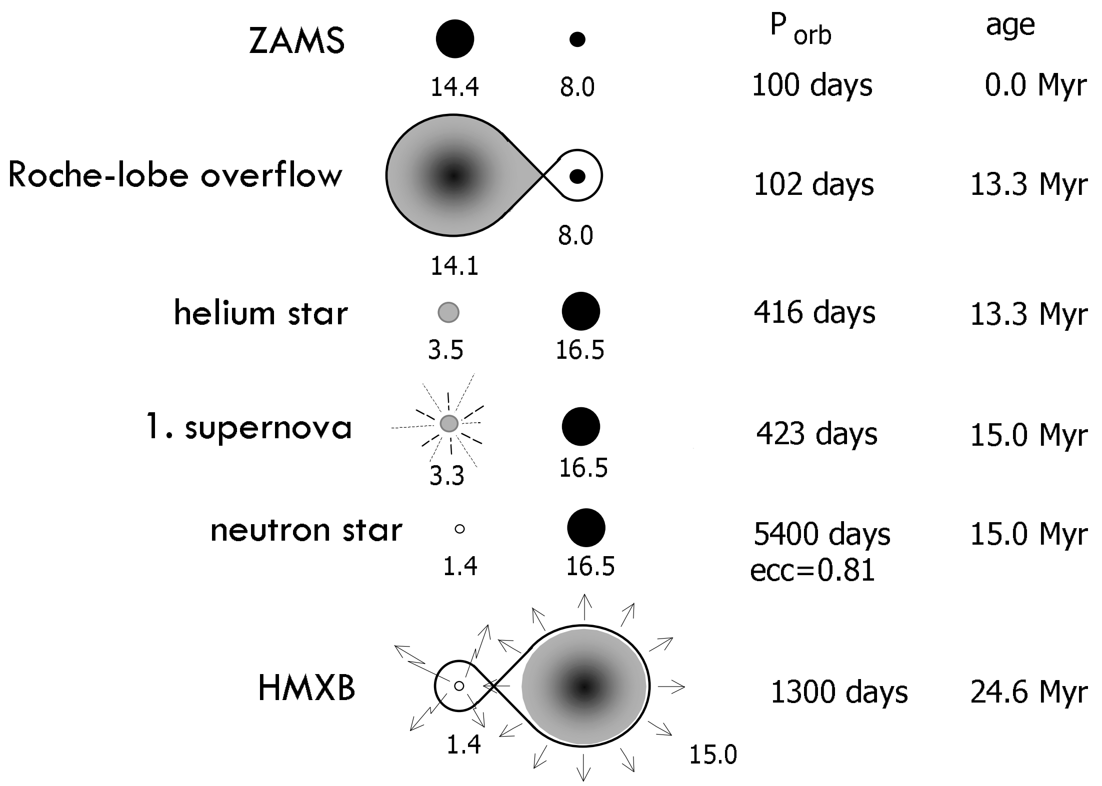

Figure 2.3: Formation of HMXBs. The numbers below the objects give their mass in units of $M_{\odot}$. Figure adapted from Tauris & van den Heuvel (2006).

Their primary component is a massive-type star with mass on the order of ~8–15 $M_{\odot}$ whose ~2 $M_{\odot}$ core consists of helium (Tauris & van den Heuvel, 2023). The secondary component is a lighter star with mass on the order of ~6 $M_{\odot}$ (Tauris & van den Heuvel, 2023).

The primary component expands during its evolution and fills up its Roche lobe, which is the region in which the gravitational force of the primary component exceeds that of the secondary component. Matter that surpasses this boundary is therefore transferred onto the secondary component. This process is known as accretion via Roche lobe overflow. The mass transfer itself is a highly interesting process and has many effects on the system: firstly, as the mass transfer implies transfer of angular momentum onto the secondary component, it spins up significantly; surface velocities of $v \sin i \sim 100\,\mathrm{km\,s^{-1}}$ are common (Pols et al., 1991)[6]. Secondly, due to the angular momentum of the accreted material in the vicinity of the secondary component, an accretion disk may form. Thirdly, the binary orbit widens, increasing the orbital period from a few days to tens of days (Tauris & van den Heuvel, 2023). Approximately $\sim 10^3$ years after the cessation of the mass transfer, the primary component explodes in a core-collapse supernova (Tauris & van den Heuvel, 2023). Asymmetries in the explosion can cause the newly formed neutron star to shift from its initial position in the binary, known as a natal kick (see, e.g., Repetto et al., 2017), which could break up the binary system. Naturally, I focus here on the cases where the binary system remains intact.

After the core-collapse supernova of the primary component, the masses of the two constituents of the binary system have changed significantly: the neutron star has a canonical

[6]This type of binary interaction is thought to be the predominant theory for the formation of Be stars, which show such rapid rotations and are often found in binary systems with compact objects, but far rarer in binary systems with main sequence stars as Bodensteiner et al. (2020) find.

mass of ∼1.4 $M_\odot$, the secondary component (also called donor star, companion star or optical counterpart) has accreted large portions of the primary constituent's mass, resulting in $M_{\mathrm{companion}} \sim 17\,M_\odot$ for the initial masses stated above (Tauris & van den Heuvel, 2023). To summarize, the newly formed HMXB system consists of a neutron star and a massive star, which is either a supergiant or rapidly-spinning Be star.

Due to the fact that $M_{\mathrm{companion}} \gg M_{\mathrm{NS}}$, the barycenter is now nearer to the companion star, if not even contained within it. This effectively results in a system where the neutron star orbits its companion on a potentially highly eccentric (see Fig. 2.1) orbit.

2.5 Accretion in HMXB systems

The notable emission of X-rays and in some cases even gamma rays of HMXBs, which can reach luminosities on the order of $\mathcal{L}_\mathrm{X} \sim 10^{37}\,\mathrm{erg\,s^{-1}}$ in the X-ray band, warrants investigation to the emission mechanism and its energy source. A major part of the observed X-ray emission is a result of the mass transfer from the companion star onto the compact object, a process called *accretion*. Due to the intense gravitational force of the latter, gravitational energy is released during the mass transfer, which is usually emitted as radiative energy in the X-ray band.

In order to estimate the magnitude of the released energy due to accretion, I consider the simple case of a single electron with mass $m_\mathrm{e} \approx 9.1 \times 10^{-31}$ kg approaching a canonical neutron star of mass $M_{\mathrm{NS}} = 1.4\,M_\odot$ from infinity up to its surface at $R_{\mathrm{NS}} = 10\,\mathrm{km}$. For simplicity, the neutron star is modeled as a point mass. The released gravitational energy can be expressed as

$$E_{\mathrm{released}} = \int_\infty^{R_{\mathrm{NS}}} -\frac{G\,M_{\mathrm{NS}}\,m_\mathrm{e}}{r^2}\mathrm{d}r = \left[\frac{G\,M_{\mathrm{NS}}\,m_\mathrm{e}}{r}\right]_\infty^{R_{\mathrm{NS}}} = \frac{G\,M_{\mathrm{NS}}\,m_\mathrm{e}}{R_{\mathrm{NS}}} \approx 106\,\mathrm{keV}. \tag{2.6}$$

Contrary to this simple example however, protons contribute significantly more to the released energy as their mass is larger by a factor of ∼1836. Furthermore, accreted protons can transmit their kinetic energy more efficiently via interactions in a plasma close to the NS surface, which becomes especially important at low mass-accretion rates. At high mass-accretion rates, Compton interactions play a more significant role in the braking of the infalling plasma.

In order to express the accretion luminosity as a function of mass accretion rate $\dot{M}$, one can generalise Eq. 2.6 and obtain

$$\mathcal{L}_{\mathrm{acc}} = \frac{G\,M_{\mathrm{NS}}\,\dot{M}}{R_{\mathrm{NS}}} \approx 1.9 \times 10^{36} \cdot \left(\frac{M_{\mathrm{NS}}}{1.4\,M_\odot}\right)\left(\frac{\dot{M}}{10^{16}\,\mathrm{g\,s^{-1}}}\right)\left(\frac{R_{\mathrm{NS}}}{10\,\mathrm{km}}\right)^{-1} \mathrm{erg\,s^{-1}}. \tag{2.7}$$

At high-mass accretion rates and subsequently high X-ray luminosities, the material is predominantly decelerated in a radiative shock due to the outward radiation (see, e.g., Becker et al., 2012). The luminosity at which the outward radiation pressure equals the inward gravitational pressure is known as the Eddington luminosity. For spherically symmetric accretion consisting of purely ionized hydrogen onto a neutron star, Frank et al. (2002) estimate the Eddington luminosity as

$$\mathcal{L}_{\mathrm{Edd}} \approx 1.3 \times 10^{38} \cdot \left(\frac{M_{\mathrm{NS}}}{M_\odot}\right) \mathrm{erg\,s^{-1}}. \tag{2.8}$$

Taking a step back and focusing on the binary system as a whole, accretion requires a mechanism to remove matter sufficiently far from the donor star to overcome its gravitational force. Frank et al. (2002) present two distinct mechanisms that allow for accretion in HMXBs:

i. Roche lobe overflow: during the later stages of its life the donor star may expand, in which case its outer layers transcend the Roche lobe and thereby transfer matter onto the compact companion. The Roche lobes of the two constituents of a HMXB system are schematically

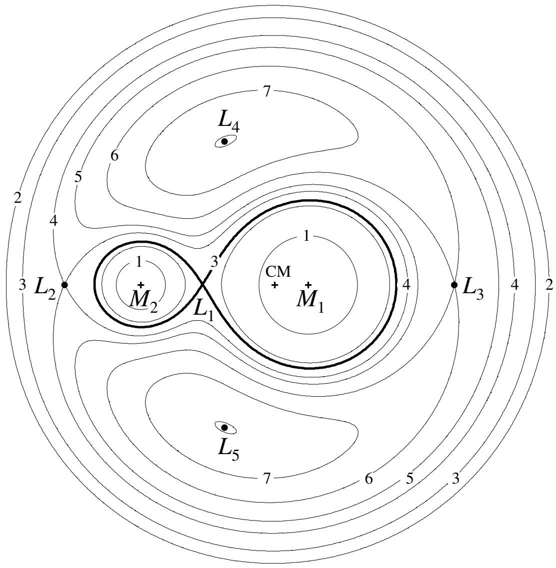

Figure 2.4: Equipotential lines in a 2D projection of a binary system consisting of two point masses M_1 and M_2. CM denotes the center of mass and L_i the i-th Lagrange point. The bold lines represent the Roche lobes of the two objects, which intersect in L_1. Figure reproduced from Frank et al. (2002).

shown in Fig. 2.4. Also, a similar effect arises in case that the total separation a in the binary system decreases due to binary evolution: due to the tightening of the binary system, the Roche lobe of the donor star shrinks, so that the outer layers may no longer be contained within it.

ii. Stellar winds: during the course of its evolution the donor star can expel its outer layers as a strong stellar wind and thereby transfer matter onto its compact star companion. Vela X−1 is a prominent example of a wind-accreting HMXB (see, e.g., Kretschmar et al., 2021).

For BeXRBs there exists another means of transferring matter: Be stars are known to form decretion disks (see, e.g., Rivinius et al., 2013), which are a result of their fast rotation. Matter can in this case also be transferred from the decretion disk onto the compact object.

The angular momentum of the accreted matter cannot be neglected, even less so in the case of binary systems including Be stars. The velocity component of the accreted matter perpendicular to the connecting line between the two stars can be expressed as

$$v_\perp \sim 100\,\mathrm{km\,s^{-1}}(1+q)^{1/3}\left(\frac{P_\mathrm{orb}}{1\,\mathrm{day}}\right)^{-1/3}, \tag{2.9}$$

where q is the mass ratio $M_\mathrm{NS}/M_\mathrm{donor}$ (Frank et al., 2002). It is important to note that the velocity component parallel to the connecting line between the two bodies is far smaller than the eventual free-fall velocity of ~$0.5c$ near the NS as we are considering the matter close to L_1, i.e. far removed from the neutron star. Frank et al. (2002) emphasize that $v_\| \sim 10\,\mathrm{km\,s^{-1}} \ll v_\perp$, which further demonstrates the need to consider the exact trajectory of the accreted matter. Frank et al. (2002) calculate such a trajectory and find that the accreted gas follows a slowly precessing elliptical orbit; particle scattering will eventually lead to a circular orbit around the compact object. Particles with higher angular momentum, and therefore energy, orbit the compact object on a wider trajectory and vice versa, leading to the formation of an accretion disk. Due to this rotation differential, viscous forces slowly convert gravitational energy into heat, allowing a test particle to spiral inwards and eventually be accreted by the neutron star. As accretion disks will play only a minor role in the present work I refer to Pringle (1981) for a historic review of accretion disks and Frank et al. (2002) for an extensive discussion of various accretion mechanisms.

2.6 Spectral formation in HMXBs

In the following I will briefly introduce the spectral formation process at high mass accretion rates in Sect. 2.6.1, before describing the process for low mass accretion rates in Sect. 2.6.2, which is the main focus of this work.

2.6.1 Spectral formation at high mass accretion rates

This section contains a brief description of the spectral formation process at high mass accretion rates, which are primarily observed in persistent HMXBs harboring pulsars, and transient HMXBs during bright outbursts. At high luminosities, the infalling matter is decelerated via interactions with particles and photons alike. Above the NS surface at a still debated height, a radiative shock causes the infalling matter to emit Bremsstrahlung via inelastic scattering with upward propagating photons. Becker et al. (2012) provide an expression for the height of the radiative shock H,

$$H = 1.14\,\mathrm{km} \times \left(\frac{M_\mathrm{NS}}{1.4 M_\odot}\right)^{-1} \left(\frac{R_\mathrm{NS}}{10\,\mathrm{km}}\right) \left(\frac{L_X}{10^{37}\,\mathrm{erg\,s^{-1}}}\right), \tag{2.10}$$

where L_X is the emitted X-ray luminosity. At such high luminosities, the matter is then further decelerated by a radiation-dominated shock; at lower luminosities of 10^{36}–$10^{37}\,\mathrm{erg\,s^{-1}}$, the radiation pressure is not sufficient to brake the matter. In this case, therefore, collisionless shocks (see, e.g., Shapiro & Salpeter, 1975) and Coulomb interactions near the NS surface (Staubert et al., 2007) brake the matter further. In either case, the emergent radiation is primarily in the X-ray band. The broadband spectrum is often well represented by a powerlaw with exponential cutoff (see, e.g., Mihara et al., 1995; Ballhausen, 2021), which are further discussed in Sect. 2.7.

2.6.2 Spectral formation at low mass accretion rates

Following the above brief overview of the accretion process in HMXBs and their behaviour at high and intermediate luminosities, here I discuss the accretion process and subsequent spectral formation at luminosities below $\sim 10^{34}\,\mathrm{erg\,s^{-1}}$, corresponding to mass-accretion rates $\dot{M} \lesssim 10^{15}\,\mathrm{g\,s^{-1}}$. At such low luminosities, the outgoing radiation is too weak to decelerate the infalling plasma. The braking of the plasma therefore takes place only very close to the NS surface within its atmosphere, where infalling particles undergo Coulomb interactions with atmospheric particles. These interactions lead to a heating of the atmosphere, which is strongly height-dependent as shown by Zel'dovich & Shakura (1969, Fig. 1): the Coulomb interactions mainly heat the optically thin upper parts of the atmosphere to $\sim 10^8$ K, while near the neutron star's surface temperatures of $\sim 10^7$ K prevail. As a result, the NS atmosphere is very inhomogeneous with a dense and cold interior and a strong outward temperature gradient. Furthermore, the strong magnetic field in the vicinity of the NS causes vacuum birefringence (see, e.g., Sokolova-Lapa et al., 2023a). In the following, the ordinary mode corresponds to that in which the vector of the electric field $\mathbf{E}$ is in the plane of the wave vector $\mathbf{k}$ and the magnetic field vector $\mathbf{B}$; the extraordinary mode corresponds to $\mathbf{E} \perp (\mathbf{k}, \mathbf{B})$.

Sokolova-Lapa et al. (2021) find that deep down within the NS atmosphere, where $k_\mathrm{B}T \sim 2\,\mathrm{keV}$ and $\tau_\mathrm{T} \approx 10^2$, both polarization modes are mixed, but only the extraordinary photons

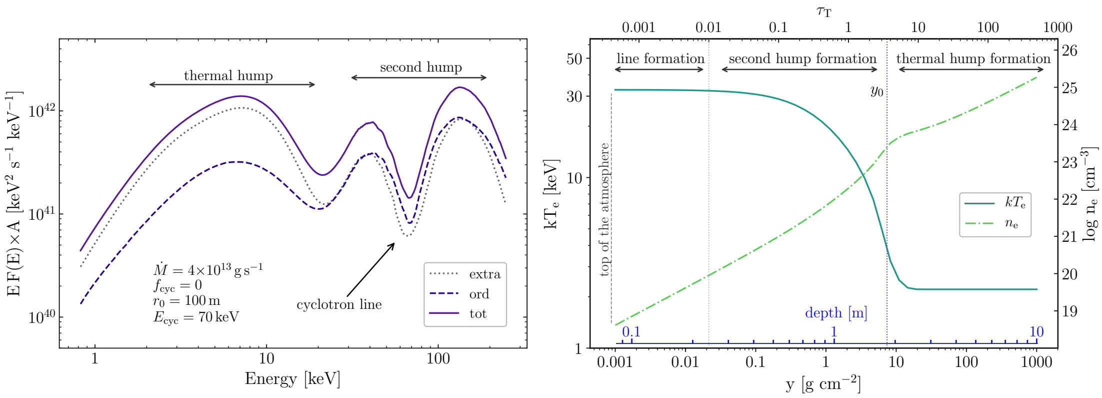

Figure 2.5: Spectral formation at low luminosities. Left: energy flux spectrum in two orthogonal polarization modes for a X-ray binary pulsar at low luminosity. The spectrum contains a thermal and nonthermal hump; the latter is imprinted with a broad and deep CRSF. Right: Electron temperature and number density throughout the NS atmosphere. The NS surface is on the far right, the top of the atmosphere on the far left. Figure reproduced from Sokolova-Lapa et al. (2021).

can escape the atmosphere as their mean free paths are much longer in comparison, leading to the formation of the so-called *thermal hump* consisting of soft extraordinary photons. As indicated by its name, the thermal hump can be described by a blackbody-like component with temperature[7] in the soft X-ray band (e.g., ∼1.7 keV for GX 304−1, see Tsygankov et al., 2019c).

Slightly higher in the optically thick part of the atmosphere ($\tau_T \approx 10$), the temperature increases due to the influence of the infalling plasma: inelastic Compton scattering between thermal photons and ambient particles increases the photons' energies to tens of keV. This process is known as Compton up-scattering.

At these energies cyclotron interactions become relevant: due to the intense magnetic field strength electron momenta perpendicular to the B-field axis become quantized. Electrons can transition to higher or lower Landau levels by resonant scattering with photons. Landau levels are approximately equidistant (see Zalot et al., 2024, Sect. 5.2 for a detailed discussion), where the energy difference between two adjacent levels is called the fundamental line energy and is related to the magnetic field strength B via

$$E_{\rm cyc} \approx \frac{1}{1+z}\frac{B}{10^{12}\,\rm G} \times 11.6\,\rm keV, \tag{2.11}$$

where z is the gravitational redshift (see, e.g., Staubert et al., 2019). In general, many HMXBs exhibit cyclotron lines (also known as cyclotron resonant scattering features or CRSFs) at energies from 10–100 keV, which are absorption line-like features in some cases accompanied by emission wings.

In the context of the presently discussed NS atmosphere at $\tau_T \approx 10$, Sokolova-Lapa et al. (2021) state that cyclotron interactions are not negligible and corresponding absorption features and wings are present in the photon density spectra.

Higher in the atmosphere where $\tau_T \approx 1$, the impact of Compton up-scattering increases. Sokolova-Lapa et al. (2021) find that in this layer the CRSF feature is much less apparent and in fact almost indiscernible in some cases, which they attribute to the strong temperature gradient in this region caused by the accreted matter and diffusion of photons away from the cyclotron

[7] In this work, I will often speak of temperatures in terms of energy, i.e. $E = k_B T$.

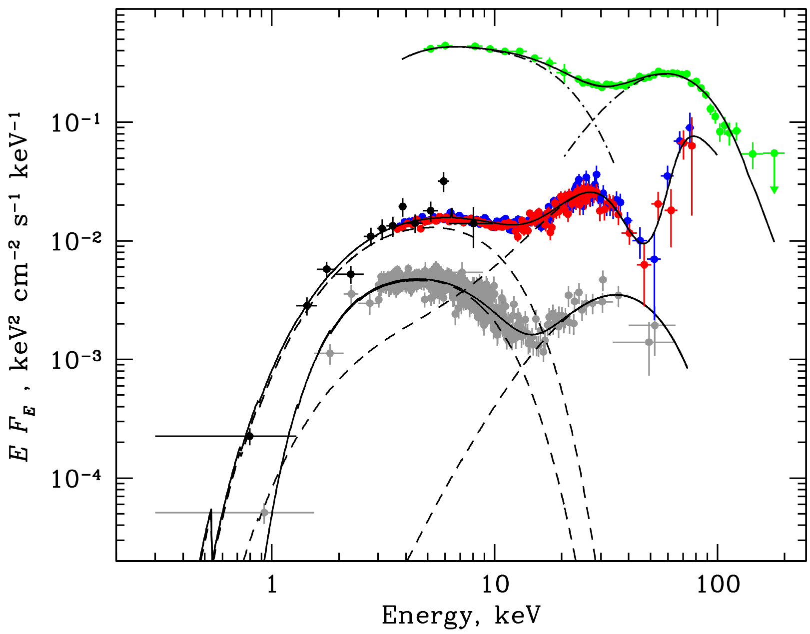

Figure 2.6: Double hump spectra of selected sources as observed at low mass accretion rates. Shown are the spectra of X-Persei (green), A0535+26 (red and blue for the two *NuSTAR* focal plane modules A and B, respectively) and GX 304−1 (grey). Also shown with dotted lines are the individual model components for the two humps, here modeled using the `comptt` model (see Titarchuk, 1994). The spectrum of A0535+26 shows a deep cyclotron line at ~45 keV. Figure reproduced from Tsygankov et al. (2019a).

line energy so that also no emission wings are present either. Instead, the diffused photons are merged in a high-energy hump.

At the highest part of the atmosphere where $\tau_T \approx 10^{-2}$ a CRSF feature forms once again, which is broadened significantly due to the high electron temperature; Sokolova-Lapa et al. (2021) quote a CRSF width of ≈27 keV for $E_{cyc} = 70$ keV and an electron temperature of $kT_e = 33$ keV, which is in agreement with Meszaros & Nagel's formula for a Doppler-broadened CRSF. The Compton up-scattering of soft photons leads to the formation of an unpolarized high-energy hump, in this work denoted as *nonthermal hump* in contrast to the polarized blackbody-like component. The resulting X-ray emission is therefore the sum of the emission from all layers of the strongly inhomogeneous NS atmosphere. The emergent energy flux spectrum as well as the temperature and electron density within the NS atmosphere is shown are Fig. 2.5.

In summary, the X-ray spectrum of X-ray binary pulsars at low luminosities consists of a thermal component, which dominates the emission at energies ≲20 keV and a nonthermal hump, which is the red wing of a high-energy cyclotron line and extends beyond 100 keV. A deep and broad cyclotron line is imprinted on the nonthermal hump. Due to their shape, such spectra are known as *double-hump spectra*. Examples of such spectra are shown in Fig. 2.6 for three characteristic sources. It is important to remember that such spectra are only observed at low mass accretion rates and that the observed double-hump vanishes at higher mass accretion rates, for which continua without humps are typically observed.

2.7 Phenomenological and physical spectral models

In the following, I discuss a variety of spectral models, that are applied to the broadband X-ray spectra of HMXBs harboring accreting neutron stars. Such spectra are often described by empirical spectral models, which I introduce in Sect. 2.7.1. They are often simple mathematical expressions, their parameters therefore have no physical motivation, but can nevertheless serve many different purposes, for example, tracking how a spectrum changes at different luminosities. Subsequently, in Sect. 2.7.2 I introduce spectral models utilized to describe specific spectral components, such as emission or absorption lines. On the other hand, as physically motivated models become more widely available, they are used with increasing frequency in order to directly quantify the underlying physical principles. I provide a brief overview over a selection of physical spectral models in Sect. 2.7.3.

2.7.1 Phenomenological spectral models for broadband X-ray spectra

The simplest model used to describe the broadband X-ray spectrum of accreting pulsars consists of a powerlaw with an exponential cutoff known as `cutoffpl`, which is defined as

$$I(E) = K \cdot E^{-\Gamma} \times \exp\left(-\frac{E}{E_{\mathrm{fold}}}\right) \tag{2.12}$$

where K is the normalisation constant, Γ the photon index of the powerlaw and E_{fold} the folding energy related to the slope of the exponential cutoff. In order to further change the location (i.e. energy) where the exponential cutoff impacts the model, one can make use of the slightly more complex model `highecut`,

$$I(E) = K \cdot E^{-\Gamma} \times \begin{cases} 1 & E \leq E_{\mathrm{cutoff}} \\ \exp\left(-\frac{E-E_{\mathrm{cutoff}}}{E_{\mathrm{fold}}}\right) & E > E_{\mathrm{cutoff}} \end{cases}, \tag{2.13}$$

which introduces an undesirable discontinuity at the cutoff energy E_{cutoff}, which Staubert et al. (2019) note can be removed by introducing an artificial absorption component at E_{cutoff} (see, e.g., Coburn et al., 2002) or replacing the discontinuity and its surroundings by a third-order polynomial (see, e.g., Klochkov et al., 2008). A similarly versatile model without a discontinuity is a powerlaw in combination with a Fermi-Dirac cutoff, the latter being known as `FDcut` (Tanaka, 1986). It can be expressed as

$$I(E) = K \cdot E^{-\Gamma} \times \left[1 + \exp\left(\frac{E - E_{\mathrm{cutoff}}}{E_{\mathrm{fold}}}\right)\right]^{-1}. \tag{2.14}$$

Although the three introduced spectral models all describe a powerlaw with high-energy cutoff, there are subtle differences between them, which can be easily seen when showing them together. I therefore show them in various parameter configurations in Fig. 2.7.

It is evident that these three functions already allow for a mathematical description of a considerable range of possible spectral shapes. Of the various other phenomenological continuum models I only mention one more, which is used so often in the community (see, e.g., Fürst et al., 2018; Iwakiri et al., 2019) that it is imperative to be included here. The negative positive exponential model (`NPEX`, Mihara, 1995) consists of two powerlaw components with positive and negative photon indices, respectively, which are both subject to an exponential cutoff. It is often expressed as

$$I(E) = \left(K_1 E^{-\Gamma_1} + K_2 E^{+\Gamma_2}\right) \times \exp\left(-\frac{E}{E_{\mathrm{fold}}}\right), \tag{2.15}$$

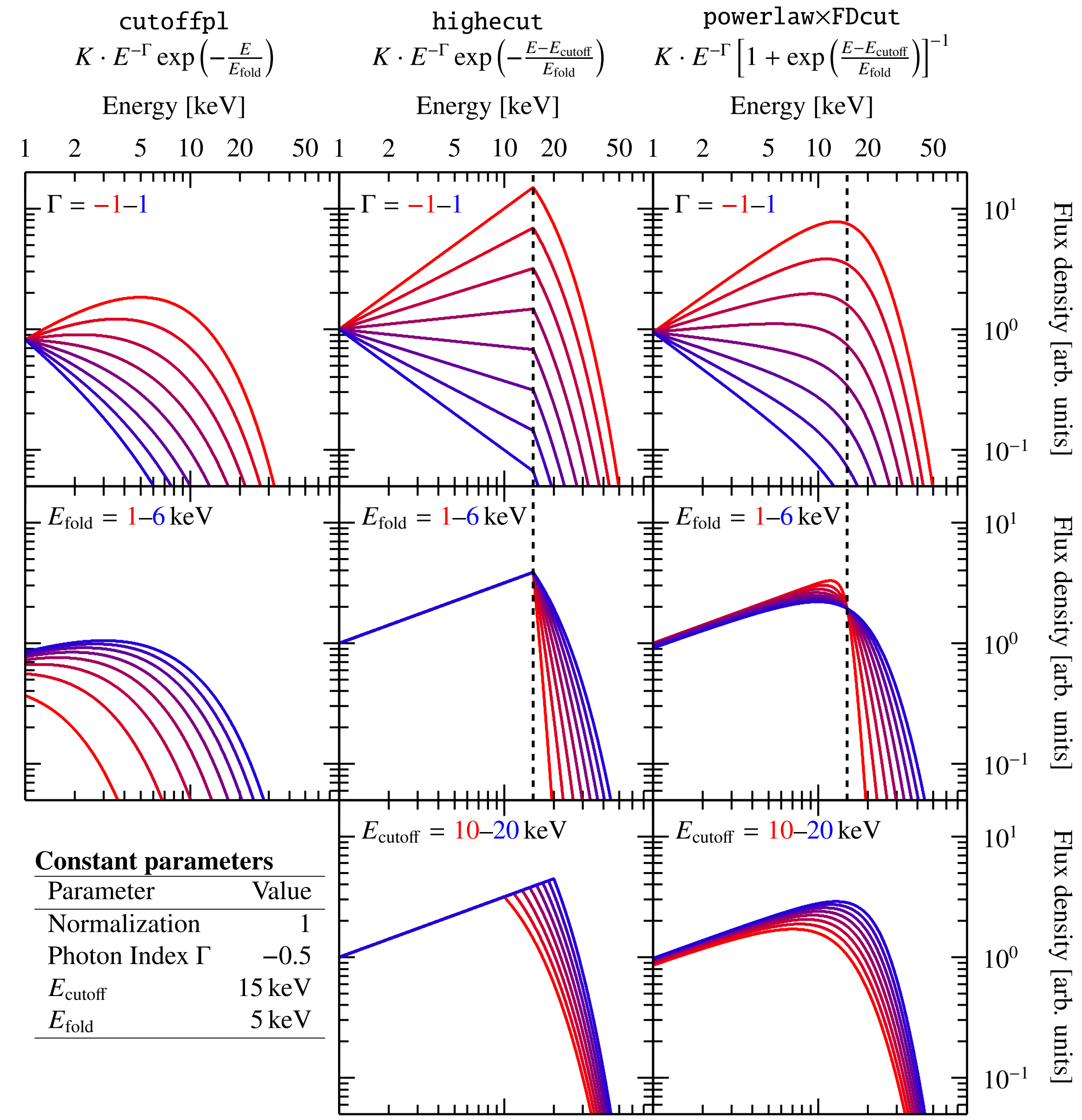

Figure 2.7: The three phenomenological spectral models `cutoffpl`, `highecut` and `powerlaw×FDcut`. Row-wise the function parameters are varied linearly within the given ranges. The otherwise constant parameters are given in the lower left corner.

where $K_{1/2}$ are the normalisations of the two components and $\Gamma_{1/2}$ their photon indices. The alternative definition

$$I(E) = K_{\mathrm{tot}} \times \left(E^{-\Gamma_1} + K_2 E^{+\Gamma_2}\right) \times \exp\left(-\frac{E}{E_{\mathrm{fold}}}\right) \tag{2.16}$$

is also often used and simplifies the comparison between the two components, as K_2 is in this case the relative norm of the positive powerlaw component. K_{tot} here is the total normalisation of the model. Staubert et al. (2019) note that commonly $\Gamma_2 = 2$ in order to account for the thermal distribution's Wien component.

Having now introduced four phenomenological models which all aim to describe broadband X-ray spectra, the question of which one to choose naturally arises. There is no undisputed answer; it is often however reasonable to start with the simplest possible model and introduce further degrees of freedom only when required. When phenomenological models are required in this work I therefore start with the `cutoffpl` model and only make use of the Fermi-Dirac cutoff when the `cutoffpl` model yields no satisfactory description of the data. The `highecut` model is not considered in this work due to its discontinuity at E_{cutoff}. The `NPEX` model also finds no application in this work.

2.7.2 Phenomenological models for spectral features

X-ray spectra of accreting pulsars are known to show various spectral features such as emission lines (see, e.g., Fürst et al., 2011), absorption features often attributed to cyclotron resonant scattering (see, e.g., Staubert et al., 2019) and the "10 keV feature" (see, e.g., Manikantan et al., 2023). Emission lines such as Fe $K\alpha$ at ~6.4 keV and Fe $K\beta$ at ~7.0 keV are very often modeled using Gaussian emission lines

$$I(E) = \frac{A}{\sqrt{2\pi}\sigma} \exp\left[-\frac{(E - E_{\text{center}})^2}{2\sigma^2}\right], \tag{2.17}$$

where A is the intensity of the emission line in units of photons $\text{s}^{-1}\,\text{cm}^{-2}$, E_{center} its centroid energy and σ its width. Absorption features are often described as multiplicative model components of the form

$$f(E) = \exp\left(-\tau(E)\right), \tag{2.18}$$

where the optical depth τ is often Gaussian,

$$\tau(E) = \tau_0 \exp\left[-\frac{(E - E_{\text{center}})^2}{2\sigma^2}\right], \tag{2.19}$$

where τ_0 is the optical depth at the line's centroid energy E_{center} and σ is the width of the absorption feature (see Staubert et al., 2019, Eq. 6). A disadvantage of this model is that more complex, asymmetric line shapes (see, e.g., Fürst et al., 2015, Fig. 3) cannot be adequately modeled and harmonics of the line have to be implemented separately.

2.7.3 Physical spectral models

In order to obtain a more physical description of spectral data and directly obtain physical information from it, theoretical works are focusing on the development of physical spectral models. Such models are based on the physical processes responsible for the emission of X-ray radiation close to the neutron star's surface.

In this environment extreme physical conditions prevail, which lead to many physical effects that have to be considered to obtain an accurate spectral model. Among these are light bending due to the strong gravitational force exerted by the neutron star's mass, emission of polarised radiation, and angle- and energy-dependence of emitted radiation. As this is a highly complex undertaking, a full mathematical treatment of radiative transfer is beyond the scope of this work. I refer the interested reader to Sokolova-Lapa (2023); I will also make references to chapter 4 therein when necessary.

Here, I focus instead on a brief description of the physical models utilized in this work. Sunyaev & Titarchuk (1980) developed an analytical model for the emission from a plasma cloud, as expected to be present near the neutron star surface. The model is based on the interaction of low-energy seed photons ($T_0 \sim 0.1$ keV) with the plasma of temperature T and optical depth τ. The seed photon energy T_0, plasma temperature $k_{\text{B}}T$ and optical depth are free parameters that can be varied in order to fit a spectrum; the model is however not physically valid for both low temperatures and low optical depths and high temperatures and high optical depths,

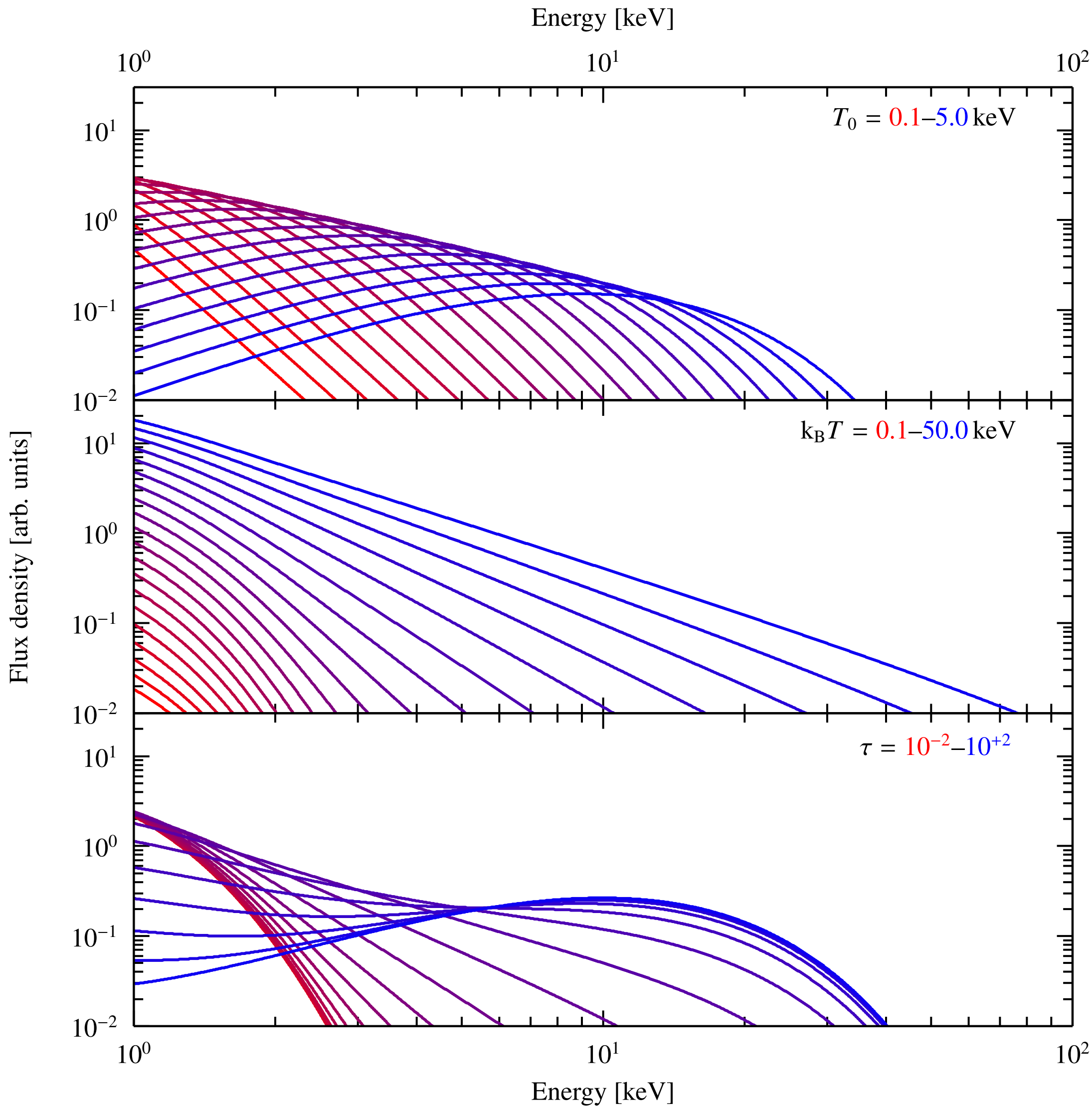

Figure 2.8: The `comptt` model in various parameter configurations. When not varied, the parameters are set to $T_0 = 0.2$ keV, $k_B T = 5$ keV and $\tau = 1$.

as for example hot plasmas are expected to be optically thin *because of* the high temperature. The relation between plasma temperature and optical depth can also be seen on the right-hand side of Fig. 2.5, from which it becomes clear that the optical depth decreases with increasing temperature. Titarchuk (1994) generalised this model by including relativistic effects as well, which is often found under the name `comptt` and has been used to describe the Comptonizing plasma; in particular it has been used to model *both* the thermal and nonthermal component of low-luminosity spectra of A0535+26 as shown in Fig. 2.6. I show the `comptt` model in various parameter configurations in Fig. 2.8.

It is evident that in some cases the `comptt` model yields similar spectral models as the phenomenological models described above and is therefore suitable to describe the thermal component of low-luminosity spectra.

For high optical depths, the `comptt` model shows a strong hump peaking at tens of keV as shown in the bottom panel of Fig. 2.8. From a mathematical point of view, it could be very well suited to describe the nonthermal hump low-luminosity spectra, however a problem becomes apparent: in this case the model would describe a high-temperature optically thick plasma, which is unphysical. For low-luminosity spectra of A0535+26 as shown here in Fig. 2.6, Tsygankov et al. (2019a) report a plasma temperature of 14.5 keV and optical depth exceeding 10, which already casts doubts on the suitability of the `comptt` model for the description of the nonthermal hump.

With this in mind, I introduce another model that could potentially provide a quasi-physical description of the nonthermal hump. For a non-magnetized plasma with Comptonization parameter

$$y = \left(\frac{4k_\mathrm{B}T}{m_\mathrm{e}c^2}\right)^2 \times \langle N_\mathrm{scat}(\tau)\rangle, \tag{2.20}$$

with $\langle N_\mathrm{scat}(\tau)\rangle$ denoting the average number of scattering events that a photon undergoes, much larger than unity, i.e. $y \gg 1$, Orlandini & Fiume (2001) suggest that saturated Compton scattering leads to the formation of a prominent hump at $3k_\mathrm{B}T$, which is often called Wien hump. Mathematically it can be expressed as

$$I(E) = K \cdot E^2 \times \exp\left(-\frac{E}{k_\mathrm{B}T}\right), \tag{2.21}$$

and is identical to a `cutoffpl` model for $\Gamma = -2$. Indirect implementation already exists in `XPSEC` and `ISIS`; I nevertheless added a direct implementation to the Remeis ISISscripts (see Sect. 3.3) under the name `wienhump`.

The `polcap` model (see Sokolova-Lapa et al., 2021; Sokolova-Lapa, 2023) is undoubtedly the most physically motived model mentioned; it includes a treatment of the radiative transfer equation and takes important physical effects such as light bending, polarisation, angle- and energy-dependency of the emitted radiation into account. It is applicable to X-ray spectra of slowly rotating ($P_\mathrm{pulse} \gtrsim 60\,\mathrm{s}$) high mass X-ray binaries with surface magnetic field strengths $B \gtrsim 5.3 \times 10^{12}\,\mathrm{G}$ (corresponding to $E_\mathrm{CRSF} \gtrsim 50\,\mathrm{keV}$) in the quiescent state at luminosities $\lesssim 10^{34}\,\mathrm{erg\,s^{-1}}$. The X-ray luminosity is however not a suitable indicator for the applicability of the `polcap` model; instead the presence of a two-component spectrum (i.e. thermal and nonthermal hump) should be considered. The energy-dependent interaction cross sections implemented in the model also account for cyclotron resonant scattering, allowing for spectra of neutron stars with varying magnetic field strengths to be modeled. The variable parameters of the model, in its current implementation, are the normalisation, which is related to the radius of the polar cap and the distance of the observer, the logarithm of the mass flux, and the fundamental cyclotron line energy in the neutron star rest frame. I show the variations in the spectral (table) model for the latter two parameters in Fig. 2.9. As expected, the mass flux has a similar effect as a change in normalisation, but it must be emphasized that the spectral shape also changes: the double-hump structure becomes more distinct for lower mass fluxes. The lower panel shows apparent that the CRSF energy is to be understood in the *neutron star* frame, whereas the simulated spectrum is naturally in the *observer's* frame: for the red model, the CRSF absorption feature is centered at ~40 keV, whereas the $E_\mathrm{CRSF} = 50\,\mathrm{keV}$ in the neutron star frame. This deviation of a factor of $50\,\mathrm{keV}/40\,\mathrm{keV} = 1.25$ is a result of the conversion from the neutron star frame to the observer's frame, corresponding to a shift of the energy grid by factor 1.24 for a canonical neutron star with mass $1.4M_\odot$ and radius 12 km. Apart from the theoretical modeling by Sokolova-Lapa et al. (2021), there are a number of other theoretical models that also treat the radiative transfer and are able to reproduce the observed double-hump spectral shape, for example the theoretical model by Mushtukov et al. (2021), which is based on a Monte Carlo approach.

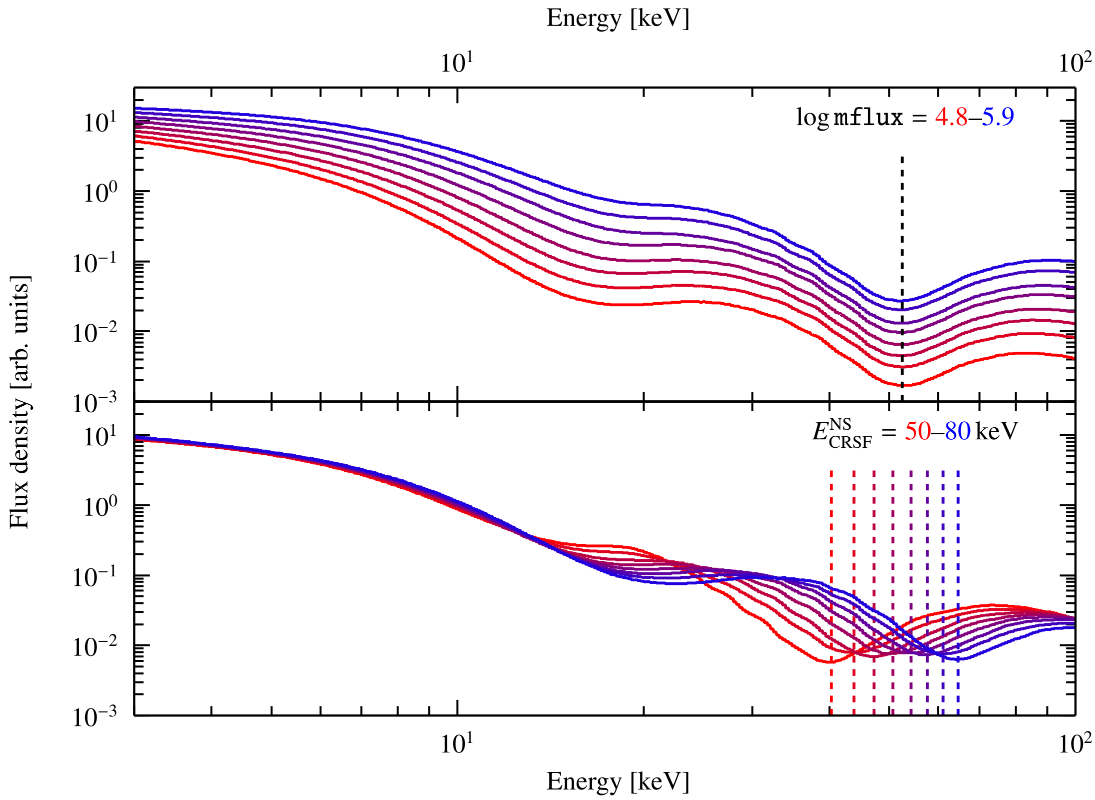

Figure 2.9: The `polcap` model in various parameter configurations. The vertical lines denote cyclotron line energy in the observer's frame for the respective configuration.

2.8 Pulse profiles

The temporal emission characteristic by neutron stars is determined by their rotation and the accretion onto their magnetic poles (for dipole geometry they are connected by the magnetic axis), where high-energy radiation is emitted.

The regular obstruction and change in viewing angle of the emitting regions therefore lead to a highly time-variable signal, whose decomposition allows us to study the geometry of the neutron star (see, e.g., Thalhammer et al., 2024; Pétri et al., 2024). Accreting neutron stars therefore fulfill all prerequisites to act as a cosmic lighthouse, which sends out pulsed signals, where both the pulse period and the shape of the transmitted signal are often unique. In fact, 14 pulsars were used on the *Voyager*'s Golden Record to provide an accurate description of the solar system's position within the cosmos, allowing potential discoverers of the probe to triangulate the senders of the message[8]. In general, the pulse-phase variability of accreting pulsars is much higher than that of radio pulsars due to the accretion process and the subsequent change in viewing angle and obscuration of the X-ray emitting region.

In this section, I will therefore focus in accreting pulsars, specifically HMXBs. Typical pulse periods are on the order of 10^{-3}–10^{3} s, spanning 6 orders of magnitude. This large range is often attributed to changes of the rotation period over the pulsar lifetime. Johnston & Karastergiou (2017) note that most young pulsars are thought to have short pulse periods of tens of ms such as the Crab pulsar (33 ms, see, e.g., Lyne et al., 2015). Transfer of angular momentum onto the neutron star can lead to both spin-up and spin-down effects, both in the short term (events) and in the long term, which provides an explanation for the existence of both slowly rotating neutron

[8]See `https://www.johnstonsarchive.net/astro/pulsarmap.html`

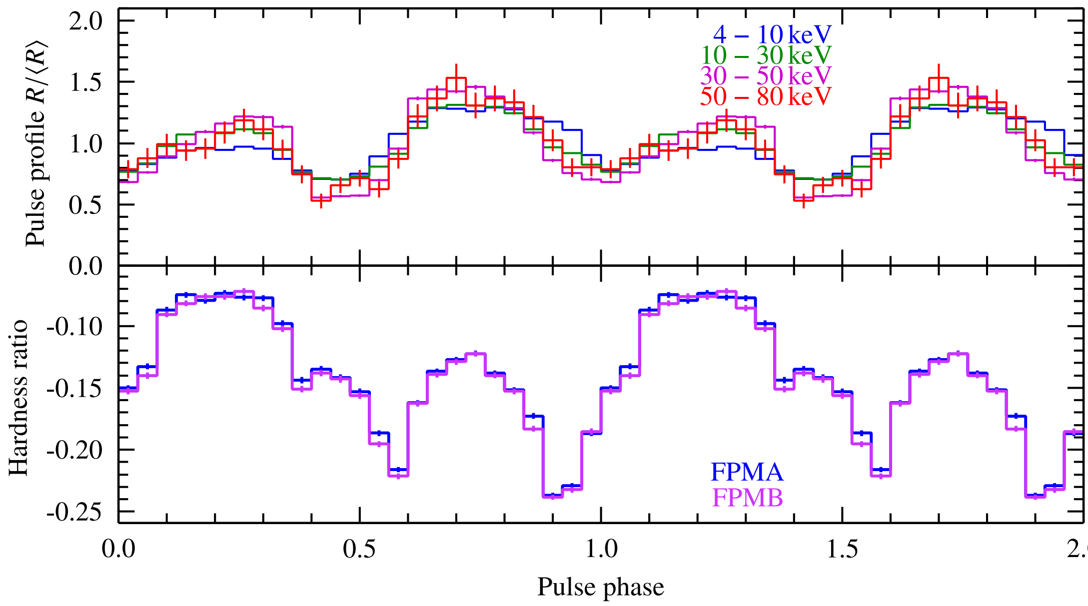

Figure 2.10: Behavior of GX 301−2 over the pulse phase. Top panel: pulse profile in different X-ray energy bands. Bottom panel: hardness ratio defined as $(H - S)/H + S)$, where S is the pulse profile in the 4–10 keV range and H the pulse profile in the 10–30 keV range. Figure adapted from Zalot et al. (2024).

stars such as GX 301−2 (671 s, see, e.g., Zalot et al., 2024) and millisecond pulsars such as PSR B1855+09 (5.3 ms, see, e.g., Kaspi et al., 1994).

In order to determine the pulse period for a given signal, the event file or its derived light curve can be used: epoch folding (see, e.g., Leahy et al., 1983) is a method in which the light curve is folded on different test periods usually spaced on a grid, from which the period that matches the observed signal best can be selected using hypothesis testing. Folding the data on the obtained period yields the *pulse profile*.

The characteristics of the pulsations can be denoted using pulse profiles, where the intensity or flux is shown as function of pulse phase. Such a pulse profile along with the corresponding hardness ratio is shown in Fig. 2.10. The hardness ratio is often defined as

$$\mathrm{HR} = \frac{H - S}{H + S} \tag{2.22}$$

where H and S are the pulse profiles in a hard and soft band, respectively. The hardness ratio therefore shows the contributions of the two respective bands to the observed profile and how *hard* or *soft* the given spectrum for a given pulse phase is.

The fraction of pulsed radiation of the overall received signal is naturally called *pulsed fraction*, one common definition of it is

$$\mathrm{PF}_{\mathrm{minmax}} = \frac{\max(C(\phi)) - \min(C(\phi))}{\max(C(\phi)) + \min(C(\phi))}, \tag{2.23}$$

where $C(\phi)$ is the number of counts at pulse phase ϕ. Apart from showing the count rate density or energy flux as a function of energy in a “regular” spectrum, one can also show the pulsed fraction as a function of energy in a *pulsed fraction spectrum*. Ferrigno et al. (2023) show that the analysis of pulsed fraction spectra allows to extract information about cyclotron resonant scattering features, as the pulsed fraction decreases notably at their centroid energies.

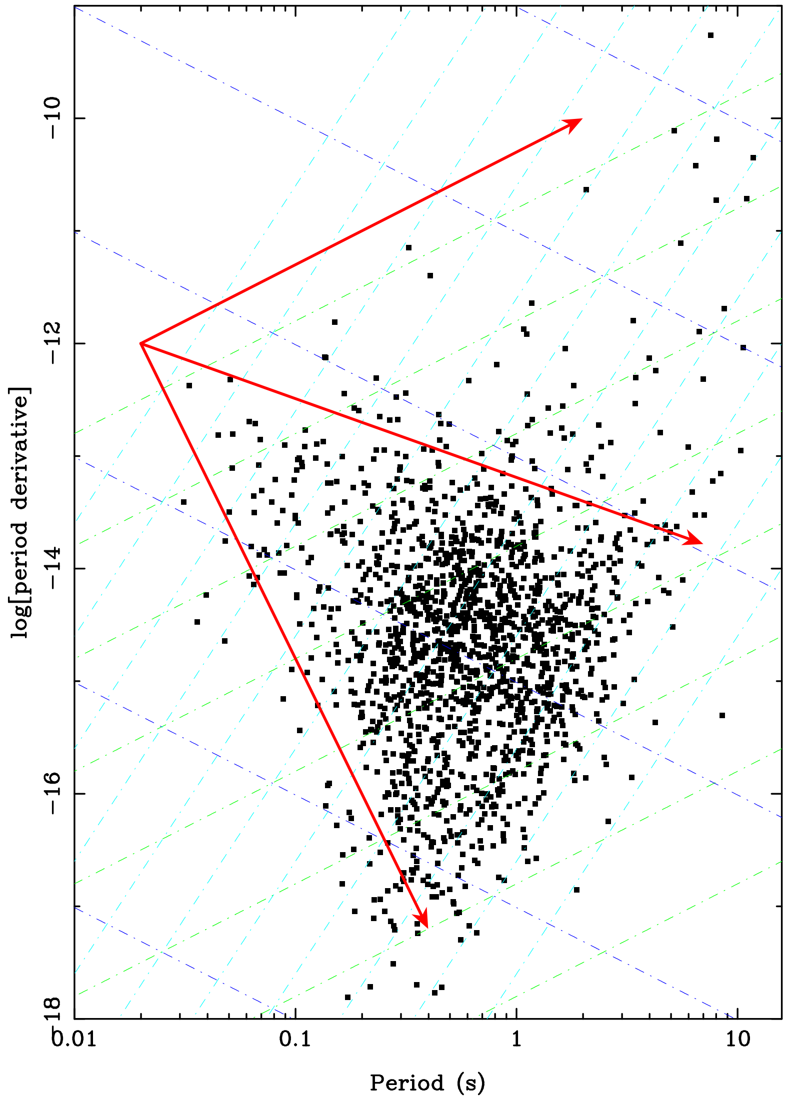

Figure 2.11: P-$\dot{P}$ diagram. The black dots resemble ∼1600 pulsars. Dashed dark blue lines resemble lines of constant magnetic field strength, dashed green lines resemble lines of constant characteristic age, $\tau_c = P/(2\dot{P})$, and dashed light blue lines resemble lines of constant spin-down energy, $\dot{E} = 4\pi^2 I \dot{P} P^{-3}$, where I is the moment of inertia of the star. The red arrows resemble evolutionary paths from a initial configuration of $P = 20\,\mathrm{ms}$ and $\dot{P} = 10^{-12}$ for differing braking indices. Figure reproduced from Johnston & Karastergiou (2017).

Many HMXBs show changes in pulse period during spin-up (see, e.g., Koh et al., 1997; Nabizadeh et al., 2019) or spin-down (see, e.g., Baykal et al., 2001) events. For HMXBs, changes in spin period are understood to be related to angular momentum transfer by the accreted matter, which can apply a torque on the neutron star and increase or decrease its angular momentum and thereby affecting the spin period (Postnov et al., 2015). Radio pulsars also show a change in spin period, as their X-ray luminosity stems from rotational energy; in order to emit radiation they must therefore decrease their spin frequency (see, e.g., Possenti et al., 2002). More generally for all pulsars, the pulse period P and its temporal derivative $\dot{P}$ are key characteristics and can be used to divide the population. Johnston & Karastergiou (2017) show $\dot{P}$ as a function of P, which is often called a P-$\dot{P}$ diagram in the literature. Their diagram is reproduced here in Fig. 2.11. As indicated by the red arrows in the figure, young pulsars start in the upper left corner with short rotation periods and comparably high pulse period derivatives. Magnetars (see Kaspi & Beloborodov, 2017, for an extensive review), are in the upper right corner of the diagram with magnetic field strengths exceeding 10^{13} G. Johnston & Karastergiou (2017) also point out the "death line" at $\dot{E} \sim 10^{30}\,\mathrm{erg\,s^{-1}}$, below which not even radio emission is thought to be possible. The majority of pulsars can however be found in a approximately circular shape at intermediate spin periods of 0.1–1 s and moderate spin derivatives of 10^{-13}–10^{-16}.

3 | Data acquisition and methods

This chapter focuses on the relevant aspects of obtaining, processing, and analysing X-ray spectra. I introduce the space-based observatories from which X-ray spectra analyzed in this work are obtained in Sect. 3.1. The data reduction is discussed in Sect.3.2. Software packages utilised are listed in Sect.3.3. The required statistical methods for analysing and modeling X-ray spectra are described in Sect.3.4.

3.1 X-ray satellites

Over the past decades a variety of X-ray missions have been launched so that there are a significant number of active X-ray missions which serve different purposes with regards to mission goals, availability to general proposers and many other properties. Due to the absorption of X-rays from Earth's atmosphere, X-ray observatories are predominantly onboard satellites in order to be able to observe X-ray radiation.

I outline the general operating principle of X-ray observatories in Sect. 3.1.1. I further introduce three X-ray observatories directly used in this work: the NUclear Spectroscopic Telescope ARray (*NuSTAR*, see Sect. 3.1.2), the Neil Gehrels Swift Observatory (*Swift*, see Sect. 3.1.3) and the X-ray Multi-Mirror-Mission (*XMM-Newton*, see Sect. 3.1.4). One of the most profound differences of the mentioned missions is their respective spectral range and their sensitivity to X-ray radiation within that band, which is resembled by the effective area A_{eff}. I show the effective areas of the aforementioned X-ray observatories Fig. 3.1.

3.1.1 General operating principle

In this section I provide a brief description of incident X-ray photons are focused, measured, and processed onboard space-based X-ray observatories. As an example, a schematic for the *Chandra* X-ray observatory (Weisskopf et al., 2000) is shown in Fig. 3.2. Due to their high energies, X-ray photons cannot be focused as easily as optical photons, whose energies are lower by a factor of 10^3–10^5. To focus X-rays photons concentric mirrors are utilized, which often consist of paraboloid mirrors followed by hyperboloids. This setup is called a Wolter I type X-ray telescope (see, e.g., Werner, 1977). The Einstein Observatory (otherwise known as HEAO-2, see, e.g., McCray et al., 1982) was the first space-based focusing X-ray telescope. In order to increase their reflectivity, the mirrors are often coated with highly reflective materials such as iridium for *Chandra* and Platinum on Carbon Catalyst (Pt/C) for *NuSTAR* (see Weisskopf et al., 2000; Harrison et al., 2013, respectively). The incident photons therefore undergo two internal reflections, that is once on each mirror type, before propagating onwards towards the focal point. The measurement devices are usually not positioned directly at the focal point, since this would not allow to obtain spatial information about the incident radiation. Instead, slightly closer towards the mirrors a focal surface is positioned, on which an imaging detector, usually a Charged Coupled Device (CCD) detector, is placed.

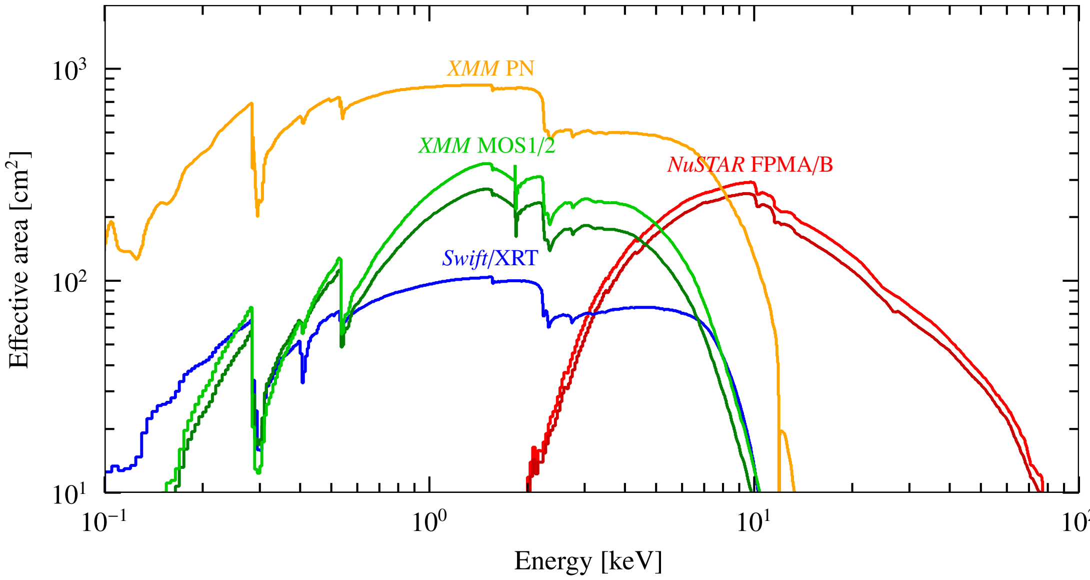

Figure 3.1: Effective areas of selected operating X-ray observatories. The *Swift*/BAT instrument is intentionally excluded as it only provides fluxes and no spectral information per se.

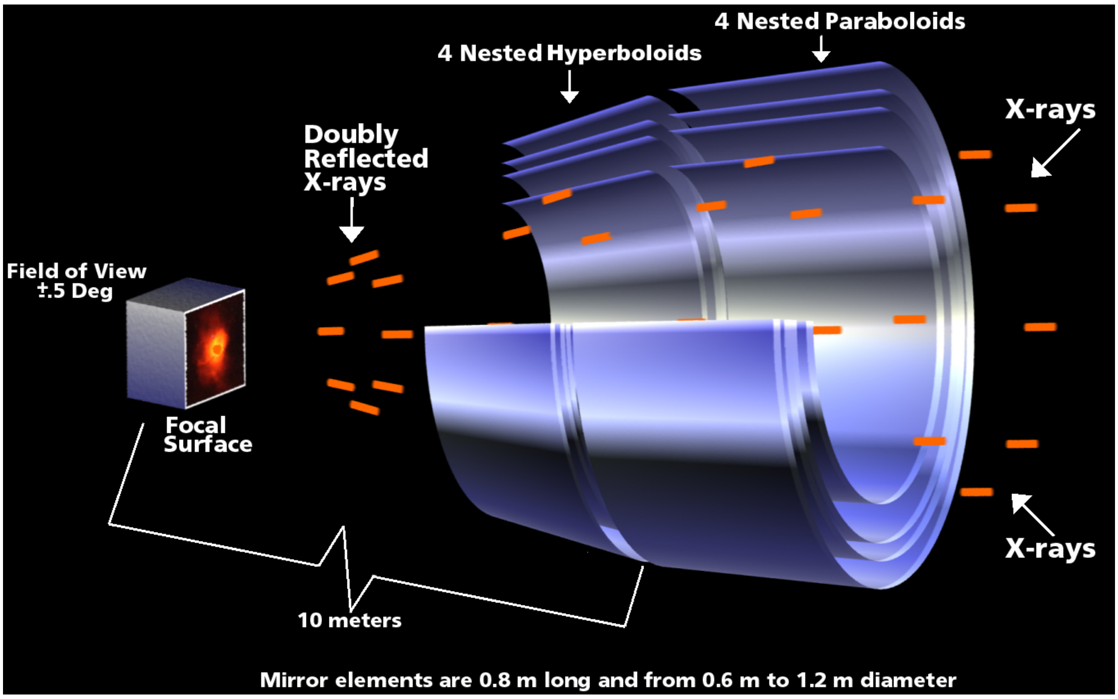

Figure 3.2: Schematic of grazing incidence optics of *Chandra*. Image: NASA/CXC/D. Berry (See `https://chandra.harvard.edu/resources/illustrations/teleSchem.html`)

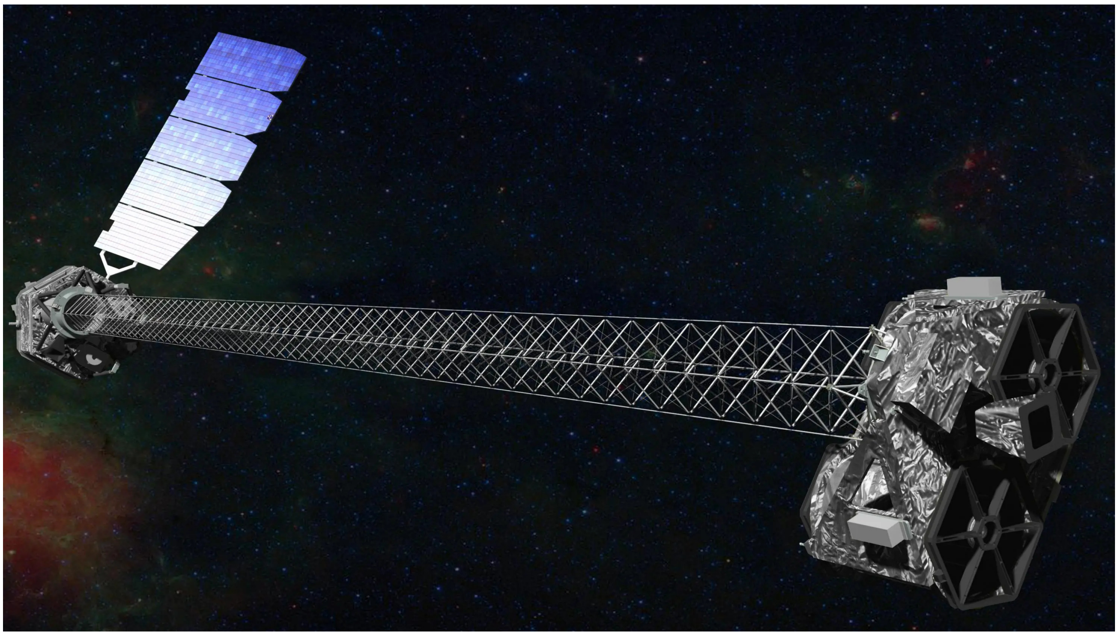

Figure 3.3: Artistic impression of the NUclear Spectroscopic Telescope ARray. Image: NASA/GSFC (See `https://science.nasa.gov/mission/nustar`)

CCD detectors utilize semiconductors to indirectly measure an incident photon's energy by collecting electrons within a pixel, where the number of electrons within the pixel is directly proportional to the photon energy. The detector consists of a grid of individual pixels, which are either read out periodically (integrated readout) or triggered by each incoming X-ray photons (triggered readout), which is naturally only feasible at high energies such as X-rays and impossible in the optical regime.

By the pixelated design and, in the case of *NuSTAR*, triggered readout, information about the spatial origin, arrival time and energy of individual photons can be obtained. This is highly advantageous for many different applications, for example spatial information is vital to estimate the background radiation, the arrival time of individual photons is naturally important for timing analyses such as pulse period searches and the investigation of quasi-periodic oscillations (see, e.g., Heindl et al., 1999, for 4U 0115+63). The spatial information of the X-ray is further useful to create images of the observed sky region. The field of view (FOV) of such a telescope is usually below 1°, for example the *Chandra*/ACIS instrument has a FOV of $17'$ and *NuSTAR* 10' for photon energies of 10 keV [1]. For a full description of the Cadmium Telluride pixel detector onboard *NuSTAR*, see Miyasaka et al. (2009).

3.1.2 The Nuclear Spectroscopic Telescope Array

The NUclear Spectroscopic Telescope ARray (*NuSTAR*) is a broadband (3.0–78.4 keV) imaging X-ray observatory (Harrison et al., 2013). It was launched on June 13, 2012 and is on a low Earth orbit with 6° inclination and expected orbital lifetime of 10 years, which is has already exceeded. Its most distinct feature is its 10.14 m long deployable mast, that was deployed after launch and separates the Wolter-I conical approximation X-ray optics (see, e.g., Petre & Serlemitsos, 1985) from the detectors. The detector consists of two focal plane modules FPMA and FPMB, which each consist of a 2×2 array of CdZnTe pixel detectors (Harrison et al., 2010) with 32×32 pixels, resulting in a total field of view of 12' for each module. With a pixel size of 0.6 mm, each pixel

[1] Since the reflectivity of the mirrors depends on the photon energy, so does the FOV.

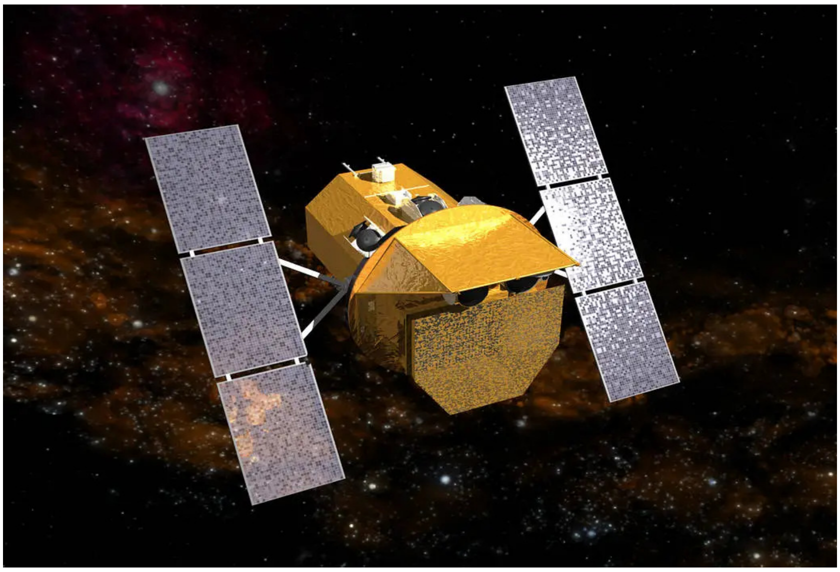

Figure 3.4: Artistic impression of the Neil Gehrels *Swift* Observatory. Image: NASA/GSFC (See `https://www.nasa.gov/image-article/neil-gehrels-swift-observatory/`)

theoretically covers 12.3”; Harrison et al. (2013) report FWHM angular resolutions of 10” and 6” at photon energies of 10 keV and 68 keV, respectively.

Each *NuSTAR* energy bin has a width of 40 eV. The FWHM energy resolution in the soft X-ray band (quoted at 10 keV) is 400 eV, at 69 keV Harrison et al. (2013) report an energy resolution of 900 eV. This energy resolution is sufficient to detect prominent emission lines in the soft X-ray band such as the Fe Kα and Fe Kβ lines; narrower and weaker emission lines are generally not expected to be resolvable and also not detected in this work.

The fact that apart from time and energy also the detector position of photons is registered, i.e. the fact that *NuSTAR* is an imaging instrument, allows the user to estimate the background directly by choosing a background region (see Fig. 3.6), which is then taken into account when applying spectral models. For more sophisticated background treatment, *NuSTAR*’s background has been modeled (Harrison et al., 2010; Wik et al., 2014), which includes various internal lines at energies of 20–30 keV, the cosmic X-ray background (CXB, see, e.g., Krivonos et al., 2021), solar X-rays and an internal continuum.

With a temporal resolution of 2 μs *NuSTAR* is more than capable to detect pulsations of accreting pulsars, whose shortest periodic signals are expected to be on the order of 10^{-3} s. Apart from a yearly General Observer Program[2], *NuSTAR* also performs Target of Opportunity (ToO) observations with claimed response times <24 hours. Such observations are useful to observe transient outbursts, which require short-notice observations due to their very nature. An artistic impression of *NuSTAR* is shown in Fig. 3.3.

3.1.3 The Neil Gehrels Swift Observatory

The Neil Gehrels Swift observatory (*Swift*, formerly the Swift Gamma-Ray Burst Mission, Gehrels et al., 2004) consists of three telescopes: the Ultra-Violet/Optical Telescope (UVOT, Roming et al., 2005), the Burst Alert Telescope (BAT, Barthelmy et al., 2005; Krimm et al., 2013) and the X-ray Telescope (XRT, Burrows et al., 2005).

[2]See `https://heasarc.gsfc.nasa.gov/docs/nustar/nustar_prop.html`

Of special interest for this work are of course the two instruments operating in the X-ray band, the UVOT can however still be relevant in the context of HMXBs, for example to identify optical counterparts to X-ray emitting compact objects. As the name of the mission suggests, the BAT instrument primarily focuses on the detection of Gamma-Ray bursts, it however also monitors the X-ray sky in the 15–50 keV energy range and provides daily fluxes for a list of well-known HMXBs among others[3] since 2006. It is therefore very well suited to provide long-term light curves of X-ray sources and alert the community to outbursts of transient sources, which can then trigger follow-up observations with broadband X-ray observatories such as *NuSTAR*. It is however important to remember that the BAT itself provides only *fluxes*, but no *spectra*.

The X-ray instrument onboard *Swift* operates in the soft X-ray band at 0.2–10 keV. As an imaging instrument based on a 600×600 pixel CCD detector corresponding to a field of view of $23.6' \times 23.6'$, its primary scientific mission is to constrain the position of Gamma-Ray bursts and measure their X-ray spectra. As part of its general observer program, also observations of X-ray binaries are carried out.

XRT observations usually consists of frequent short pointing observations with exposure times of $\sim$1 ks, which are ideal to follow transient sources over outbursts (see, e.g., Rykoff et al., 2007). The XRT provides valuable data in the soft X-ray band, which is critical to constrain the absorption between source and observer (see, e.g., Willingale et al., 2013). In this work, simultaneous or nearly simultaneous XRT observations with *NuSTAR* observations are used for this purpose. An artistic impression of *Swift* is shown in Fig. 3.4.

3.1.4 The X-ray Multi-Mirror-Mission

The X-ray Multi-Mirror mission (*XMM-Newton*, Jansen et al., 2001) was launched on December 10 1999 as part of the ESA Horizon 2000 program. Three X-ray telescopes with Wolter-I mirrors are onboard the satellite. The European Photon Imaging Camera (EPIC, Strüder et al., 2001) is an imaging instrument equipped with a pn CCD detector consisting of 398×384 pixels, which can operate in six different modes depending on the expected count rate and scientific goals. In full frame mode, the full CCD area is utilized at the expense of time resolution (73.3 ms) and maximum count rate of $8.1 \times 10^{-12}\,\mathrm{erg\,cm^{-2}\,s^{-1}}$. For higher expected count rates or in cases where sub-ms timing is required, the timing and burst modes are available. For more details see Strüder et al. (2001, Table 1 and Fig. 3). The EPIC operates in the energy range 0.15–15 keV with a spectral resolution of $E/\Delta E \sim 20$—50. *XMM-Newton* is also equipped with two MOS CCD cameras Turner et al. (2001) and a Reflection Grating Spectrometer den Herder et al. (2001). I show an artistic impression of *XMM-Newton* in Fig. 3.5.

3.2 Data reduction

This work is primarily based on the analysis of *NuSTAR* observations; therefore their data extraction reduction is briefly described here, which generally follows the procedure describe in the *NuSTAR* Quickstart guide[4]. Public *NuSTAR* data can directly obtained from the NASA Goddard Space Flight Center (GSFC)[5]. The High Energy Astrophysics Software (HEASoft)[6] contains processing resources for many X-ray missions, including the *NuSTAR*Data Analysis Software (NuSTARDAS). To obtain light curves and event files form the stage 1 data products, the `nupipeline` routine can be utilised. Subsequently, sky images can be computed from the event

[3]See `https://swift.gsfc.nasa.gov/results/transients/`

[4]See `https://heasarc.gsfc.nasa.gov/docs/nustar/analysis/nustar_quickstart_guide.pdf`

[5]See `https://heasarc.gsfc.nasa.gov/cgi-bin/W3Browse/w3browse.pl`

[6]See `https://heasarc.gsfc.nasa.gov/docs/software/lheasoft/`

Figure 3.5: Artistic impression of *XMM-Newton* with Earth in the background. Image: NASA/GSFC (See `https://science.nasa.gov/mission/xmm-newton/`)

files for both detectors, respectively either manually or more conveniently by dedicated software, e.g. `ds9`. In order to estimate the contribution by background radiation to measurement, source and background regions need to be defined, from which source and background spectra can be extracted. In this work, for each astrophysical source and detector the source region is chosen to be a circle that encloses the visible point source. Its radius is chosen to be sufficiently large to capture as many source events as possible, which is especially important for observations at low luminosity. To estimate the background radiation as precisely as possible its region should be as large as possible, here I use annuli centered on the point source as background regions. As an example, the sky image of X Persei is shown in Fig. 3.6 with the corresponding source and background regions.

From the previously obtained level 2 data products and the selected regions source and background spectra can be obtained using the `nuproducts` routine. The routine offers many optional filters, which can be used to obtain energy-, time- or pulse phase-filtered spectra. The extracted spectra can then be further analyzed with dedicated spectral analysis software packages, which are discussed below.

3.3 Software packages

The large amounts of data generated by space-based observatories naturally suggests to utilize computer programs for their analysis. For high-energy spectra, more specifically X-ray spectra, there are multiple open-source software packages available designed for this purpose. The X-ray

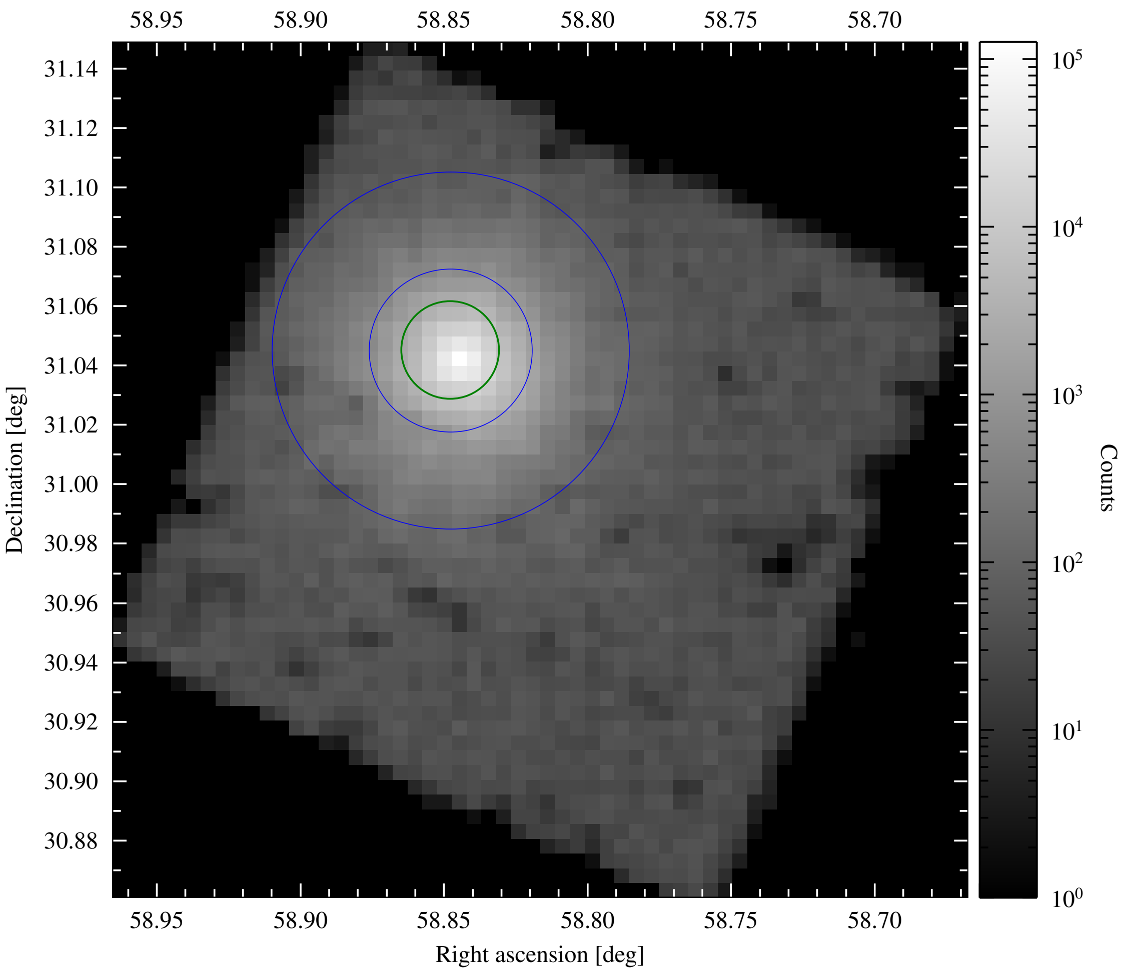

Figure 3.6: *NuSTAR*/FPMA sky image of X Persei. The green circle denotes the source region used for the extraction, the two blue circles denote the annulus region used for the estimation of the background radiation.

SPECtral fitting package (XSPEC Arnaud, 1996; Dorman & Arnaud, 2001)[7], which was initially developed at the Institute of Astronomy in Cambridge is a command-line based package to analyze and model X-ray spectra. It includes a large library of phenomenological and physical model components, which can be combined to develop models for X-ray emission of various objects. More recently, a python version of the package has been published as well [8].

The Massachusetts Institute of Technology has meanwhile developed another software package for X-ray spectra, that is based on the S-Lang interpreted programming language[9] by John E. Davis. The Interactive Spectral Interpretation System (Houck & Denicola, 2000)[10] can also be used to model X-ray spectra with the same models as in XSPEC, but has crucial advantages over its counterpart: both ISIS and XSPEC can be used form a command-line interface; ISIS however also allows the user to write executable scripts, which allow to automate certain tasks and simplify their repeated execution. Furthermore, ISIS includes functionality for parallelization of complex computations, e.g., estimation of fit parameter confidence intervals. The natively

[7] See `https://heasarc.gsfc.nasa.gov/xanadu/xspec/`
[8] See `https://heasarc.gsfc.nasa.gov/docs/xanadu/xspec/python/html/index.html`
[9] See `https://jedsoft.org/slang/`
[10] See `https://space.mit.edu/CXC/isis/index.html`

implemented features of ISIS are supplemented by the Remeis ISISscripts[11], which are a large collection of useful ISIS functions and routines.

A further useful resource for the reduction and processing of X-ray spectra is the High Energy Astrophysics Software (HEASoft)[12], which provides useful routines for high-level data products for a large number of active and past X-ray missions. In this work, all spectral analysis is conducted with ISIS version 1.6.2 and HEASoft version 6.33.0.

3.4 Statistics

The spectral analysis of X-ray spectra often entails the development of one or more spectral models to describe the measured spectrum. To determine the to which degree a model can reproduce an observed spectrum, statistical methods are required. In Sect. 3.4.1, I outline the derivation of the χ^2-statistic; the same is shown for the Cash statistic in Sect. 3.4.2 and the W-Statistic in Sect. 3.4.3. I further focus on their properties and use cases.

3.4.1 χ^2 statistic

The χ^2-statistic is the most commonly used statistic to assess the goodness of fit not only in X-ray astronomy, but in many different sciences as well. Here, I focus on the derivation in the context of astrophysical spectra and follow the mathematical description outlined in the appendix of the XSPEC manual[13]. The starting point for the derivation of the statistic is the underlying question: what is the probability to measure the observed spectrum for a given model? For Gaussian-distributed data, the likelihood can therefore be expressed as

$$L = \prod_{i=1}^{N} \frac{1}{\sqrt{2\pi}\,\sigma_i} \exp\left[\frac{-\left(y_i - f(x_i, \vec{\Theta})\right)^2}{2\sigma_i^2}\right] \tag{3.1}$$

where N is the number of data bins, y_i the observed number of counts in bin i, σ_i the uncertainty of the data counts, $f(x_i, \vec{\Theta})$ the number of counts predicted by the model with parameters $\vec{\Theta}$. For a given, in the best case physically motivated model it is desirable to determine the parameters $\vec{\Theta}$ that maximise the likelihood. There are at least two obstacles that complicate or even prevent the direct use of the maximum likelihood for the determination of the best-fit parameters:

1. In computer science it is often desirable for a set of parameters that *minimizes* a given function; there are therefore far more minimizing algorithms available than algorithms maximising a quantity.

2. At least in the past decades, the multiplication of two floating-point numbers is more computationally expensive than adding them. Eq. 3.1 implies the multiplication of all N individual probabilities. Since N is typically on the order of few hundreds for X-ray spectra (and is expected to significantly increase with new high-resolution instruments such as *XRISM*/Resolve) it is desirable to circumvent the repeated multiplication.

Mathematically, the above problems can be solved by taking the natural logarithm of the likelihood and thus converting multiplications to sums and taking the negative value, so that the minimum of the new function is the desirable result. One obtains

$$-\log(L) = \sum_{i=1}^{N} \log\left(\sqrt{2\pi}\sigma_i\right) + \frac{\left(y_i - f(x_i, \vec{\Theta})\right)^2}{2\sigma_i^2} \tag{3.2}$$

[11] See `https://www.sternwarte.uni-erlangen.de/isis/`
[12] See `https://heasarc.gsfc.nasa.gov/docs/software/lheasoft/`
[13] See `https://heasarc.gsfc.nasa.gov/xanadu/xspec/manual/XSappendixStatistics.html`

One can see that the first term only depends on the data and can therefore be dropped. Further multiplication with 2 to simplify the denominator of the second factor yields the χ^2-statistic

$$\chi^2 = \sum_{i=1}^{N} \frac{\left(y_i - f(x_i, \vec{\Theta})\right)^2}{\sigma_i^2}. \tag{3.3}$$

In the case that the fit model describes the data reasonably well, $\chi^2(\vec{\Theta})$ is χ^2-distributed. As the expected value of the χ^2 distribution is

$$\langle \chi^2 \rangle = N_{\text{d.o.f.}} \tag{3.4}$$

with $N_{\text{d.o.f.}} = N_{\text{bins}} - N_{\text{free parameters}}$ the number of degrees of freedom, one expects the fit statistic to approach this value and further implies that the reduced χ^2 defined as

$$\chi^2_{\text{red}} = \frac{\chi^2}{N_{\text{d.o.f.}}} \tag{3.5}$$

approaches 1 for a sufficiently good fit. $\chi^2_{\text{red}} < 1$ implies that the data is *overfitted* and too many model components are utilized to describe the data.

It is important to note that minimising the χ^2-statistic in order to fit a model to data should only be done in the case of Gaussian uncertainties. In ISIS the data uncertainty is estimated based on Poisson statistics, where for a λ measured counts the uncertainty is $\sqrt{\lambda}$. As for sufficiently large λ the Poisson distribution approaches the Gaussian distribution it is fair to take the uncertainties as Gaussian uncertainties, which is however not necessarily for low-luminosity observations or energies with low effective areas and subsequent low observed number of counts.

3.4.2 Cash statistic

For distributions where the assumption of Gaussian uncertainties does not hold a different statistic is required to assess the goodness of fit. In the field of X-ray astronomy this is required for observations at the low luminosities. Cash (1979) suggested a Poisson statistic based fit statistic, which is now known as the Cash statistic. It can be derived in similar fashion as done in Sect. 3.4.1 from the Poissonian likelihood

$$L = \prod_{i=1}^{N} \frac{\left[f(x_i, \vec{\Theta})\right]^{y_i} e^{-f(x_i)}}{y_i!}. \tag{3.6}$$

Taking twice the negative natural logarithm yields the statistic proposed by Cash (1979)

$$C = 2 \sum_{i=1}^{N} f(x_i, \vec{\Theta}) - y_i \cdot \log\left[f(x_i, \vec{\Theta})\right] + \log(y_i!). \tag{3.7}$$

One can see that the last term only depends on the data and is often approximated using Stirling's approximation[14] in literature, which yields the familiar form of the Cash statistic

$$C = 2 \sum_{i=1}^{N} f(x_i, \vec{\Theta}) - y_i + y_i \cdot \log\left(\frac{y_i}{f(x_i, \vec{\Theta})}\right). \tag{3.8}$$

It is important to note that the minimization of the Cash statistic can not necessarily achieved with the same algorithms as for the χ^2-statistic: for example the Levenberg-Marquart algorithm

[14] for large n: $\log(n!) \approx n \cdot \log n - n$

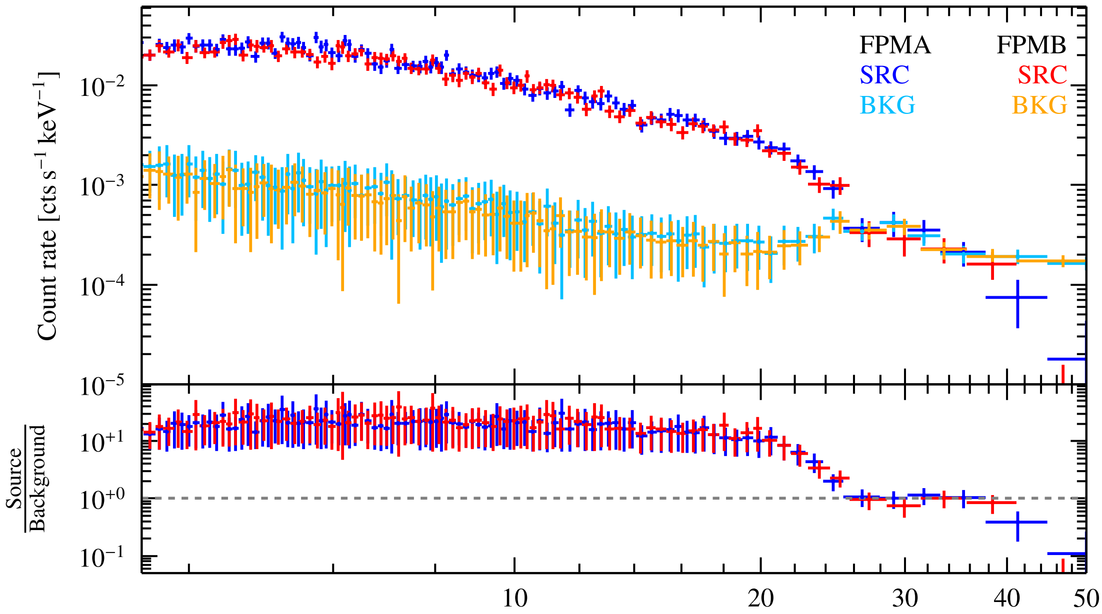

Figure 3.7: Background-dominated *NuSTAR* spectrum of Cepheus X−4. Top panel: background-subtracted source spectra and background spectra of 2023 *NuSTAR* observation of Cepheus X−4 of both focal plane modules. Bottom panel: Ratio between source and background count rates. The dashed line indicates a ratio of unity.

(`mpfit` in ISIS, see Levenberg, 1944; Marquardt, 1963), that is often the algorithm of choice in ISIS, does not minimize the C-statistic. One therefore has to utilize other algorithms such as the `subplex` algorithm, which generally requires more iterations to reach convergence, therefore significantly increasing the CPU time required, especially for complex tasks such as parameter uncertainty estimations.

3.4.3 W-Statistic

Both the χ^2-statistic and Cash statistic do not take the background spectrum into account. This may be problematic in cases where the background signal is not significantly weaker than the source signal. Such a case is shown in Fig. 3.7, where I show the spectrum of Cepheus X−4 from a 2023 *NuSTAR* observation.

It is evident that above ∼25 keV the spectrum becomes background-dominated, making scientific analysis without consideration of the background practically impossible.

One method to tackle this problem is the use of a statistic that takes the background into account. The W-statistic does exactly that, as it is based on Poisson statistics for both the source and background spectrum. Its likelihood can be expressed as

$$L = \prod_{i=1}^{N} \underbrace{\frac{[t_s\,(m_i + b_i)]^{S_i} \exp\left[-t_s\,(m_i + b_i)\right]}{S_i!}}_{\text{Source Poisson term}} \times \underbrace{\frac{(t_b\,b_i)^{B_i}\,e^{-t_b b_i}}{B_i!}}_{\text{Background Poisson term}} \tag{3.9}$$

where $t_{s,b}$ are exposure times of the source and background observation, respectively, S_i and B_i are the source and background count values, respectively, m_i is the model rate (in units of cts s^{-1}), b_i is the *predicted* background rate, whose definition is given further below. Similarly, but less trivially, taking twice the negative logarithm of Eq. 3.9 and applying the Stirling approximation where possible gives the W-Statistic

$$W = 2 \cdot \sum_{i=1}^{N} t_s \cdot m_i + b_i \cdot (t_s + t_b) - S_i \cdot [\log (t_s \cdot (m_i + b_i)) - \log S_i + 1] - B_i \cdot [\log (t_b b_i) - \log B_i + 1]. \tag{3.10}$$

Unless given by a dedicated background model, the background count rates b_i have to be calculated. Here, we choose the b_i for each bin such that they maximise the W-Statistic, that is where

$$\frac{\partial W}{\partial b_i} = 0. \tag{3.11}$$

and call the determined value f_i. Differentiating Eq. 3.10 with respect to b_i and solving the following quadratic formula requires the following distinction: if $(t_s + t_b) \cdot m_i - S_i + B_i \geq 0$, then

$$f_i = \frac{S_i + B_i - (t_s + t_b) \cdot m_i + d_i}{2(t_s + t_b)}, \tag{3.12}$$

otherwise

$$f_i = \frac{2B_i m_i}{S_i + B_i - (t_s + t_b) \cdot m_i + d_i}. \tag{3.13}$$

In the above two expressions d_i corresponds to the square root of the discriminant obtained while solving the quadratic formula and can be expressed as

$$d_i = \sqrt{[(t_s + t_b) \cdot m_i - S_i - B_i]^2 + 4 \cdot (t_s + t_b) B_i m_i}. \tag{3.14}$$

One can further see that Eq. 3.10 is not defined in the case where $S_i = 0$ or $B_i = 0$. In the first case, the contribution is calculated as

$$W_i = 2 \cdot \left(t_s m_i - B_i \cdot \log \frac{t_b}{t_s + t_b} \right) \tag{3.15}$$

If $B_i = 0$, one distinguishes the case where the model rate is lower than the source rate, i.e. if $m_i < S_i/(t_s + t_b)$, in which case

$$W_i = 2 \cdot \left(-t_b m_i - S_i \cdot \log \frac{t_s}{t_s + t_b} \right), \tag{3.16}$$

otherwise the contribution is simply the Cash statistic, i.e.,

$$W_i = 2 \cdot [t_s m_i + S_i \cdot (\log S_i - \log(t_s m_i) - 1)]. \tag{3.17}$$

In comparison to the above two statistics, the W-statistic may seem not as straightforward, which is a result of the consideration of the background. The implementation of the W-Statstic in ISIS was performed as a part of this work in collaboration with Jakob Stierhof and Deniz Demirci.

4 | X-ray observations of Be X-ray binaries

This section covers my original work and research on high-mass X-ray binaries harboring pulsars transitioning to and in quiescence. Sect. 4.1 provides an overview over those Be X-ray binaries which are the main subject of this work. In Sect.4.2, I discuss the spectral transition which GRO J1008−57 undergoes from its bright to quiescent state as observed with *NuSTAR*. Subsequently in Sect. 4.3, I show the pulse profile evolution with luminosity of GRO J1008−57 as well as pulse profiles of various sources at low luminosities. In Sect. 4.4, I discuss the cyclotron resonant scattering feature of Cepheus X-4 and investigate how well the feature can be constrained with different fit statistics in order to understand whether the use of more complex statistics benefits the spectral analysis in this case. In Sect. 4.5, I aim to obtain a empirical description of the double-hump structure present in the quiescent spectra of BeXRBs. Building on said description, in Sect. 4.6 I use it to estimate the magnetic field strength and compare it with results obtained from theoretical simulations.

4.1 Overview of selected low-luminosity sources

Prior to the analysis of BeXRBs in quiescence, I performed a literature and database study in order to obtain a set of BeXRBs, for which high-quality broadband *NuSTAR* spectra are available. I select the following nine sources, for which I provide a brief overview over their properties and history before continuing with the analysis of the corresponding observations.

4.1.1 2RXP J130159.6-635806

2RXP J130159.6-635806 was discovered by Kaspi et al. (1995). The analysis by Chernyakova et al. (2005) suggests a classification as a high-mass X-ray binary with Be companion. They further report that the X-ray spectrum is typical for that of high-mass X-ray binaries. Masetti et al. (2006) and later Coleiro et al. (2013) identify the optical counterpart as a Be star. The system's photogeometric distance as determined with *Gaia* is $5.4^{+2.6}_{-1.5}$ kpc (Gaia Collaboration, 2016, 2023; Bailer-Jones et al., 2021). More recently, Krivonos et al. (2015) studied a *NuSTAR* observation of the source and also find a typical X-ray pulsar spectrum and strong pulsations with a pulsed fraction of ~80%. They further state that the source shows low, but persistent flux and neither type I or type II outbursts.

4.1.2 A0535+26

A0535+26 was first discovered by Rosenberg et al. (1975), who report a flat X-ray spectrum (3–7 keV) and pulsations at a period of 104 s. Since then, it has been observed many times and is a well-studied X-ray pulsar (see, e.g., Motch et al., 1991; Giovannelli & Graziati, 1992; Haigh et al., 2004). Its optical companion has been classified as a Be star (Li et al., 1979). The photogeometric distance is $1.77^{+0.07}_{-0.06}$ kpc (Gaia Collaboration, 2016, 2023; Bailer-Jones et al., 2021). The source's observed type I and type II outbursts can possibly be explained by a disc truncation mechanism, with a Be decretion disk with a disk parameter $\alpha \gtrsim 0.1$ (Okazaki & Negueruela, 2001). More recently, Ballhausen et al. (2017) and Tsygankov et al. (2019a) analyzed *NuSTAR* observations of A0535+26 during its low luminosity state. Tsygankov et al. (2019a) find that the X-ray spectrum fundamentally changes at low luminosities. The source is known to have a CRSF at ~45 keV, which is discussed in detail by Ballhausen et al. (2017).

4.1.3 Cepheus X-4

Cepheus X-4 is a Be high-mass X-ray binary system that was discovered by Ulmer et al. (1973). Its Be companion was identified by Bonnet-Bidaud & Mouchet (1998). Its photogeometric distance is $7.2^{+0.8}_{-0.7}$ kpc (Gaia Collaboration, 2016, 2023; Bailer-Jones et al., 2021). Koyama et al. (1991) and Mihara et al. (1991) independently detect pulsations in *Ginga* data from Cepheus X-4's 1988 outburst. Mihara et al. (1991) further discover a cyclotron line centered at ~30 keV. *NuSTAR* observations of its 2014 outburst indicate a distorted cyclotron line shape (Fürst et al., 2015). A first harmonic of the CRSF has been found by Vybornov et al. (2017), who further report a positive correlation of the fundamental CRSF energy and X-ray luminosity. Sokolova-Lapa et al. (2023b) report that preliminary studies of observations of Cepheus X-4 during the decline of its 2023 outburst indicate a spectral transition when entering the low luminosity regime.

4.1.4 GX 304−1

GX 304−1 is a Galactic high-mass X-ray binary system located at a distance of $1.85^{+0.06}_{-0.05}$ kpc (Gaia Collaboration, 2016, 2023; Bailer-Jones et al., 2021). It was independently discovered by Lewin et al. (1968a,b) during a balloon flight over Australia and by McClintock et al. (1977) using the SAS-3 satellite in the year 1977. The later report pulsations at a period of 272 s and a single-peaked pulse profile. In the following year, Mason et al. (1978) identify the optical counterpart as a Be star. More recently, Yamamoto et al. (2011) discovered a CRSF centered at 54 keV during GX 304−1's 2010 outburst using *RXTE* and *Suzaku* data. Klochkov et al. (2012) detect a positive correlation between CRSF energy and luminosity form data obtained during the source's 2012 outburst. GX 304−1 has also been studied in its low luminosity state: Rouco Escorial et al. (2018) monitored the source between regular type I outbursts using *Swift* and report that the source exhibits a quasi-stable low luminosity state and generally behaves very similar to GRO J1008−57. They further emphasize that pulsations are detected during the stable low luminosity state and argue that this a strong indicator for mass accretion onto the neutron star in this state. Tsygankov et al. (2019c) compare *NuSTAR* observations of GX 304−1 at luminosities between 10^{34}–10^{37} erg s^{-1} and find a spectral transition towards low luminosities, where the X-ray spectrum shows a double-hump structure consistent with a `comptt+comptt` model. Lastly, Sokolova-Lapa et al. (2021) show that the `polcap` model introduced in Sect. 2.7.3 is able to reproduce the X-ray spectrum of GX 304−1 at low luminosities.

4.1.5 GRO J1008−57

GRO J1008−57 is a Galactic transient Be X-ray binary that was first discovered during its 1993 outburst (Wilson et al., 1994; Stollberg et al., 1993). Its photogeometric distance is $3.52^{+0.17}_{-0.16}$ kpc Gaia Collaboration (2016, 2023); Bailer-Jones et al. (2021). Coe et al. (1994) identified the optical counterpart of GRO J1008−57; the infrared spectrum and Balmer emission lines allowed the identification as a Be star. A broadband X-ray analysis using *ASCA* and *CGRO/OSSE* has shown that the high-energy continuum is well described by a powerlaw with exponential cutoff (Shrader et al., 1999). Coe et al. (2007) conduct a multi-wavelength study in the optical and X-ray band of the source and report an eccentric orbit ($e = 0.68 \pm 0.02$) and an orbital period of $P_{\rm orb} = 247.8 \pm 0.4\,$d. In the optical, they study the Hα line over a period of more than 10 years and relate the outbursts to the binary orbit and circumstellar disk and even provide a linear expression for expected outburst times. More recently, Kühnel et al. (2013) analyze GRO J1008−57's outburst during December 2011 and aimed to predict its type II outbursts. Chen et al. (2021) report a cyclotron line with centroid energy between 75–90 keV, for which they further find a negative correlation with luminosity. Tsygankov et al. (2023) analyzed two observations of GRO J1008−57 by the X-ray Polarimetry Explorer (*IXPE*) and report a magnetic obliquity of $\sim 75°$ which indicates that GRO J1008−57 is nearly an orthogonal rotator[1].

4.1.6 MAXI J0655−013

MAXI J0655−013 was first detected in 2022 by *MAXI*/GSC (Serino et al., 2022) as a hard X-ray transient. A follow-up observation with *Swift*/BAT (Kennea et al., 2022b) confirmed the detection and a *NuSTAR* follow-up observation reveled pulsations at a period of 1129 s (Shidatsu et al., 2022). The source was also detected by the Spektrum-Roentgen-Gamma Astronomical Roentgen Telescope – X-ray Concentrator (SRG/ART-XC, Pavlinsky et al., 2022). Kennea et al. (2022a) identify the optical companion as V520 Mon, a Be star (Zaznobin et al., 2022) located at a photogeometric distance of $3.44^{+0.26}_{-0.21}\,$kpc (Gaia Collaboration, 2016, 2023; Bailer-Jones et al., 2021). The two conducted *NuSTAR* observations in June and August 2022 have been analyzed by Rai et al. (2023), who report a significant spin-up between the two observations of $\sim 1.23\,{\rm s\,d^{-1}}$. The second observation was at a luminosity of few $10^{34}\,{\rm erg\,s^{-1}}$, during which pulsations were also detected. As already suggested for other sources above, Rai et al. (2023) suggest that the detected pulsed radiation at low luminosity could be caused by mass accretion from a cold accretion disk.

4.1.7 MAXI J1409−619

MAXI J1409−619 was first detected by *MAXI*/GSC in 2010 as reported by Yamaoka et al. (2010). They classify the source as an X-ray transient; shortly later *RXTE* observations indicate pulsations at a period of 506 ± 1 s (Yamamoto et al., 2010). Kennea et al. (2010) find a near infrared source located 2.1 arcsecond from the X-ray transient, 2MASS 14080271-6159020 (see, e.g., Skrutskie et al., 2006), and suggest it as the counterpart of MAXI J1409−619. Orlandini et al. (2012) argue that the NIR color indices are consistent with a B-type star when considering Galactic extinction, they therefore suggest that the system is a high-mass X-ray binary system. More recently, Ghimiray et al. (2024) classify the system as a Be X-ray binary. The system's photogeometric distance is $4.4^{+1.2}_{-0.6}\,$kpc (Gaia Collaboration, 2016, 2023; Bailer-Jones et al., 2021). Orlandini et al. (2012) also carry out an analysis of *BeppoSAX* observations of the X-ray source at low luminosity of few $10^{34}\,{\rm erg\,s^{-1}}$ and find a CRSF at $44 \pm 3\,$keV.

Dönmez et al. (2020) carry out a timing and spectral analysis of the 2010 outburst of MAXI J1409−619 and connect variations in pulsed fraction and spectral index with a transition from high luminosity to low luminosity state. Their pulse-phase resolved spectral analysis further shows spectral hardening during phases with high emission, which they interpret as a tendency for harder X-ray emission from the magnetic poles. Raman et al. (2023) also analyze MAXI J1409−619 during its low luminosity state as observed by *NuSTAR* and conclude that the emission in this state is powered by accretion; they present the cold disk model as a possible

[1]Orthogonal rotators are X-ray pulsars whose magnetic axis and rotation axis are orthogonally aligned.

mechanism. The X-ray spectrum is well described by a powerlaw with $\Gamma = 1.54 \pm 0.25$ and a blackbody component with $kT_{\mathrm{BB}} = 1.75^{+0.8}_{-0.3}$ keV (Raman et al., 2023).

Ghimiray et al. (2024) analyze the same *NuSTAR* observation of MAXI J1409−619 and find a spectral description utilizing the `cutoffpl` model. They further find an increase in pulsed fraction with energy, which is generally expected for HMXBs (see, e.g., Ferrigno et al., 2023).

4.1.8 SRGA J124404.1-632232

SRGA J124404.1-632232 was discovered by the SRG/ART-XC and eROSITA (Predehl et al., 2021) in 2021(Semena et al., 2021). Already in the first publication on its detection, Semena et al. (2021) suggest the NIR/optical star 2MASS J12440380-6322320 as the optical counterpart, whose photogeometric distance is 5.8 ± 0.8 kpc (Gaia Collaboration, 2016, 2023; Bailer-Jones et al., 2021). This identification supports their tentative claim that the discovered source is an HMXB system, which is also supported by the semi-regular variability with period of 138 ± 1 d of the optical counterpart (Mroz & Udalski, 2021), which is interpreted as the orbital period of the system. The analysis of observations of the companion with the South African Large Telescope (*SALT*) lead Buckley et al. (2021) to the conclusion that the system is a obscured Be X-ray binary system. Follow-up observations with *NuSTAR* and *SALT* confirm the classification and reveal a spin period of ~538 s (Doroshenko et al., 2022). The X-ray spectrum is well described by an absorbed powerlaw in combination with two `comptt` Comptonization models.

4.1.9 X Persei

X Persei is a persistent Be X-ray binary, that was discovered with the *Copernicus* and *Ariel 5* satellites (White et al., 1976). Using a distance of 350 pc (which is approximately half of the current estimates of its photogeometric distance of 600 ± 14 pc, Gaia Collaboration, 2016, 2023; Bailer-Jones et al., 2021) a luminosity of few $10^{33}\,\mathrm{erg\,s^{-1}}$ was inferred. White et al. (1976) further report modulations of the X-ray flux with a 13.9 min (corresponding to 834 s) period. More than two decades later, Coburn et al. (2001) interpret a dip in the spectrum at 29 keV as a cyclotron line; with today's knowledge about spectral formation at low luminosities (see, e.g., Sokolova-Lapa, 2023), that predicts a dip between the thermal and nonthermal component, this identification as a CRSF seems at the very least questionable. The claim of a CRSF at ~30 keV is further challenged by Doroshenko et al. (2012), who successfully model X Persei's X-ray spectrum with two Comptonizing plasma components without the need for a cyclotron resonant scattering feature, and by Yatabe et al. (2018), who apply the torque model by Ghosh & Lamb (1979) and determine a lower limit for the magnetic field strength of 4×10^{13} G, which corresponds to a CRSF energy of ~400 keV.

Lutovinov et al. (2012) analyze a 15 year observational campaign of X Persei conducted with *RXTE* and *Swift*, during which several outbursts occurred where the X-ray luminosity increased by a factor up to 5. They also report on an extensive spin-down episode, which changed in favour of a significant spin-up during the campaign. Lutovinov et al. (2012) find the same dip as Coburn et al. (2001) previously and also interpret it as a CRSF. Another temporal analysis of X Persei by Nakajima et al. (2019) revealed a 7 year periodicity of X-ray flares, which they note is approximately a factor 10 longer than the orbital period of 250 d. More recently, Mushtukov et al. (2023) conducted a X-ray polarimetry analysis of X Persei using *IXPE*, and report a strong dependency of polarized emission on the pulse phase as well as a large angle between magnetic and rotational axis; which they emphasize is a similarity to GRO J1008−57. In their analysis of GX 304−1, Tsygankov et al. (2019c) use X Persei for spectral comparison and describe the latter as a persistent low luminosity X-ray binary, whose spectrum fundamentally differs from other, brighter XRBs. A recent broadband analysis of X Persei using *INTEGRAL* and *NuSTAR* observations by Rodi et al. (2024) also shows the double-hump shape of the X-ray spectrum, which they model as two cutoff powerlaws.

The *NuSTAR* observations analyzed in this work are given further below in Table 4.4.

4.2 Spectral transition of GRO J1008−57

GRO J1008−57 has been observed with *NuSTAR* five times at various luminosities. These observations therefore provide the opportunity to study the source's transition from its bright state at luminosities of $\sim 10^{37}\,\mathrm{erg\,s^{-1}}$ to its quiescent state at $\sim 10^{34}\,\mathrm{erg\,s^{-1}}$.

In this section, I investigate all available *NuSTAR* observations of GRO J1008−57 with the goal to show that the spectrum changes fundamentally towards low luminosities. All observations were extracted and reduced as described in Sect. 3.2. The spectrum was rebinned using the optimal rebinning routine by Kaastra & Bleeker (2016) with an additional requirement that each bin must at least contain 20 counts. The spectral model utilised for the description of the data is

$$I(E) = \mathtt{detconst} \times \mathtt{tbnew\_simple} \times (\mathtt{powerlaw} \times \mathtt{fdcut} + \mathtt{egauss}_1 + \mathtt{egauss}_2 \times \mathtt{bbody}), \tag{4.1}$$

where `detconst` is a detector constant, which is fixed to 1 for FPMA and free to vary between 0.9–1.1 for FPMB, `tbnew_simple` is the absorption model by Wilms et al. (2000), $\mathtt{egauss}_{1/2}$ are Gaussian emission lines to account for the Fe $K\alpha$ and Fe $K\beta$ lines and `bbody` is a blackbody component. The model also includes a gainshift constant, which accounts for possible miscalibrations of the detector energy grids, which are expected to be at most few tens of eV (see, e.g., Madsen et al., 2015). For all five observations, the fitted models and the residuals are shown in Fig. 4.1. The corresponding parameters are given in Table 4.1.

The residuals of the 2012 and 2015 observations show an excess below 5 keV, which hints at the presence of a complex iron line and soft excess, which are expected at high luminosities. The residuals of the 2014, 2018, and 2020 observation indicate no significant deviation from the data; for the 2020 observation however the model itself deviates significantly from the data at high energies. This is a result of the χ^2-statistic weighting data bins with the inverse square of the uncertainty, therefore nearly disregarding data bins with large uncertainties, in this case those at high energies. Only longer observations can solve this problem by constraining the high-energy emission to a higher degree.

I now turn to a brief discussion of the fit parameters and their variability at various luminosities to assess spectral changes. The absorption column density appears to decrease with luminosity, which could also be a result of lack of data below 3 keV, which is required to constrain the absorption reliably.

The photon index also shows an anti-correlation with luminosity and decreases from 2.39 from the lowest luminosity observation to 1.41 for the observation at highest luminosity. The cutoff energy varies erratically between 10^{-2}–10^{2} keV, indicating that a simpler cutoff model (e.g. `cutoffpl`) would have sufficed [2]. The folding energy varies between 10–21 keV for the higher luminosity observation, for the low luminosity observation it becomes apparent that the high-energy cutoff is not needed at all ($E_\mathrm{fold} = 100$ keV), which is consistent with the fact that the spectrum does not show a high-energy cutoff. Fe $K\alpha$ and Fe $K\beta$ emission lines are detectable in all but the lowest luminosity observation. As expected, the width of the Fe $K\alpha$ line cannot be constrained reliably, as it is expected to be below the detector resolution. The width of the Fe $K\beta$ line is significantly overestimated with values up to 2 keV. Although broad iron lines have been found for other sources such as Her X-1 (see Wolff et al., 2016), the value obtained here

[2]For example, a cutoff energy of 80 keV implies that the cutoff affects data points above 80 keV of which there are none for *NuSTAR* spectra.

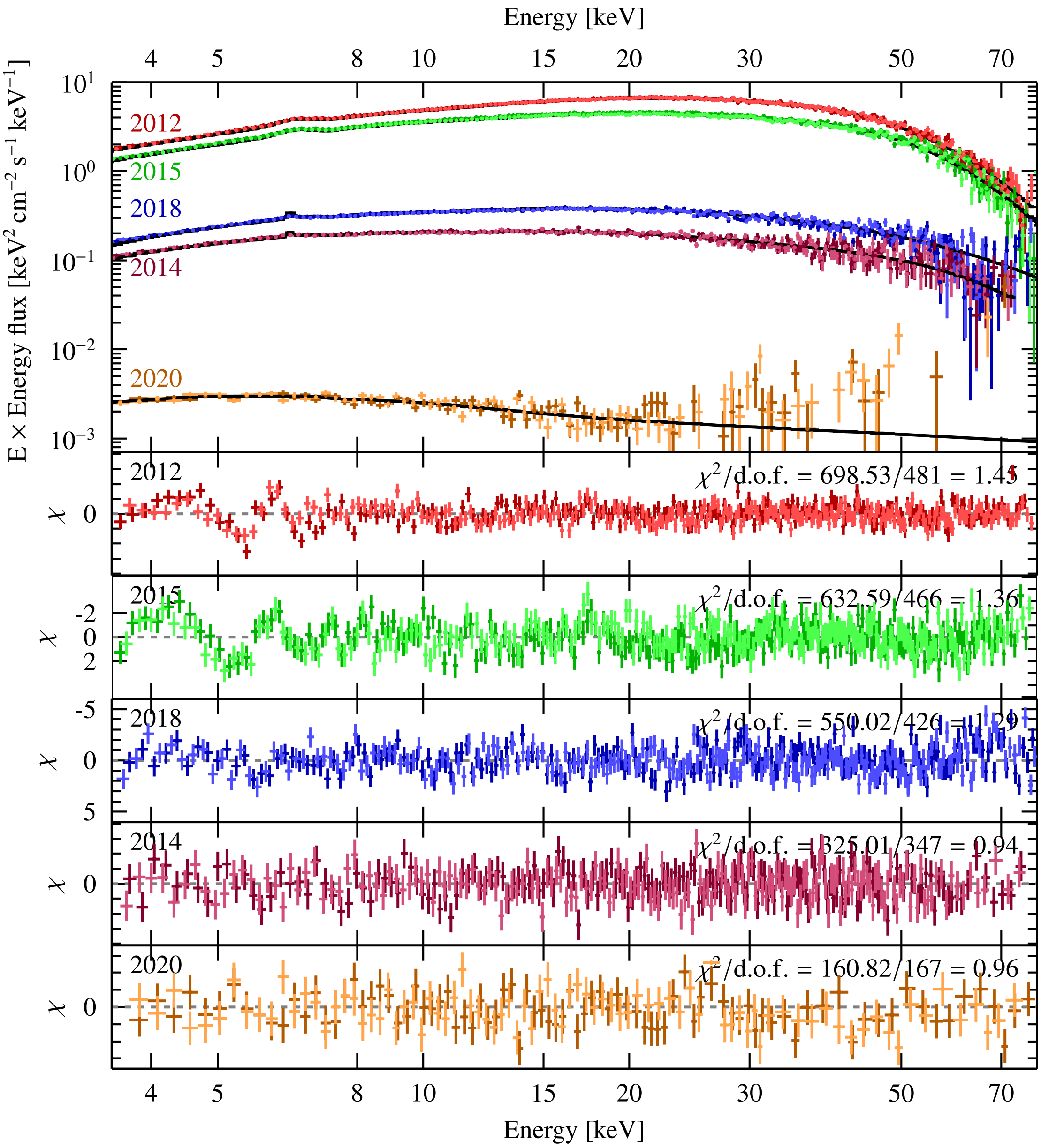

Figure 4.1: GRO J1008−57 spectra at various luminosities. The residuals are sorted by decreasing luminosity.

for the Fe $K\beta$ line is interpreted as a modeling effect and not of physical origin. Freezing the width to an arbitrarily small value of 0.3 keV and refitting resulted in wavy residuals around the Fe $K\beta$ line energy, which could hint at more complex emission patterns at soft energies, or that the emission line is not centered at 7.058 keV as assumed by the model or that issues regarding the gain shift component are present. Also, emission from ionized iron could be a contributing factor. As the emission lines are not the intended focus of this subsection, which is the broadband spectrum, I acknowledge the issues regarding the Fe $K\beta$ line, but will not further focus on them. The blackbody component is detected throughout all observations and generally increases in intensity with luminosity. For the low luminosity observation of 2020, its temperature is 1.7 keV; for the other observations it is ~4 keV, which is a significant change.

To further show the drastic changes in spectral shape, I show the powerlaw photon index Γ and the blackbody temperature kT_{BB} as a function of luminosity in Fig. 4.2.

Table 4.1: Parameters of fits to five *NuSTAR* observations of GRO J1008−57. The observations are listed column-wise by year of observation.

Parameter	2012	2015	2018	2014	2020
C_{FPMB}	0.9914 ± 0.0015	0.9794 ± 0.0017	1.004 ± 0.004	0.990 ± 0.006	1.01 ± 0.05
N_{H} [10^{22} cm^{-2}]	$3.20^{+0.27}_{-0.28}$	$3.83^{+0.30}_{-0.31}$	$7.0^{+1.0}_{-0.5}$	$8.2^{+1.1}_{-1.8}$	5^{+7}_{-6}
N_{PL}	0.97 ± 0.06	0.91 ± 0.05	$0.255^{+0.022}_{-0.071}$	$0.179^{+37.254}_{-0.025}$	$\left(5.1^{+3.7}_{-2.7}\right) \times 10^{-3}$
Γ	1.41 ± 0.04	1.54 ± 0.04	$1.47^{+0.39}_{-0.05}$	$2.00^{+0.13}_{-0.39}$	$2.39^{+0.20}_{-0.26}$
E_{cutoff} [keV]	$41.8^{+1.8}_{-2.0}$	$45.6^{+1.8}_{-2.1}$	$0.0117^{+48.6701}_{-0.0017}$	53^{+10}_{-54}	82^{+19}_{-35}
E_{fold} [keV]	10.5 ± 0.4	10.3 ± 0.6	$21.4^{+1.7}_{-6.4}$	15^{+13}_{-7}	$\leq 1.00 \times 10^{2}$
$A_{\mathrm{Fe\,K}\alpha}$ $\left[\mathrm{ph\,s^{-1}\,cm^{-2}}\right]$	$\left(8.0^{+0.7}_{-0.6}\right) \times 10^{-3}$	$(5.9 \pm 0.5) \times 10^{-3}$	$\left(2.4^{+0.5}_{-0.4}\right) \times 10^{-4}$	$(10 \pm 4) \times 10^{-5}$	–
$\sigma_{\mathrm{Fe\,K}\alpha}$ [keV]	$0.329^{+0.032}_{-0.030}$	$0.314^{+0.030}_{-0.029}$	$0.05^{+0.09}_{-0.05}$	$\left(7^{+2377}_{-7}\right) \times 10^{-4}$	–
$A_{\mathrm{Fe\,K}\beta}$ $\left[\mathrm{ph\,s^{-1}\,cm^{-2}}\right]$	$0.0265^{+0.0030}_{-0.0028}$	0.0284 ± 0.0030	$\left(1.7^{+1.1}_{-0.4}\right) \times 10^{-3}$	$\left(1.8^{+0.6}_{-0.9}\right) \times 10^{-3}$	–
$\sigma_{\mathrm{Fe\,K}\beta}$ [keV]	1.80 ± 0.10	2.05 ± 0.10	$1.69^{+0.18}_{-0.20}$	$1.90^{+0.22}_{-0.28}$	–
N_{BB}	0.046 ± 0.005	$0.0339^{+0.0029}_{-0.0030}$	$\left(7.0^{+4.0}_{-2.9}\right) \times 10^{-4}$	$\left(1.3^{+0.5}_{-1.0}\right) \times 10^{-3}$	$\left(1.8^{+1.6}_{-1.1}\right) \times 10^{-5}$
$\mathrm{k}T_{\mathrm{BB}}$ [keV]	$4.23^{+0.12}_{-0.13}$	$4.05^{+0.12}_{-0.13}$	$3.6^{+0.4}_{-0.7}$	$3.80^{+0.17}_{-0.69}$	$1.7^{+0.5}_{-0.4}$
G_{FPMA} [eV]	28 ± 12	60 ± 13	-36^{+21}_{-23}	$(-0 \pm 5) \times 10^{1}$	$(0 \pm 6) \times 10^{2}$
G_{FPMB} [eV]	51 ± 12	20 ± 13	-56^{+20}_{-22}	$(-1 \pm 5) \times 10^{1}$	$(1 \pm 6) \times 10^{2}$
$\mathcal{L}_{3.5\text{–}79\,\mathrm{keV}}$ [erg s^{-1}]	3.1×10^{37}	2.2×10^{37}	2.1×10^{36}	1.2×10^{36}	1.4×10^{34}
χ^2/d.o.f.	699/481	633/466	550/426	325/347	161/167
χ^2_{red}	1.45	1.36	1.29	0.94	0.96

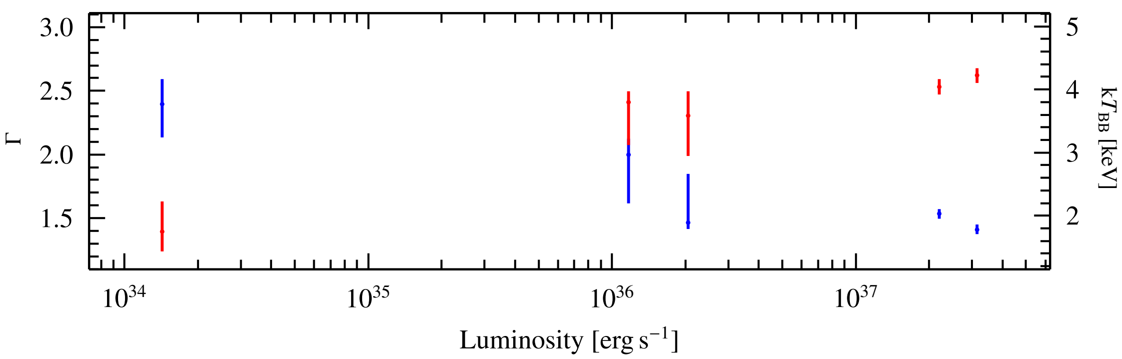

Figure 4.2: Selection of luminosity-dependent parameters in GRO J1008−57's X-ray spectrum. The photon index Γ is shown in blue, the blackbody temperature kT_{BB} is shown in red.

In summary, both broadband spectral components powerlaw continuum and blackbody emission change significantly at low luminosities. I would like to emphasize the following key points:

1. At low luminosities of $\sim 10^{34}\,\mathrm{erg\,s^{-1}}$ the spectral model does no longer require a cutoff component, a model with a pure powerlaw instead of a `powerlaw` × `fdcut` yields very similar results in terms of statistics and even shows an improvement in χ^2_{red} due to the increase in degrees of freedom.

2. The powerlaw shape also changes, the photon index increases towards lower luminosities to a value of $2.39^{+0.20}_{-0.26}$, softening its contribution.

3. The blackbody temperature also shows a drastic change in the low luminosity state; at higher luminosities it remains nearly constant at $\sim 4\,\mathrm{keV}$ whereas for the low luminosity observation a value of $1.7^{+0.5}_{-0.4}\,\mathrm{keV}$ is found.

All these arguments strongly suggest that the emission characteristics at low luminosities of $\sim 10^{34}\,\mathrm{erg\,s^{-1}}$ are fundamentally different. For GRO J1008−57, the observation carried out in 2020 therefore needs to be treated and modeled carefully, which is the aim of the following sections.

4.3 Pulse profiles at low luminosities

Before discussing low luminosity spectra in detail, the question remains whether the emission at low luminosities shows pulsations, which is a strong indicator for spectral formation in accretion columns or accretion mounds at the magnetic poles. In Sect. 4.3.1, I briefly revisit the previously shown *NuSTAR* observations of GRO J1008−57 and search for pulsations before taking a broader look at multiple sources and their low luminosity pulse profiles in Sect. 4.3.2.

4.3.1 Pulse profiles of GRO J1008−57 at various luminosities

In order to obtain pulse profiles for the five *NuSTAR* observations of GRO J1008−57, the routine described in Sect.2.8 is employed, where I search for pulsations with periods of ~93 s as indicated by the literature (see, e.g., Coe et al., 2007; Kühnel et al., 2013; Tsygankov et al., 2019a), which are found in all present observations with variations on the 0.1 s scale, owing to the long timespan of 8 years over which the observations were carried out, during which minor spin-up and spin-down events are expected (see, e.g., Ghosh & Lamb, 1979).

The pulse profiles obtained from the five *NuSTAR* observations are shown in Fig. 4.3. Furthermore, the pulsed fraction as a function of luminosity is shown in Fig. 4.4.

The pulse profiles of GRO J1008−57 at high and intermediate luminosities of 10^{36}–$10^{37}\,\mathrm{erg\,s^{-1}}$ show a double-peaked pulse profile with a broad main peak at a pulse phase of $\phi \approx 0.0$–0.3 and a secondary peak at $\phi \approx 0.6$–0.8, which is split into two peaks. Given that the secondary peak has a maximum normalized count rate of $\lesssim 1.0$, one can argue that it is not apparent due to excessive emission, but rather due to two deep troughs preceding and following it. With decreasing luminosity, the second trough at $\phi \approx 0.9$ becomes more narrow and shallow, whereas the first trough remains nearly unchanged. The splitting of the secondary peak vanishes and changes from a "plateau with negative slope" to one with a positive slope. Furthermore, the pulsed fraction remains nearly constant within uncertainties at a value of ~0.6, where a slight decrease at high luminosities is evident. For low luminosities however, the pulsed fraction decreases to a value of 0.178 ± 0.005. This is accompanied by a drastic change in the observed pulse profile, which features a broad main peak positioned at $\phi = 0.0$–0.4 and a shallow broad trough at $\phi = 0.5$–1.0.

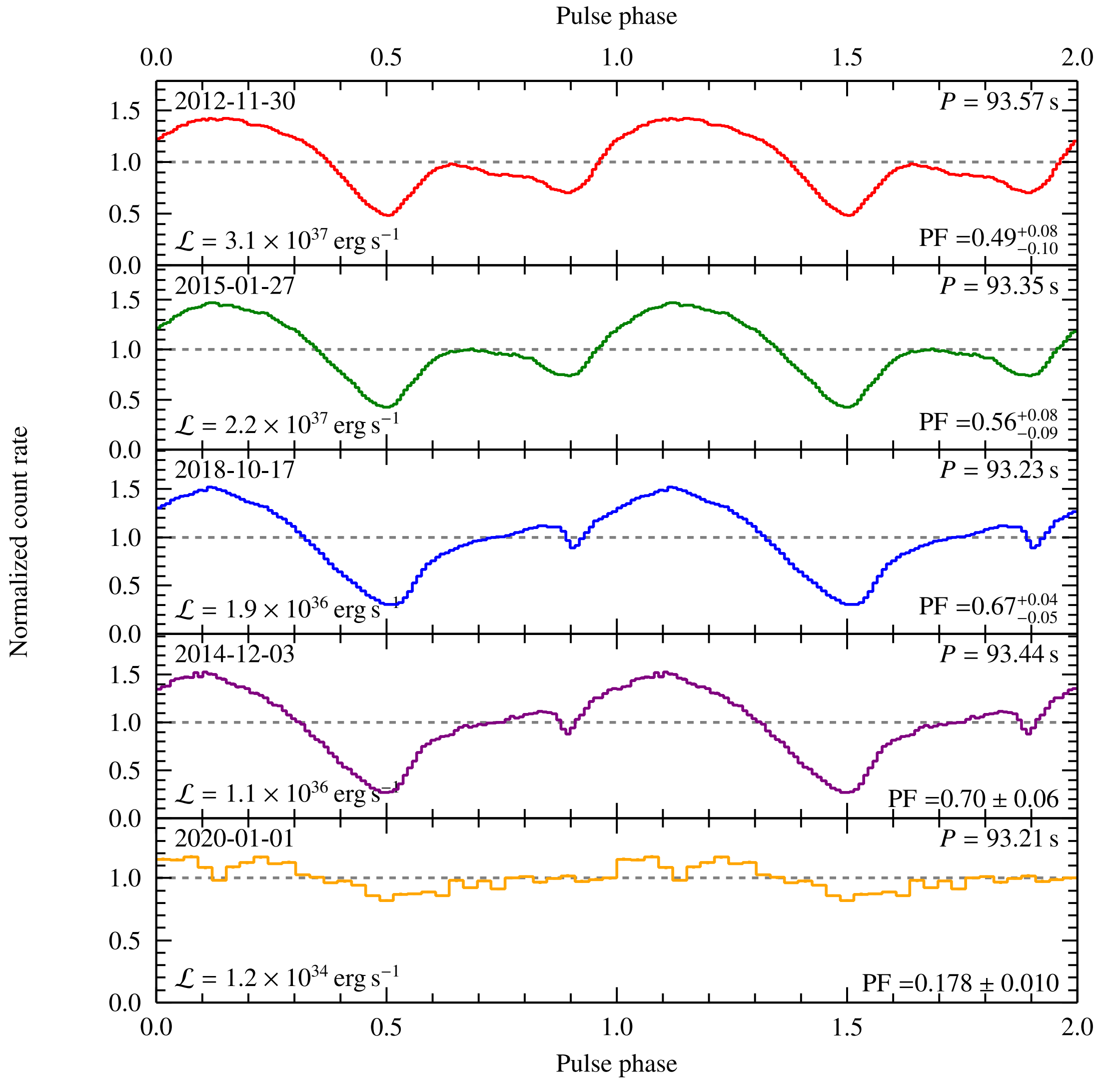

Figure 4.3: *NuSTAR* pulse profile of GRO J1008−57 at various luminosities. The pulse profiles of the two *NuSTAR* FPMs are added to further eliminate stochastic variability. The profiles are aligned such that their absolute minima are at $\phi = 0.5$. The observations are ordered in order of decreasing luminosity. In the top left corner the date of the observation is given, in the top right corner the pulse period is given and the pulsed fraction as defined in Eq. 2.23. Uncertainties are shown but not visible.

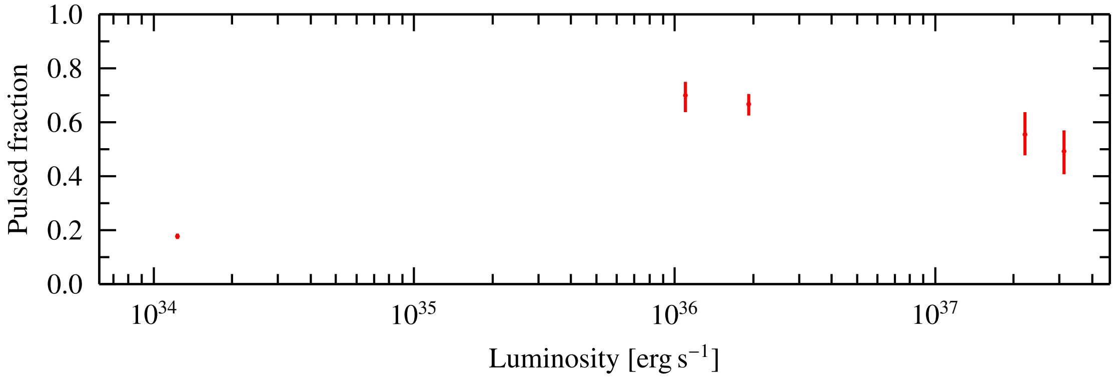

Figure 4.4: Pulsed fraction of GRO J1008−57 as a function of luminosity.

I emphasize that this however does *not* imply the cessation of pulsations; instead the pulse profile and pulsed fraction indicate weaker, but nevertheless undoubtedly present pulsations, which indicate that a significant part of the high-energy emission originates from the magnetic poles of the neutron star.

In summary, the here conducted brief analysis of the pulse profiles indicates that at luminosities of $\sim 10^{34}\,\mathrm{erg\,s^{-1}}$ GRO J1008−57 emits pulsed radiation resulting from anisotropic emission from the accretion columns which are seen under varying angles during the pulse phase.

4.3.2 Pulse profiles of various sources at low luminosities

While in the previous section I focused on the pulsed emission of a single source under the transition to the low luminosity state, here I aim to show that the observed behaviour of persisting pulsed emission is generally also found for other sources. For all BeXRBs introduced in Sect. 4.1 pulse profiles and *NuSTAR* spectra are shown in Fig. 4.5.

The pulse profile of 2RXP J130159.6-635806 shows a broad peak at pulse phase $\phi \sim 0.2$ and a strong, narrow dip at pulse phase 1.0. Both features imply a high pulsed fraction, which is on the order of 75%. The luminosity of few $10^{35}\,\mathrm{erg\,s^{-1}}$ is 1–2 magnitudes too high to use this observation for the analysis of HMXBs in quiescence, this particular observation, which is unfortunately the only available *NuSTAR* observation of the source, is therefore not considered for the investigation of low luminosity observations below.

At luminosities of $10^{34}\,\mathrm{erg\,s^{-1}}$, the pulse profile of A0535+26 shows little variability with a broad peak at $\phi \sim 0.2$–0.5 and a dip at $\phi \sim 1.0$. The pulsed fraction is in the order of 25% and not consistent with zero.

The pulse profile of Cepheus X-4 is single-peaked with a peak at $\phi \sim 0.3$ and a trough at $\phi \sim 1.0$. The observation at hand was performed at a luminosity few $10^{34}\,\mathrm{erg\,s^{-1}}$, which in combination with a comparably short exposure time of ~30 ks results in comparably low statistics, which is evident in strong statistical variations in the pulse profile, which potentially increase the pulsed fraction, which is 63%.

The pulse profile of GRO J1008−57 in its low luminosity state has already been discussed in the previous section, but is also included in Fig. 4.5.

GX 304−1 was observed by *NuSTAR* for ~173 ks, which is the longest observation included in this work and provides an excellent ground for spectral and timing analysis due to the comparably well constraints on high-energy emission resulting from the long exposure time. Its pulse profile shows a very broad peak extending from $\phi \sim 0.2$–0.9. The pulsed fraction is on the order of 33%.

MAXI J0655−013 also shows a broad peak in its pulse profile between $\phi \sim 0.2$–0.8, which is followed by a sharp drop. The observation and subsequent pulse profile is significantly impacted by the low flux level, which may influence the determined pulsed fraction of ~85%.

A similar argument can be made for the pulse profile of MAXI J1409−619, which is also impacted its low signal-to-noise ratio owing to the exceptionally low luminosity of $\sim 6\times10^{33}\,\mathrm{erg\,s^{-1}}$. The pulse profile shows a single broad excess at $\phi \sim 0.5$.

The pulse profile of SRGA J124404.1-632232 shows a "triangular" peak spanning the whole pulse period; at its peak the emission increases by ~50% compared to the average flux level.

Lastly, Fig. 4.5 shows the pulse profile of X Persei, which shows a broad, asymmetric peak spanning nearly the whole pulse period. Due to its close proximity, the high-energy emission is well constrained despite the low luminosity of few $10^{34}\,\mathrm{erg\,s^{-1}}$.

From the examples shown and discussed above it is clear that pulsations are detectable for a variety of BeXRBs at low luminosity levels down to few $10^{33}\,\mathrm{erg\,s^{-1}}$, which are an indicator for emission from the magnetic poles of the NS as well as the occurrence of mass accretion during the state of "quiescence".

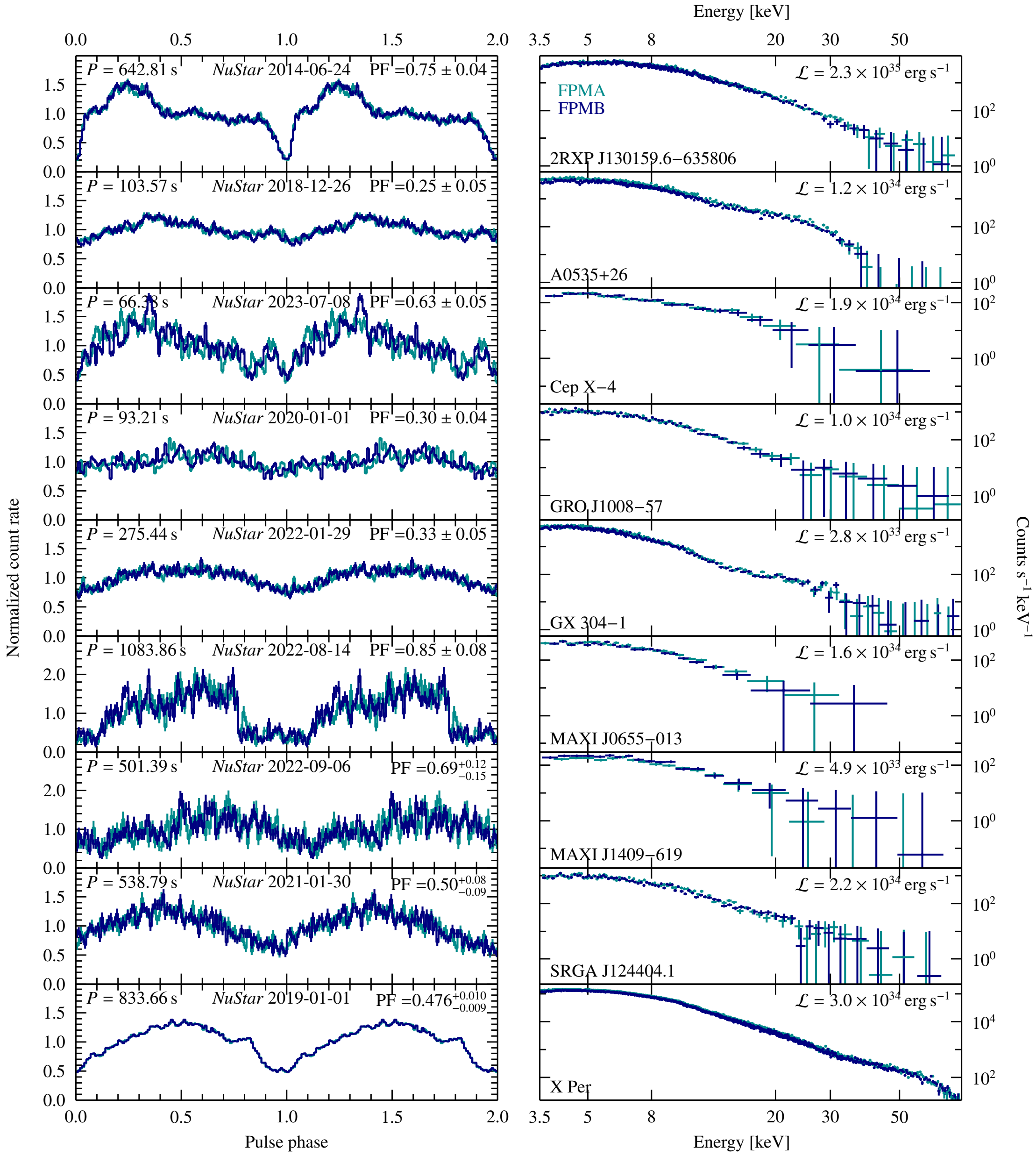

Figure 4.5: *NuSTAR* X-ray pulse profiles and spectra at low luminosities of various BeXRBs. The pulse period and pulsed fraction are shown in the left column, the observed luminosity in the 3.5–20 keV band is shown in the right column.

4.4 Constraining the cyclotron line of Cepheus X-4

Cepheus X-4 was observed twice by *NuSTAR* during the decline of its 2023 outburst. As the CRSF energy of ~30 keV is comparably low, it is expected that the CRSF can be detected even at low count rates. The two observations therefore provide the interesting opportunity to compare the influence of different fit statistics on the determined fit and especially CRSF parameters. In this section, I aim to obtain a simple empirical description of the first, brighter observation of Cepheus X-4 from the year 2023 utilizing the χ^2-, C- and W-statistic. Its goal is to answer whether more elaborate statistics are able to constrain the spectral parameters, specifically those modeling to cyclotron line, better than the predominantly used χ^2-statistic.

Table 4.2: Fit parameters of 2023 *NuSTAR* observation of Cepheus X-4. The parameters for the different statistics are shown column-wise.

Parameter	χ^2	C-Stat	W-Stat
C_{FPMB}	1.00 ± 0.04	1.01 ± 0.04	1.00 ± 0.04
C_{XRT}	0.41 ± 0.22	$0.46^{+0.18}_{-0.14}$	$0.41^{+0.22}_{-0.23}$
N_{H} [$10^{22}\,\mathrm{cm}^{-2}$]	10^{+5}_{-4}	$2.2^{+1.4}_{-1.0}$	9^{+6}_{-4}
N_{PL}	$0.010^{+0.015}_{-0.005}$	$\left(3.36^{+1.18}_{-0.29}\right) \times 10^{-3}$	$\left(9^{+8}_{-4}\right) \times 10^{-3}$
Γ	$2.6^{+0.6}_{-0.4}$	$2.08^{+0.21}_{-0.17}$	$2.6^{+0.7}_{-0.4}$
A_{Gaussian} [$\mathrm{ph\,cm^{-2}\,s^{-1}}$]	$\left(5.1^{+4.4}_{-1.9}\right) \times 10^{-4}$	$\left(3.3^{+1.6}_{-1.0}\right) \times 10^{-4}$	$\left(5.1^{+4.8}_{-2.0}\right) \times 10^{-4}$
E_{Gaussian} [keV]	14^{+5}_{-8}	$16.9^{+2.8}_{-2.7}$	13^{+4}_{-6}
$\sigma_{\mathrm{Gaussian}}$ [keV]	$11.2^{+3.5}_{-2.5}$	$9.5^{+2.4}_{-2.1}$	$11.3^{+3.6}_{-2.8}$
E_{CRSF} [keV]	$27.5^{+1.4}_{-1.2}$	27.5 ± 1.2	$27.5^{+1.5}_{-1.2}$
σ_{CRSF} [keV]	$2.7^{+1.3}_{-1.0}$	$2.9^{+1.3}_{-1.0}$	$2.6^{+1.4}_{-0.9}$
d_{CRSF} [keV]	$6.5^{+4.3}_{-2.9}$	7^{+5}_{-4}	$6.1^{+4.9}_{-2.6}$
Statistic/d.o.f.	150.51/177	179.70/177	163.47/177
Reduced Statistic	0.85	1.02	0.92

The broadband X-ray spectrum of Cepheus X-4 at low luminosities can be well described by a powerlaw *without* cutoff component. The CRSF itself is modeled with the earlier introduced `gabs` model component; an excess at ~15 keV, that can be interpreted as the red wing of the CRSF or more generally as part of the nonthermal hump, is modelled as a Gaussian in emission, represented by the `egauss` component. Together with the model components for interstellar absorption (`tbnew_simple`, Wilms et al., 2000) and a detector cross-calibration constant (`detconst`), the complete spectral model reads

$$I(E) = \mathtt{detconst} \times \mathtt{tbnew\_simple} \times (\mathtt{powerlaw} + \mathtt{egauss}) \times \mathtt{gabs}. \tag{4.2}$$

The fit parameters that were found for each fit statistic are given in Table 4.2. As expected, the two detector constants agree within uncertainties. The absorption column density found in the C-Stat fit is significantly lower than the values obtained with the other two statistics, but still above the Galactic absorption value along to line of sight of Cepheus X-4 of $\sim 0.8 \times 10^{22}\,\mathrm{cm}^{-2}$ as obtained with the HEASARC nH column density tool[3] (see Dickey & Lockman, 1990; Kalberla et al., 2005; HI4PI Collaboration et al., 2016, for further reference). For this particular observation, it is difficult to judge which determined absorption column density is more realistic as better soft coverage than the available short *Swift*/XRT observation would be required. The normalisations of the powerlaw and the Gaussian emission vary between the different statistics by as much as a factor of three. The photon indices the χ^2- and W-statistic fits are nearly identical, for the C-statistic a lower index, indicating a harder spectrum, is found. The obtained centroid energies of the Gaussian emission peak agree within uncertainty; the best constraints are found for the C-statistic fit. A similar picture arises for the width of the Gaussian feature, here however the C-statistic fit shows only slightly better constraints than the other two fits.

[3]See `https://heasarc.gsfc.nasa.gov/cgi-bin/Tools/w3nh/w3nh.pl`

Table 4.3: Relative uncertainties of CRSF parameters for the three utilized statistics.

Parameter	χ^2	C-Stat	W-Stat
E_{CRSF} [keV]	$27.53 \times (1.00 \pm 0.05)$	$27.49 \times (1.00 \pm 0.05)$	$27.49 \times (1.00^{+0.06}_{-0.05})$
σ_{CRSF} [keV]	$2.74 \times (1.0^{+0.5}_{-0.4})$	$2.90 \times (1.0^{+0.5}_{-0.4})$	$2.63 \times (1.0^{+0.6}_{-0.4})$
d_{CRSF} [keV]	$6.47 \times (1.0^{+0.7}_{-0.5})$	$6.74 \times (1.0^{+0.7}_{-0.5})$	$6.12 \times (1.0^{+0.8}_{-0.5})$

I now turn to the obtained cyclotron line parameters, which are given in Table 4.2 as well as again in Table 4.3 with relative uncertainties to facilitate the comparison of parameter constraints. The obtained centroid cyclotron line energy is identical for all three statistics with nearly identical constraints of ±5%, respectively. The width of the CRSF is consistent within uncertainties as well, but is generally only poorly constrained with relative uncertainties of ±50%. For the depth of the cyclotron line the situation is very similar, as the obtained parameter values agree within uncertainty and are generally only very poorly constrained with uncertainties exceeding 50%. The initial expectation that increasingly physically motivated statistics (basis on Poisson statistics for C-Stat, treatment of background radiation for W-Stat) lead to better constraints on spectrum parameters has not been confirmed by the here shown study. This does however not mean that these statistics pose no advantages, but merely that for the analysed dataset no improvement in parameter constraints could be found. Further improvements, especially for low luminosity observations, can be made by treating the background more carefully by modeling it (see, e.g., Wik et al., 2014). Simultaneous fitting of source and background models to the respective datasets may provide a way forward to constrain absorption features such as CRSFs even at low luminosities of 10^{33}–10^{34} erg s^{-1}. At low luminosities it is expected that the W-statistic generally yields better results due to its treatment of the background; here however I find that at least for the Cepheus X-4 observation above the use of the W-statistic does not result in significantly better constraints of the fit parameters. Therefore I will resort to the more simple χ^2-statistic for the analysis of low luminosity spectra in this work.

4.5 Constraining the high-energy emission at low luminosities

The main focus of this work is to find a (semi-)empirical description for the X-ray spectra of BeXRBs at low luminosities, which can constrain the high-energy emission well enough to utilize its description for further analyses, specifically estimating the magnetic field strength near the neutron star's surface. In this first part, I will test a variation of empirical models and discuss how well they can describe the X-ray spectra of the small list of sources given in Sect. 4.1. Prior to the spectral analysis, I conducted a preliminary feasibility analysis for the X-ray spectra of the listed sources, in which I aimed to exclude observations with too poor signal-to-noise ratios such as the second Cepheus X-4 observation of 2023 and too bright observations such as the one of 2RXP J130159.6-635806. Furthermore, the *Swift*/XRT data for X Persei suggests that the source was observed in a less luminous state in comparison with the 16 hour later conducted *NuSTAR* observation. The *Swift*/XRT data for X Persei is therefore not considered in the following spectral analyses. As the low source luminosities are expected to be most likely insufficient to constrain the absorption column density, the corresponding N_{H} value of the absorption model (`tbnew_simple`, see Wilms et al., 2000) is set to the Galactic absorption value

Table 4.4: List of observations utilized in the investigation of low luminosity spectra of BeXRBs.

Source	Distance [kpc] [(a)]	Date	Exp. [ks]	Joint with	$\mathcal{L}\left[\mathrm{erg\,s^{-1}}\right]$ [(b)]	$N_\mathrm{H}\left[10^{22}\,\mathrm{cm^{-2}}\right]$ [(c)]
A0535+26	$1.77^{+0.07}_{-0.06}$	2018-12-26	54.9	*XRT*	1.0×10^{34}	0.44
Cep X−4	$7.2^{+0.8}_{-0.7}$	2023-07-07	26.5	*XRT*	5.9×10^{34}	0.8
GRO J1008−57	$3.52^{+0.17}_{-0.16}$	2020-01-01	45.2	*XRT*	8.1×10^{33}	1.2
GX 304−1	$1.85^{+0.06}_{-0.05}$	2022-01-29	174.0	XMM	2.0×10^{33}	1.0
MAXI J0655−013	$3.44^{+0.26}_{-0.21}$	2022-08-14	11.3	*XRT*	1.1×10^{34}	0.55
MAXI J1409−619	$4.4^{+1.2}_{-0.6}$	2022-09-06	40.5	*XRT*	4.0×10^{33}	2.0
SRGA [(d)]	5.8 ± 0.8	2021-01-30	54.0	*NICER*	1.5×10^{34}	1.3
X Per	0.600 ± 0.014	2019-01-01	58.3	–	2.3×10^{34}	0.063

a) Photogeometric distance as estimated from *Gaia* data (Gaia Collaboration, 2016, 2023) by Bailer-Jones et al. (2021).
b) Absorbed X-ray luminosity in the 5–20 keV band in the observer's frame. The luminosity is calculated based on a high-energy cutoff powerlaw fit.
c) The Galactic absorption column density is obtained from the HEASARC nH Column Density Tool (See `https://heasarc.gsfc.nasa.gov/cgi-bin/Tools/w3nh/w3nh.pl`), which is based on Dickey & Lockman (1990), Kalberla et al. (2005) and HI4PI Collaboration et al. (2016).
d) Full name: SRGA J124404.1-632232

as determined by Dickey & Lockman (1990), Kalberla et al. (2005) and HI4PI Collaboration et al. (2016)[4]. The observations used for this analysis are listed in Table 4.4.

In this work I utilize three criteria to judge the goodness of a fit:

1. The fit residuals must show no systematic structure that indicate potential missing model components. Ideally, they should be evenly scattered around the zero.
2. The ratio between χ^2-statistic and the degrees of freedom, often known as the reduced statistic is expected to approach unity.
3. Most importantly, all model components should model the spectral feature they are intended to. If parameters cannot be constrained reasonably or they even take values that indicate that the component does not describe the intended feature, the model is not considered useful for this analysis.

The simplest spectral model tested here to describe double-hump spectra consists of a `comptt` component for the thermal hump and a Gaussian feature for the red part nonthermal hump, so that it reads in total

$$I(E) = \mathtt{detconst} \times \mathtt{tbnew\_simple} \times (\mathtt{comptt} + \mathtt{egauss}). \tag{4.3}$$

The fact that the Gaussian component is only supposed to model the red component of the nonthermal hump implies that the above given (and all subsequent) models do not account for

[4]This procedure may underestimate the absorption column densities in case the total absorption exceeds the Galactic absoption due to circumstellar absorption. Even if this is the case, its effect is expected to be negligible as the absorption column density cannot be determined sufficiently well due to the lack of high-quality data in the soft X-ray band for most sources with the exception of GX 304−1 and SRGA J124404.1-632232.

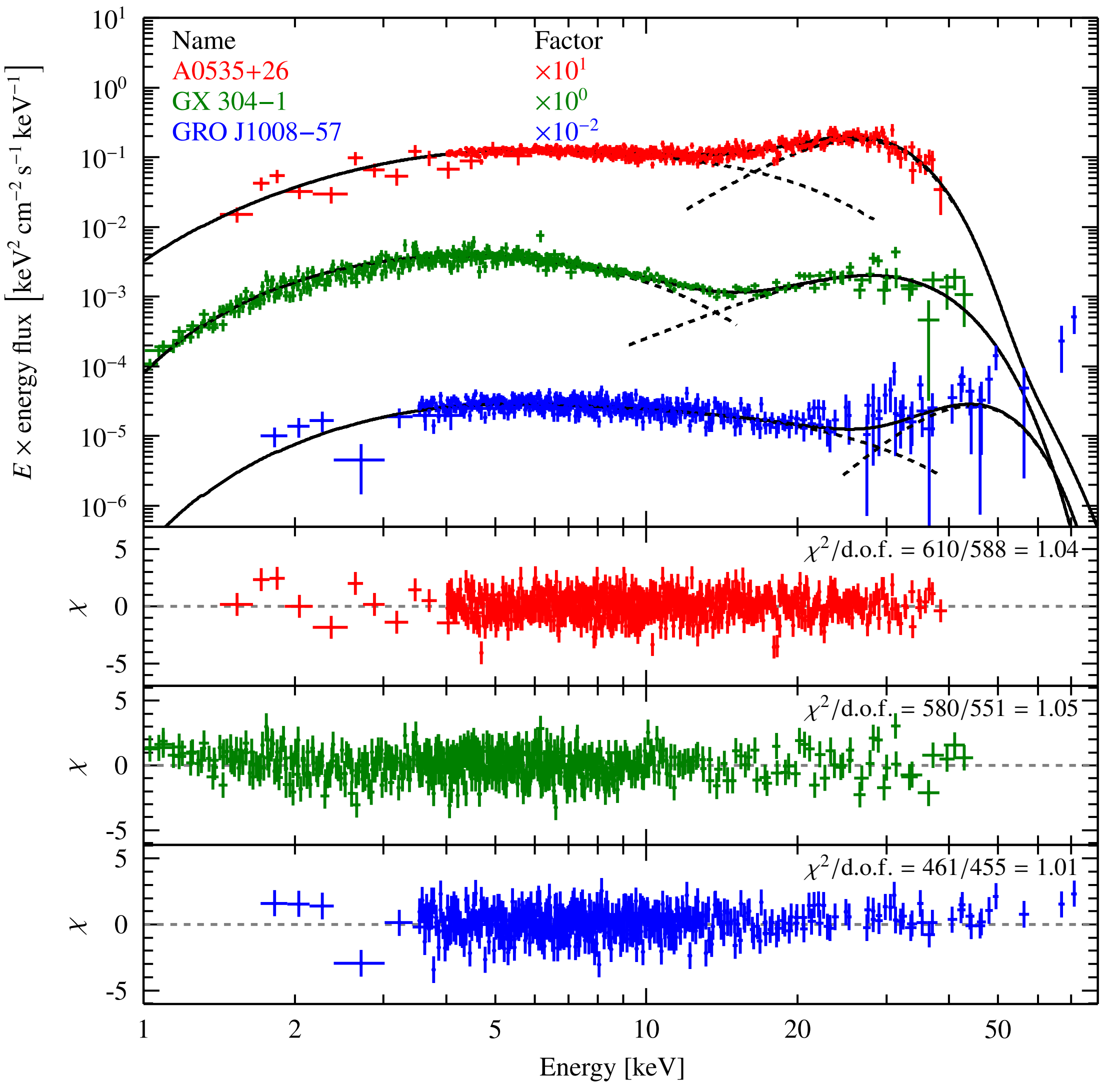

Figure 4.6: `comptt+egauss` fits to A0535+26,GRO J1008−57 and GX 304−1.The spectra have been shifted according to the factors given in the inset for plotting purposes. The solid line represents the full spectral model, the dashed lines its respective components. The bottom panels show the residuals for each spectrum.

absorption features due to cyclotron resonant scattering. Such features can therefore not be adequately modeled by it and I subsequently only fit the data at energies below the cyclotron line energy for sources with known CRSFs; this impacts Cepheus X-4, A0535+26 and GX 304−1, whose *NuSTAR* spectra are only modeled up to 25 keV, 40 keV and 50 keV, respectively.

The model is applied to all observations listed above with varying degree of success, as only the fits to the X-ray spectra of A0535+26, GRO J1008−57 and GX 304−1 fulfil all three criteria described above. The spectral fits along with residuals are shown in Fig. 4.6, the corresponding parameters are given in Table 4.5.

For all three sources, the seed photon temperature is below 1 keV and well constrained. The plasma temperatures determined for A0535+26 and GRO J1008−57 are both on the order of few keV, where it has to be noted that for the latter the upper confidence limit cannot be constrained within reason. For GX 304−1, the plasma temperature is considerably lower at 1.86 keV. The optical depths are also consistent within uncertainties and around 3–7τ_T, which is close to the

Table 4.5: Parameters of `comptt+egauss` spectral fits to A0535+26, GRO J1008−57 and GX 304−1 as shown in Fig. 4.6.

Parameter	A0535+26	GRO J1008−57	GX 304−1
C_{FPMB}	0.967 ± 0.014	1.02 ± 0.04	1.034 ± 0.017
C_{XRT}	0.85 ± 0.12	$0.88^{+0.21}_{-0.20}$	–
C_{EPN}	–	–	0.85 ± 0.04
C_{EMOS1}	–	–	$0.99^{+0.06}_{-0.05}$
C_{EMOS2}	–	–	0.91 ± 0.05
$N_{\mathtt{comptt}}$	$\left(1.8^{+1.1}_{-1.0}\right) \times 10^{-3}$	$\left(2.9^{+1.9}_{-2.0}\right) \times 10^{-4}$	$\left(1.48^{+0.16}_{-0.20}\right) \times 10^{-3}$
$k_{\mathrm{B}}T_0$ [keV]	$0.89^{+0.08}_{-0.16}$	$0.87^{+0.08}_{-0.10}$	0.70 ± 0.05
$k_{\mathrm{B}}T$ [keV]	$3.6^{+3.5}_{-1.2}$	$5.3^{+9.5}_{-1.9}$	$1.86^{+0.25}_{-0.16}$
τ	$4.7^{+2.2}_{-1.9}$	$3.4^{+1.5}_{-2.1}$	7.0 ± 1.1
A_{Gaussian} [ph cm^{-2} s^{-1}]	$(5.7 \pm 2.0) \times 10^{-4}$	$\left(3.8^{+9.0}_{-1.9}\right) \times 10^{-5}$	$\left(9.9^{+2.4}_{-2.1}\right) \times 10^{-5}$
E_{Gaussian} [keV]	$22.0^{+1.5}_{-2.1}$	40^{+6}_{-23}	$19.0^{+2.7}_{-2.1}$
$\sigma_{\mathrm{Gaussian}}$ [keV]	7.5 ± 1.2	10^{+23}_{-4}	$11.1^{+2.4}_{-2.2}$
$\mathcal{L}^{\mathrm{obs}}_{5\text{–}50\,\mathrm{keV}}$ $\left[10^{34}\,\mathrm{erg\,s^{-1}}\right]$	1.37	1.04	0.25
χ^2/d.o.f.	610/588	461/455	580/551
χ^2_{red}	1.04	1.01	1.05

high optical depths of 10–100τ_T expected deep down in the NS atmosphere, where this radiation is expected to form (see, e.g., Sokolova-Lapa et al., 2021, Fig. 4 therein). For A0535+26 and GX 304−1 the centroid energy of the Gaussian feature modeling the nonthermal hump up to the cyclotron line can be constrained well to energies slightly above 20 keV; for GRO J1008−57 a value of 40 keV is found, which is however only very poorly constrained. This upshift in centroid energy could be a result of the higher cyclotron line energy expected for GRO J1008−57, which is a factor of 1.5–2.0 higher than for the other two sources (~90 keV for GRO J1008−57 versus 45 keV for A0535+26 and 54 keV for GX 304−1). A similar picture arises for the width of the Gaussian feature, which is again well constrained for A0535+26 and GX 304−1 to values between 7–11 keV and only poorly constrained for GRO J1008−57.

In summary, although this model provides a good description of the data for the three mentioned sources, it fails for the other five sources and cannot constrain the parameters for GRO J1008−57 to a satisfactory degree. I therefore conclude that this model cannot constrain the high-energy emission sufficiently well to use it as a basis for further investigation and continue the search for a better empirical spectral model.

Tsygankov et al. (2019a) have shown that a model consisting of two `comptt` components provides a satisfactory description of the X-ray spectrum of A0535+26 in its low luminosity state in which it exhibits the above described double-hump shape. I therefore also test such a model defined as

$$I(E) = \mathtt{detconst} \times \mathtt{tbnew\_simple} \times (\mathtt{comptt1} + \mathtt{comptt2}) \tag{4.4}$$

and call it `2comptt` model for further reference. Evidently, one `comptt` component represents the thermal hump and the second one the nonthermal hump. Unlike Tsygankov et al. (2019a), I

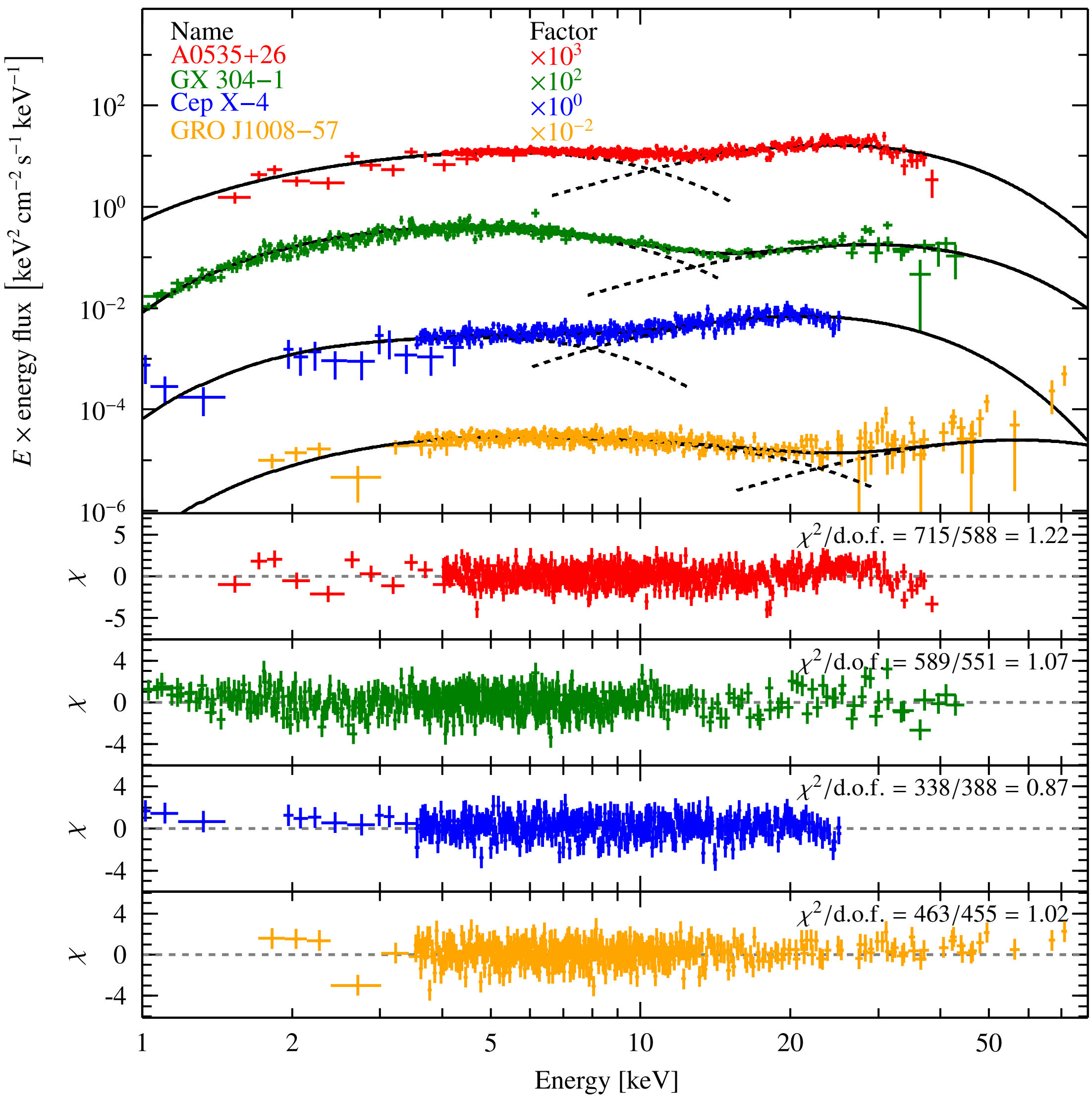

Figure 4.7: `2comptt` spectral fits to A0535+26, GRO J1008−57, GX 304−1 and Cepheus X-4. The top panel shows the spectra along with the spectral model as a solid line and the two single components as dashed lines. The spectra have been shifted according to the factors given in the inset for plotting purposes. The lower panels show the residuals of each spectral fit.

do not include CRSFs in this model and restrict the data to an energy range below it, so that in this case the second `comptt` component represents the part below the nonthermal hump below the CRSF feature. Like Tsygankov et al. (2019a), I tie the seed photon temperatures T_0 so that the spectral models are directly comparable among publications; in a physical picture the tying of the two temperatures implies that both components' seed photons have the same origin, which is not necessarily fulfilled in the NS atmosphere, where the temperature in the upper layers of the atmosphere is significantly higher than near the surface (see, e.g., Sokolova-Lapa et al., 2021). Once again, I apply the model to the eight observations listed in Table 4.4. This spectral model is able to provide a satisfactory description of the X-ray spectra of A0535+26, GX 304−1, Cepheus X-4 and GRO J1008−57. The spectral fits are shown in Fig. 4.7 and the corresponding parameters are given in Table 4.6.

All spectral fits provide a satisfactory description of the data, the statistics indicate that the fit to the X-ray spectrum of A0535+26 is slightly worse in comparison with the `comptt` + `egauss`

Table 4.6: Parameters of `2comptt` spectral fits to A0535+26, GRO J1008−57, GX 304−1 and Cepheus X-4 as shown in Fig. 4.7.

Parameter	A0535+26	GRO J1008−57	GX 304−1	Cep X−4
C_{FPMB}	0.967 ± 0.014	1.02 ± 0.04	1.034 ± 0.017	1.01 ± 0.04
C_{XRT}	$0.78^{+0.13}_{-0.12}$	$0.87^{+0.21}_{-0.20}$	–	0.35 ± 0.21
C_{EPN}	–	–	0.85 ± 0.04	–
C_{EMOS1}	–	–	$0.99^{+0.06}_{-0.05}$	–
C_{EMOS2}	–	–	0.91 ± 0.05	–
Model normalisation	$\left(4.2^{+0.6}_{-0.4}\right) \times 10^{-3}$	$(4.3 \pm 1.5) \times 10^{-4}$	$\left(1.66^{+0.11}_{-0.12}\right) \times 10^{-3}$	$0.0165^{+0.0011}_{-0.0158}$
$k_{\mathrm{B}}T_0$ [keV]	0.53 ± 0.15	$0.84^{+0.09}_{-0.11}$	$0.66^{+0.04}_{-0.05}$	1.27 ± 0.16
$k_{\mathrm{B}}T_{\mathtt{comptt1}}$ [keV]	$1.65^{+0.09}_{-0.08}$	$3.8^{+1.7}_{-1.2}$	$1.68^{+0.11}_{-0.09}$	$0.41^{+0.42}_{-0.13}$
$\tau_{\mathtt{comptt1}}$	$12.0^{+2.0}_{-1.6}$	$4.4^{+1.3}_{-1.2}$	$8.1^{+1.0}_{-0.9}$	23^{+43}_{-24}
`comptt2` rel. normalisation	$0.045^{+0.007}_{-0.006}$	$0.013^{+0.178}_{-0.004}$	$\left(9.0^{+77.7}_{-0.6}\right) \times 10^{-3}$	$\left(6^{+289}_{-6}\right) \times 10^{-3}$
$k_{\mathrm{B}}T_{\mathtt{comptt2}}$ [keV]	$6.12^{+0.16}_{-0.15}$	14^{+486}_{-5}	$7.2^{+0.6}_{-0.5}$	$5.29^{+0.78}_{-0.28}$
$\tau_{\mathtt{comptt2}}$	$\left(1.00^{+0.00}_{-0.74}\right) \times 10^{2}$	75^{+25}_{-75}	$\left(1.00^{+0.00}_{-0.89}\right) \times 10^{2}$	$\left(1.00^{+0.00}_{-0.91}\right) \times 10^{2}$
$\mathcal{L}^{\mathrm{obs}}_{5\text{–}50\,\mathrm{keV}}$ $\left[10^{34}\,\mathrm{erg\,s^{-1}}\right]$	1.32	1.00	0.26	3.52
χ^2/d.o.f.	715/588	463/455	589/551	338/388
χ^2_{red}	1.22	1.02	1.07	0.87

fit with $\chi^2_{\mathrm{red}} = 1.22$, the residuals do however show only minor deviations from the model at energies approaching the CRSF energy, which is expected. The seed photon and plasma temperatures are all below 1.5 keV and generally well constrained. The optical depths determined for A0535+26, GRO J1008−57 and GX 304−1 for the thermal component are all within the same magnitude as in the `comptt+egauss` model, for Cepheus X-4 the optical depth is $21\tau_{\mathrm{T}}$ and only poorly constrained. The optical depth of the `comptt` component modeling the nonthermal hump τ_{comptt2} is expected to be low, as the nonthermal hump is expected to form throughout the NS atmosphere, where the optical depth decreases down to values of $10^{-2}\tau_{\mathrm{T}}$. The obtained parameter is however much too high with values up to $10^{2}\tau_{\mathrm{T}}$ for all fours sources. This is already a strong indicator that while the `2comptt` model may provide a good description of the data in terms of statistics, it does not provide a good description of the data in terms of the physical parameters and the physical process it is intended to describe. A second indicator is the comparably low plasma temperature of the nonthermal component of a few keV (apart from GRO J1008−57, for which a value of 14 keV is found, whose upper limit is however not constrained), which theory predicts to be on the order of tens of keV (see, e.g., Sokolova-Lapa et al., 2021, Fig. 4 therein). Also, the Comptonization model by Titarchuk (1994) does not describe *magnetic* Comptonization, but non-magnetic Comptonization, and can therefore only describe the spectrum from a phenomenological standpoint. In conclusion, modeling both the thermal and nonthermal components with the Comptonizing plasma model `comptt` results in a statistically satisfactory description of 4 out of 8 observations, but shows severe issues when interpreting the parameters from a physical point of view. In this work, the direct physical meaning of the fit parameters plays only a minor part, so that a empirical description of the data would also be sufficient to conduct a further investigation.

Following the stated issues with the `comptt` model, I therefore now turn again to a more empirical description of the data. In the next iteration, I model the thermal component using the `cutoffpl` model and the nonthermal component using a Wien hump as described in Sect. 2.7.3. One can express the spectral model as

$$I(E) = \texttt{detconst} \times \texttt{tbnew\_simple} \times (\texttt{cutoffpl} + \texttt{wienhump}). \tag{4.5}$$

Based on theoretical models such as `polcap`, I expect that the magnetic field strength influences the position of the nonthermal hump in relation to the thermal component(see, e.g., Fig. 2.9 herein, lower panel). In order to indirectly obtain the CRSF energy from the fit model I require access to the energy, at which the thermal and nonthermal component intersect, where their contributions to the model are equal. Analytically, this energy can be obtained by solving the equation

$$\begin{aligned} \texttt{cutoffpl}(E_\text{intersect}) &= \texttt{wienhump}(E_\text{intersect}) \\ K_1 \times E_\text{intersect}^{-\Gamma} \times \exp\left(-\frac{E_\text{intersect}}{E_\text{fold}}\right) &= K_2 \times E_\text{intersect}^2 \times \exp\left(-\frac{E_\text{intersect}}{k_\text{B}T_\text{Wien}}\right) \end{aligned} \tag{4.6}$$

for $E_\text{intersect}$, which is evidently no simple undertaking; the uncertainty estimation of $E_\text{intersect}$ is even more challenging.

In a preliminary analysis, I employ the following strategy to estimate the intersection energy and its uncertainty:

1. I obtain a good description of the data with the `cutoffpl+wienhump` model.

2. I explore the parameter space using Markov chain Monte Carlo algorithms (MCMC, see, e.g., Mackay, 2003; Goodman & Weare, 2010; Foreman-Mackey et al., 2013)

3. From the more than 10^6 obtained parameter sets, I select those for which for the fit statistic the condition $\chi^2 \leq 1.5 \times \min(\chi^2)$ is fulfilled. From those, I calculate the smallest possible 90% intervals for all fit parameters and use them as a filter criterion.

4. For the remaining parameter sets (which are still in excess of 10^4), I calculate the intersection energy of the two components numerically by evaluating `cutoffpl-wienhump` on a fine grid. It must be noted that this step could be improved by using root-finding algorithms.

5. Lastly, I histogram the obtained intersection energies and also calculate the smallest 90% interval, which is then interpreted as the uncertainty interval of the intersection energy. The intersection energy *value* is obtained from the intersection energy as found in the best-fit, on which this routine is based.

Apart from the caveats mentioned in each step, this method requires a significant amount of computation resources and takes ~1 d to run. Furthermore, each step increases the risks of errors and overlooked edge cases, which decrease the method's credibility and robustness.

I therefore employ a different strategy to obtain the intersection energy: it is also viable to implement a fit function which takes the intersection energy as an input parameter, which then replaces one of the other input parameters. Solving Eq. 4.6 for K_2, one obtains

$$K_2 = K_1 \times E_\text{intersect}^{-(\Gamma+2)} \times \exp\left[E_\text{intersect} \times \left(\frac{1}{k_\text{B}T_\text{Wien}} - \frac{1}{E_\text{fold}}\right)\right]. \tag{4.7}$$

I therefore define a fit-function (christened `doublehump`), that takes the `cutoffpl` norm K_1, photon index Γ and folding energy E_fold as well as Wien temperature $k_\text{B}T_\text{Wien}$ and the intersection energy $E_{\mathrm{intersect}}$ as input parameters. Internally, this function then computes the norm K_2 as in Eq. 4.7 and returns the sum of the `cutoffpl` and `wienhump` components. I emphasize that this reparametrisation restricts the spectral model to realisations which *do* intersect and excludes those parameter sets that do not intersect (or do so at negative energies). It is therefore not able to reproduce all models that could be obtained by a `cutoffpl + wienhump` model. I now turn to the application of the spectral model

$$I(E) = \mathtt{detconst} \times \mathtt{tbnew\_simple} \times \underbrace{\mathtt{doublehump}}_{\mathtt{cutoffpl+wienhump}} \tag{4.8}$$

to the X-ray spectra of BeXRBs in quiescence. This model is able to obtain a good description of the data for all eight observations listed in Table 4.4. The fitted spectra are shown in Fig. 4.8, their residuals are shown in Fig. 4.9 and their parameters are given in Table 4.7. As this spectral model is the first in this work that is able to provide a satisfactory description of all eight observations, I will briefly discuss the obtained results for each source individually in the following.

The residuals of the fit to the observation of GX 304−1 show no systematic deviation from the model and appear to be scattered stochastically around zero. The photon index and folding energy are both well constrained. The temperature of the Wien component is 6.6 keV, indicating that it peaks at ∼20 keV. The intersection energy is found to be 12.11 ± 0.25 keV, which is consistent with a visible dip at this energy.

For A0535+26, the residuals up to 35 keV also show no systematic deviations from the model, at energies up to the pre-defined limit of 40 keV the model overestimates the flux, which is a direct result of a cyclotron resonant scattering feature at 45 keV. The absorption line is most likely no narrow feature, but extends few keV both towards the red and blue. Also excluding the energy range of 35–40 keV leads to a significant improvement in statistic by $\Delta\chi^2 = 56$, yielding a reduced χ^2 of 1.15. The deviation close to 40 keV is therefore not a result of incorrect modeling, but an expected deviation due to the CRSF, which is intentionally not included in the model. The intersection energy and Wien temperature are both well constrained and show similar values as obtained for GX 304−1. The obtained luminosity for A0535+26 of $1.39 \times 10^{34}\,\mathrm{erg\,s^{-1}}$ is not in agreement with the value obtained by Tsygankov et al. (2019a). As explained in Appendix A, this discrepancy is the result of differing energy ranges, distances, and modeling approaches.

The residuals to the spectral fit to GRO J1008−57 also shows no systematic deviation from the model over the whole energy range from 1–79 keV, which is also reflected by the reduced fit statistic being close to unity. The Wien temperature and intersection energy are higher by a factor of roughly two compared to GX 304−1 and A0535+26 and generally less well constrained, with $E_{\mathrm{intersect}}$ only being constrained to an interval of 7 keV.

As noted by Tsygankov et al. (2019c), the X-ray spectrum of X Persei is unlike those of other X-ray pulsars, which are often described by cutoff powerlaws. X Persei is known to show a double-hump spectrum, which is also the case in the observation analysed in this work. The residuals of the `doublehump` fit show deviations at energies above 10 keV with two shallow troughs between 10–25 keV and 25–50 keV. Both are however shallow enough and the fit statistic well enough that the obtained description of the data is still acceptable. A preliminary analysis has shown that the fit statistic can be significant improved by increasing the absorption column density, which is however not justified due to the low Galactic absorption column along the line of sight due to X Persei's proximity. The increase in absorption could be interpreted as local absorption close to the system; this claim can however only be substantiated with well-constrained data in the soft X-ray band down to ∼1 keV, which is not available for the 2019 *NuSTAR* observation. As this source is exceptionally close with a distance of only ∼600 pc (Gaia Collaboration, 2016, 2023; Bailer-Jones et al., 2021), the flux level at low luminosities is

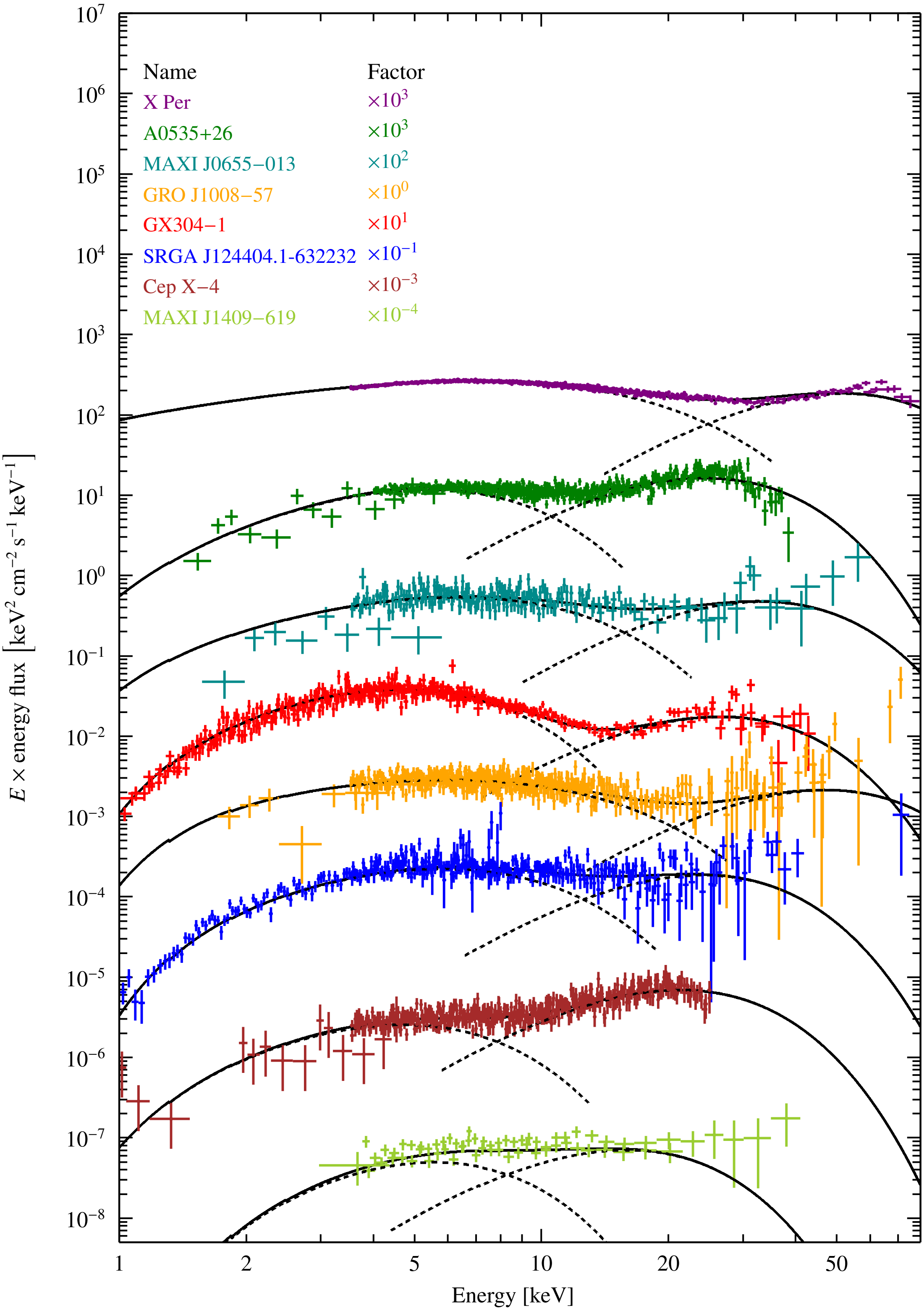

Figure 4.8: `doublehump` spectral fits to low-luminosity spectra of BeXRBs. The spectra have been shifted according to the factors given in the inset for plotting purposes. The solid line resembles the full spectral model; the dashed lines show its `cutoffpl` and `wienhump` components, respectively.

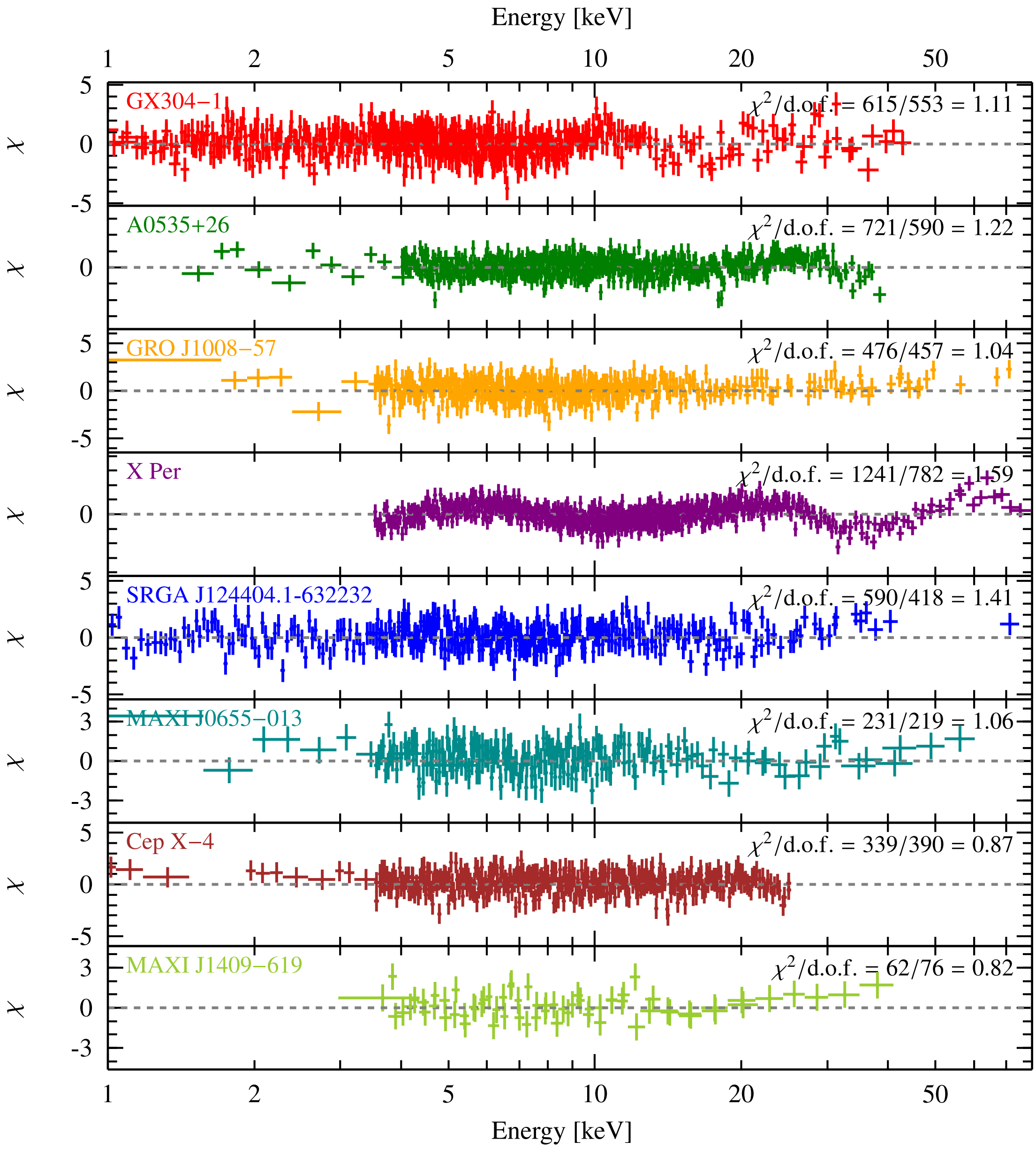

Figure 4.9: Residuals of `doublehump` fits as shown in Fig. 4.8.

expected to be high enough to constrain fit parameters comparably well. This is the case in this analysis, as all fit parameters are constrained within comparably small intervals and even the intersection energy can be constrained within an interval of ~0.8 keV. With a value of 24.8 keV, the intersection energy obtained for X Persei is the highest of the whole sample of observations.

For SRGA J124404.1-632232, the residuals indicate a satisfactory description of the data as they appear scattered stochastically around zero. The reduced fit statistic of 590/418 = 1.41 indicates an acceptable, but not exceptionally well description of the data. All fit parameters are reasonably constrained; the parameters of the Wien component and the intersection energy are similar to those obtained for GX 304−1.

For MAXI J0655−013, the residuals and the fit statistic indicate that the spectrum can be well described with the `doublehump` model. While the soft component parameters are constrained comparable well, the intersection energy and Wien temperature are only poorly constrained.

For Cepheus X-4, the residuals indicate that a good description of the data can be obtained by the `doublehump` model; the reduced fit statistic is below unity. The Wien temperature and intersection energy are well constrained to intervals smaller than 1 keV; both parameters are lower than obtained for the other sources, which hints at possible correlations between CRSF energy and the Wien component's parameters. With a luminosity of $\sim 4 \times 10^{34}\,\mathrm{erg\,s^{-1}}$ it is the brightest among the small sample of observations.

Lastly, I report on the fit obtained for the spectrum of MAXI J1409−619. Both fit statistic and residuals indicate a good description of the data; the parameters however are however exceptionally poorly constrained, especially those of the Wien component, the intersection energy of the two components is found to be within 6.5–20 keV. I discuss possible explanations for these large uncertainty intervals below, but already here it is clear that this observation and the fit to it is of no use for the subsequent analysis of the nonthermal component.

Table 4.7: Parameters of `doublehump` spectral fits shown in Fig. 4.8.

Parameter	GX 304−1	A0535+26	GRO J1008−57	X Per	SRGA J124404.1-632232	MAXI J0655−013	Cep X−4	MAXI J1409−619
C_{FPMB}	1.033 ± 0.017	0.967 ± 0.014	1.02 ± 0.04	0.9805 ± 0.0026	1.02 ± 0.04	0.98 ± 0.05	1.01 ± 0.04	1.29 ± 0.10
$C_{\mathrm{XRT/EPN}}$	0.87 ± 0.04	$0.82^{+0.12}_{-0.11}$	$0.58^{+0.17}_{-0.08}$	–	–	$0.36^{+0.14}_{-0.12}$	$0.38^{+0.20}_{-0.19}$	$0.8^{+0.8}_{-0.7}$
C_{EMOS1}	$1.02^{+0.06}_{-0.05}$	–	–	–	–	–	–	–
C_{EMOS2}	0.93 ± 0.05	–	–	–	–	–	–	–
$N_{\texttt{cutoffpl}}\left[\times 10^{-3}\right]$	1.07 ± 0.07	$1.9^{+0.5}_{-0.4}$	1.3 ± 0.4	$(1.098 \pm 0.022) \times 10^{2}$	$0.46^{+0.06}_{-0.05}$	$1.3^{+0.6}_{-0.5}$	$0.57^{+0.55}_{-0.30}$	$0.04^{+335.50}_{-0.04}$
Γ	-0.56 ± 0.09	-0.67 ± 0.27	$0.95^{+0.28}_{-0.32}$	$1.062^{+0.022}_{-0.023}$	$-0.15^{+0.17}_{-0.20}$	$0.3^{+0.5}_{-0.6}$	$-0.9^{+1.1}_{-1.2}$	$-1.5^{+2.3}_{-3.2}$
E_{fold} [keV]	1.76 ± 0.06	$2.00^{+0.20}_{-0.17}$	$5.5^{+1.7}_{-1.3}$	$7.37^{+0.19}_{-0.18}$	2.7 ± 0.4	$3.6^{+1.5}_{-1.0}$	$1.6^{+0.8}_{-0.5}$	$1.54^{+9.82}_{-0.11}$
$k_{\mathrm{B}}T_{\mathrm{Wien}}$ [keV]	6.6 ± 0.4	6.14 ± 0.16	12^{+6}_{-4}	13.0 ± 0.4	$6.0^{+1.3}_{-1.1}$	$8.3^{+2.9}_{-2.1}$	$5.3^{+0.5}_{-0.4}$	$4.0^{+2.3}_{-0.7}$
$E_{\mathrm{intersect}}$ [keV]	12.11 ± 0.25	$10.55^{+0.25}_{-0.24}$	$20.6^{+3.5}_{-3.0}$	24.8 ± 0.4	12.6 ± 1.6	$15.7^{+3.3}_{-2.7}$	$7.8^{+0.7}_{-0.5}$	$8.3^{+12.0}_{-1.8}$
$\mathcal{L}\left[10^{34}\,\mathrm{erg\,s^{-1}}\right]$ **(a)**	0.26	1.39	0.66	3.24	3.06	0.87	3.79	0.35
χ^2/d.o.f.	615/553	721/590	476/457	1241/782	590/418	231/219	339/390	62/76
χ^2_{red}	1.11	1.22	1.04	1.59	1.41	1.06	0.87	0.82

a) Absorbed luminosity in the observer's frame in the 5–50 keV energy band.

I note that for SRGA J124404.1-632232 as well as MAXI J0655−013 and MAXI J1409−619 the energy flux spectrum itself does not necessarily suggest that the physical motivation of the `doublehump` model is correctly applied here, where I aim to identify a thermal and nonthermal hump-shaped component. For the latter two sources, the doubt about the applicability of the `doublehump` model is further supported by the poor constraints achieved for the Wien component parameters. In order to investigate this claim and provide motivation that for the spectra of the other sources a physically meaningful description of the data can be obtained by applying the `doublehump` model, I employ the following strategy:

I fit the X-ray spectrum of the above analysed observations in the energy range from 3.5 keV up to the determined intersection energy, e.g. 3.50–12.11 keV for GX 304−1. The spectral model only accounts for the thermal component, which is modeled using a `cutoffpl` component. This model is fitted to the 3.5 keV–$E_{\mathrm{intersect}}$ energy range and subsequently evaluated over the whole *NuSTAR* energy range of 3.5–79 keV. If the residuals show an excess in the hard X-ray band it is an indicator that when interpreting the soft X-ray emission as the thermal component, a nonthermal component is also present. I emphasize that this does *not* directly imply that a `cutoffpl` fit alone is not able to obtain a satisfactory description of the data, but only indicates that when the soft emission is interpreted as the thermal component, a nonthermal component is also detected. Generally however, a simple `cutoffpl` fit is in most cases not able to obtain a satisfactory description of the data as the literature of the past decades has shown (see, e.g., Staubert et al., 2019, and references therein) The obtained residuals are shown in Fig. 4.10.

For GX 304−1 and A0535+26 large excesses at energies of 15–40 keV are evident, which are a strong indicator for applicability of the `doublehump` model. For GRO J1008−57 only a slight excess at energies of 25–60 keV is present, the inclusion of the nonthermal component however leads to decrease in fit statistic by $\Delta\chi^2 = 46$, which also brings the reduced statistic much closer to unity. The residuals of the fit to the X-ray spectrum of X Persei show large deviations at energies exceeding 25 keV extending up to ~80 keV. The residuals of the fit to the SRGA J124404.1-632232 spectrum show a very minor excess at energies of 10–40 keV. MAXI J0655−013 is a similar case, where minor deviations from the model at energies of 20–50 keV are present; here however the reduced fit statistic of 1.30 is not as indicative of a missing component as in the case of SRGA J124404.1-632232. The residuals of the fit to the spectrum of Cepheus X-4 show drastic deviations at energies of 8–25 keV, which is a strong indicator for the presence of a nonthermal component. For MAXI J1409−619, I report an excess from 8–30 keV. Generally however, the *NuSTAR* dataset of MAXI J1409−619 has too poor constraints to use the dataset for subsequent analysis of the nonthermal component; it is therefore not considered in the following.

In summary, in this section I have shown that the X-ray spectra of a small sample of BeXRBs at low luminosities can be described by a model consisting of a `cutoffpl` component for the thermal hump and a `wienhump` component for the nonthermal hump. The here shown results can further be seen as evidence that the soft and hard X-ray spectra behave differently at low luminosities and that a treatment with two components is justified.

4.6 Surface magnetic field estimates from spectral components

In the previous section I have obtained a phenomenological description of seven X-ray spectra exhibiting double-hump spectra. Four of the seven sources (GX 304−1, A0535+26, GRO J1008−57 and Cepheus X-4) are known to exhibit cyclotron lines in their X-ray spectra, which allow to in-

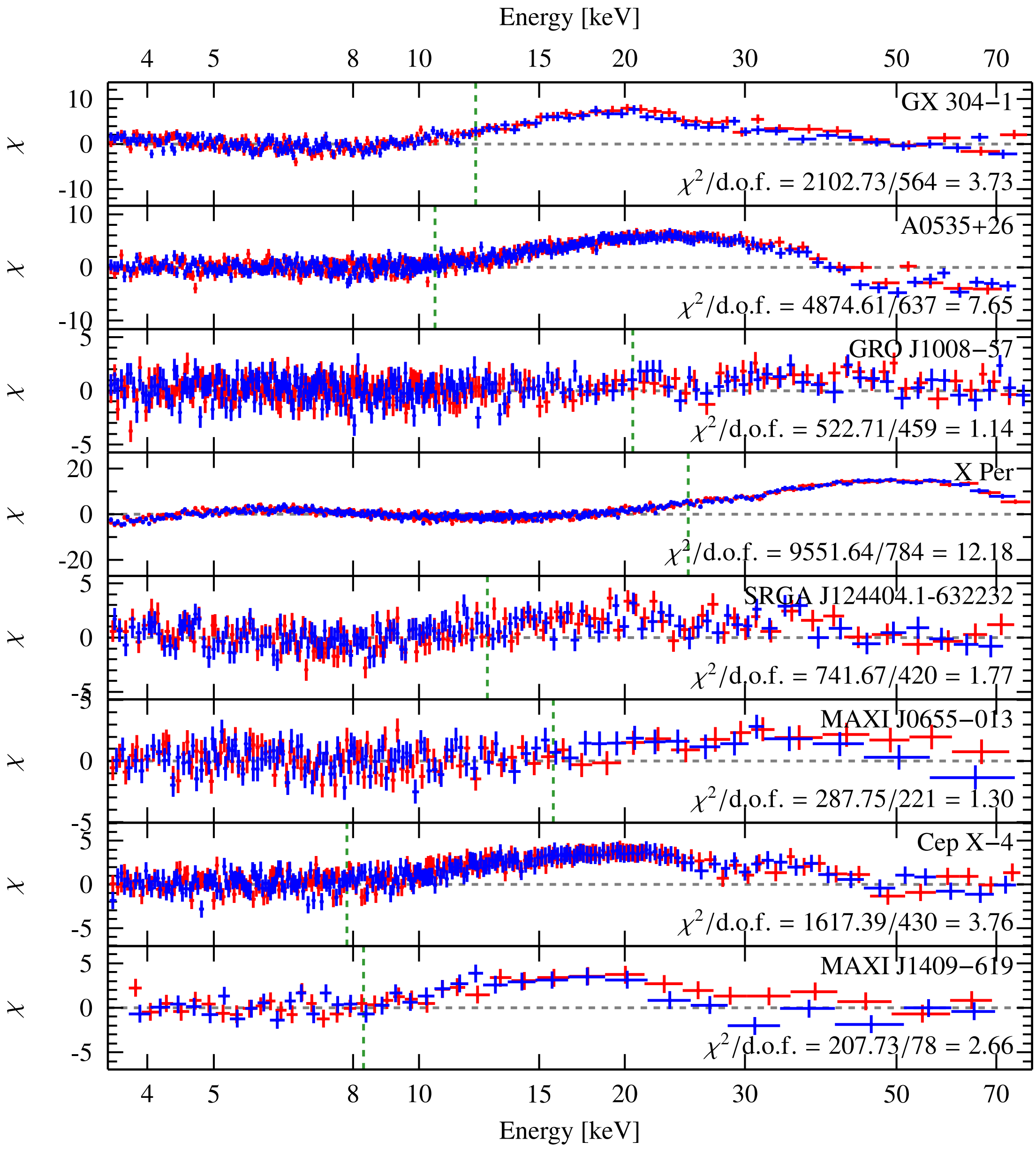

Figure 4.10: Investigation of presence of two component spectra with residuals. Shown are the residuals of `cutoffpl` fits in the energy range from 3.5 keV up to $E_{\mathrm{intersect}}$, which is indicated by a dashed green line.

fer the magnetic field strength[5]. As the energy of the nonthermal hump is related to the cyclotron energy, I aim to relate the two quantities and obtain an empirical relation between them. Specifically, I aim to relate the intersection energy of the two components as introduced in the previous section with the cyclotron line energy as stated in the literature. For the sources with known cyclotron lines, I show the observed cyclotron line energy as a function of the here determined intersection energy in Fig. 4.11.

Fig. 4.11 suggests a positive correlation between the magnetic field strength as indirectly measured as the cyclotron line energy and the intersection energy of the two component. It is

[5]This list intentionally excludes X Persei as the previously reported CRSF at ~29 keV (see, e.g., Coburn et al., 2001) is in this work understood as the dip between the thermal and nonthermal component and *not* the result of absorption due to cyclotron resonant scattering.

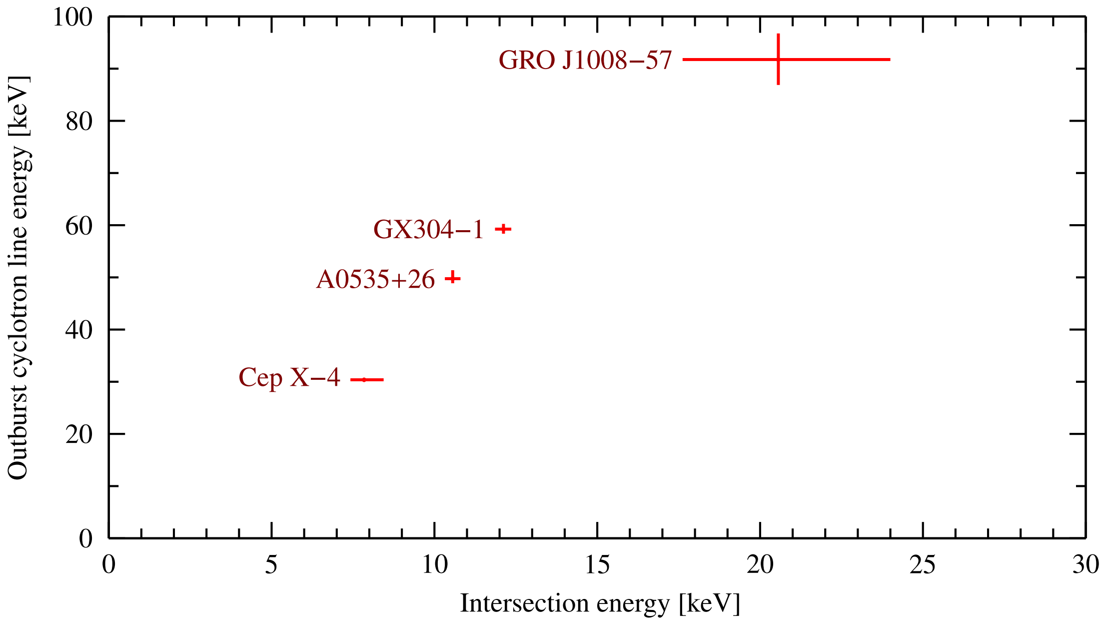

Figure 4.11: Outburst cyclotron line energy as a function of intersection energy of the two components. References for the cyclotron line energies: Fürst et al. (Cepheus X-4, 2015), Sartore et al. (A0535+26, 2015), Malacaria et al. (GX 304−1, 2015) and Chen et al. (GRO J1008−57, 2021).

however also clear that it is not possible to infer a precise mathematical relation between the two quantities due to the low number of data points. In order to estimate an approximate relation between the two quantities, I fit a linear curve to the four data points. As the uncertainties of the Cepheus X-4, A0535+26 and GX 304−1 data points are significantly smaller than for GRO J1008−57, the fitting algorithm would completely disregard the latter data point; I therefore do not include the uncertainties in the fitting procedure to obtain a approximate relation between the CRSF and intersection energies. The four data points along with the linear fit to them are shown in Fig. 4.12. The figure also shows the predicted CRSF energies for X Persei, MAXI J0655−013 and SRGA J124404.1-632232, which are obtained from the linear relation. Their uncertainties are estimated by sampling the distribution of CRSF energies as obtained from the linear relation considering both the parameter and intersection energy uncertainties. I note however, that this relation should be understood only as an estimate and should not be used to make precise predictions of CRSF energies at this stage. In order to obtain a more resilient description of the data, more data points are required, which implies a need for more observations of XRBs with known magnetic field strengths at low luminosities, e.g. during the decay of outbursts.

In order to better understand the exact relation between the cyclotron line energy and intersection energy and to compare with the above found positive correlation, I make use of the `polcap` model, which provides an accurate description of low luminosity X-ray spectra. From this theoretical model I aim to obtain a relation between the cyclotron interaction energy and the intersection energy for three different mass fluxes[6] spanning the whole mass flux range available in the tabulated model, i.e. $\log\left(\dot{M}/A_{\mathrm{cap}}\right)$ between 4.8–5.9. The cyclotron energies utilised for

[6]Contrary to the parametrisation described in Sokolova-Lapa et al. (2021), the current realisation of the `polcap` model takes normalisation (which accounts for the ratio between polar cap area and source distance in units of $\mathrm{m^2\,kpc^{-2}}$), cyclotron energy in the NS frame in keV and the mass flux, which is the mass accretion rate divided by the area of the polar cap in units of $\log\left(\mathrm{g\,s^{-1}\,cm^{-2}}\right)$, onto which the matter is accreted, as input parameters.

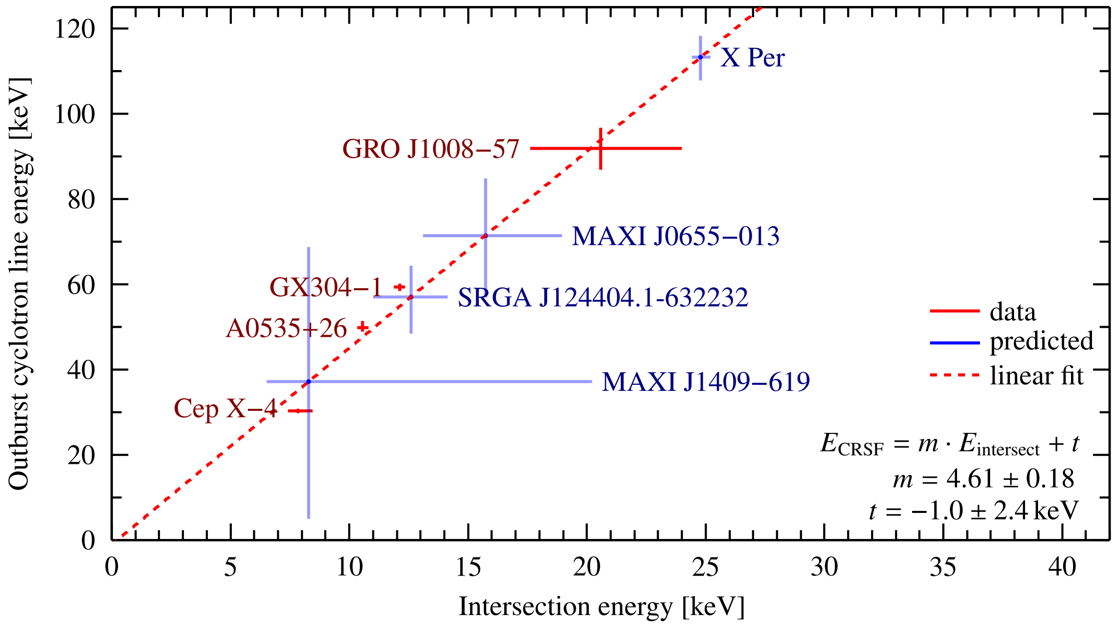

Figure 4.12: Linear fit to relation between CRSF and intersection energy. Data points identical to those shown in Fig. 4.11. Linear fit shown as dashed red curve with parameters as given in the inset. The predicted CRSF energies as a function of intersection energy are shown in blue.

the simulation are 100 values linearly spaced between 50–80 keV in the NS rest frame. For each combination of mass flux value and cyclotron energy I employ the below described strategy.

1. For a given pair of mass flux and cyclotron line energy, I simulate 10^3 *NuSTAR* observations with exposure times of 100 ks for which background, ARF, and RMF are taken from the GX 304−1 observation performed in 2022. All spectra are simulated such that the absorbed ($N_\mathrm{H} = 1 \times 10^{22}\mathrm{cm}^{-2}$) luminosity in the *NuSTAR* band is $1 \times 10^{34}\,\mathrm{erg\,s}^{-1}$.

2. Each simulated spectrum is fitted with the `doublehump` model as given in Eq. 4.8.

3. The 10^3 simulated spectra per cyclotron energy value provide a distribution of $E_{\mathrm{intersect}}$, for which I calculate the smallest 90% interval as well as the mode, which I take as uncertainty interval and value of the intersection energy for the given mass flux and cyclotron energy.

One could argue that instead of simulating 10^3 spectra for each parameter combination and then sampling the distribution of intersection energy values one could also just simulate one spectrum and then calculate the uncertainty of the intersection energy; just using one simulated spectrum poses the disadvantage that the obtained result strongly depends on that simulated spectrum, which can be circumvented by simulating a large number of spectra in order to gain a more precise understanding of the intersection energy parameter space. The obtained intersection energies as a function of CRSF energy for the three mass flux values are shown in Fig. 4.13[7]

It is evident that there exists a linear relation between the cyclotron energy and the intersection energy, which especially for the low and medium mass flux data require a breaking at ~13 keV. For the high mass flux data this breaking is less obvious, but still required to obtain

[7]Given that the cyclotron energy is the input parameter for the simulation, one might expect that it is the ordinate of the shown figure. For later usage however the inverse is much more useful as one would determine the intersection energy and then use it to estimate the cyclotron energy.

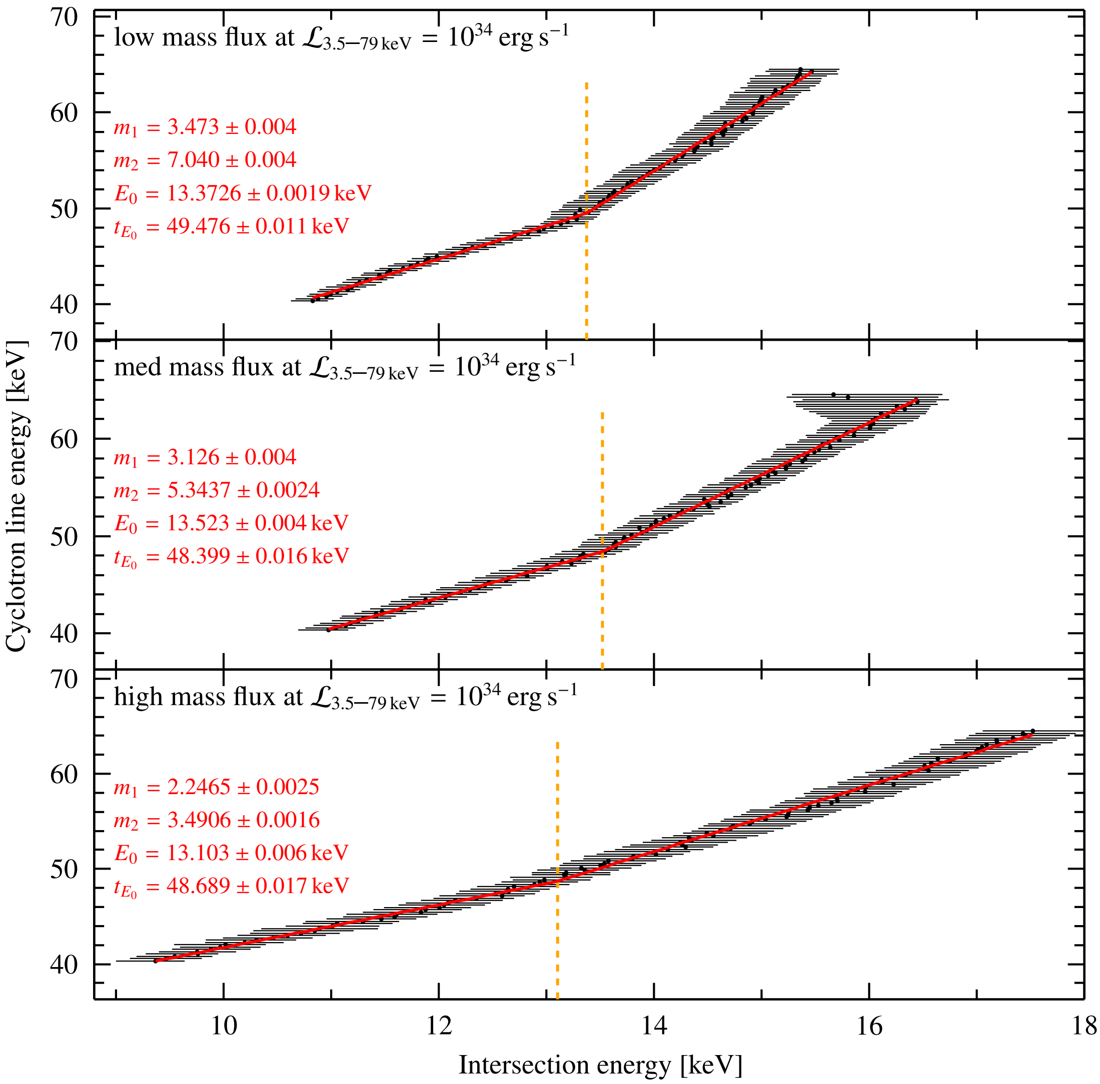

Figure 4.13: Cyclotron energy versus intersection energy for three different mass fluxes. The cyclotron line energy is given in the observer's frame, i.e. the corresponding `polcap` parameter E_{cyc} has been divided by the factor $(1 + z)$ with $z = 0.24$. Shown in black are the data points as obtained from simulated spectra; shown in red are the broken linear fits to the data with orange dashed lines indicating the breaking energy E_0. The parameters are given in the insets.

a good description of the data. The parameters of the broken linear fits are given in Table 4.8. The breaking energy E_0 varies only slightly between the three fits within 13.1–13.5 keV. The slope of the lower linear component is comparable to that determined from the experimental data with values between 2.2–3.5. The slope of the higher linear component is generally steeper with values between 3.5–7.0. The difference in linear slopes between the two components is largest for the low mass flux data with $\Delta m \sim 3.6$ and lowest for the high mass flux data with $\Delta m \sim 1.2$. While it is difficult to provide a physical explanation why the observed relation is a broken linear one, it is still highly useful to compare with the relation derived from experimental data as shown in Fig. 4.11. Based on the 4 data points shown in that figure, it is also evident that a broken linear relation cannot be fitted to it, as then the number of degrees of freedom would be zero and a "perfect" description of the data can always be obtained, which is self-evidently not meaningful. In order to compare the relations determined from experimental data and sim-

Table 4.8: Parameters of broken linear fits shown in Fig. 4.13.

Parameter	low mflux	medium mflux	high mflux
m_1	3.473 ± 0.004	3.126 ± 0.004	2.2465 ± 0.0025
m_2	7.040 ± 0.004	5.3437 ± 0.0024	3.4906 ± 0.0016
E_0 [keV]	13.3726 ± 0.0019	13.523 ± 0.004	13.103 ± 0.006
t_{E_0} [keV]	49.476 ± 0.011	48.399 ± 0.016	48.689 ± 0.017

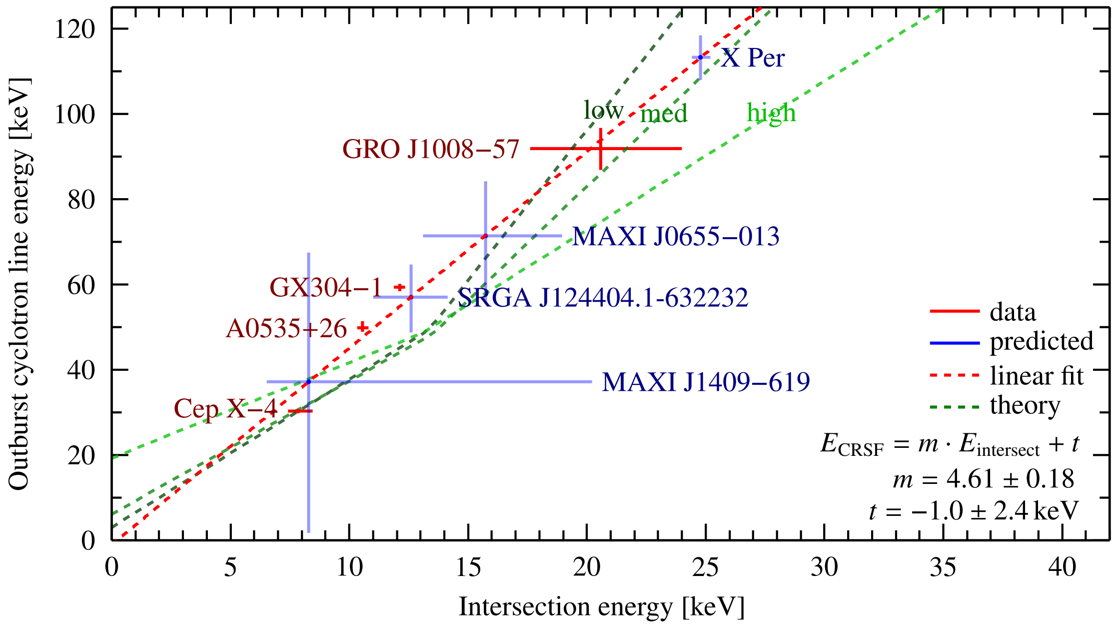

Figure 4.14: Relation between intersection energy and cyclotron line energy as determined from data and simulations based on theoretical models. Red data points: sources for which the fundamental CRSF energy is known. Red curve: fitted linear relation to red data points (disregarding uncertainties) with parameters as given in the inset. Blue data points: sources for which CRSF energies are not known, for which the CRSF energy and its uncertainty is derived form the linear fit shown in red. Green curves: broken linear curves for low, medium, and high mass flux values as obtained from simulations shown in Fig. 4.13.

ulations based on the `polcap` model I show them together in Fig. 4.14. The obtained relations between intersection and CRSF energies generally show the same positive correlation.

I report that the data points for Cepheus X-4, A0535+26, GX 304−1 and GRO J1008−57 as obtained from *NuSTAR* observations and the linear fit to them show a remarkable similar relation of CRSF and intersection energy as obtained from the simulated `polcap` spectra. At CRSF energies below ~50 keV, the theoretical curves show no strong dependence on mass flux as their slopes are comparably similar. At higher energies (i.e. energies exceeding the breaking energy E_0) the three curves diverge as the slope for the low mass flux simulations is higher than for the one with high mass flux. For sources with known magnetic field strength and intersection energy, this poses the interesting prospect of making statements about the mass flux level. For example, for GRO J1008−57 the green curves in Fig. 4.14 indicate an intermediate to high mass flux level, although much better constraints on the intersection energy are required to make this a credible statement. In theory, this predicted mass flux level could be verified by directly

Table 4.9: Cyclotron line energies and magnetic field strengths as estimated from the intersection energy. For each obtained relation and source, I give both quantities. The uncertainties are estimated by sampling the (broken) linear relations 1000 times and computing the smallest 90% intervals. Values and uncertainties should be taken as a rough estimate and not used for further analyses.

Source	$E_{\text{intersect}}$ [keV]	$E_{\text{CRSF}}^{\text{predicted}}$ [keV]	$B_{\text{surface}}\left[10^{12}\,\text{G}\right]$
X Per	24.8 ± 0.4	113 ± 6	12.1 ± 0.6
SRGA J124404.1-632232	12.6 ± 1.6	57^{+8}_{-9}	6.1 ± 0.9
MAXI J0655−013	$15.7^{+3.3}_{-2.7}$	71^{+13}_{-16}	$7.7^{+1.4}_{-1.7}$
MAXI J1409−619	$8.3^{+12.0}_{-1.8}$	$(4 \pm 4) \times 10^{1}$	4 ± 4

applying the `polcap` model to the observation. Right now, this is not feasible as the model is only tabulated up to magnetic field strengths corresponding to a cyclotron energy of 80 keV in the NS frame (~65 keV in the observer's frame), which is not sufficiently high to properly model the X-ray spectrum GRO J1008−57.

The four obtained linear relations (one from data and three from theory) can however also be used to estimate the cyclotron line energy and thus magnetic field strength of the sources for which the quantities are not known. It is however clear that both the estimated values and their uncertainties should only be taken as rough estimates and should not be used as for subsequent research; the data-obtained relation relies on four data points which is insufficient to obtain a reliable relation. For the theory-driven relations one must consider that in order to make use of them knowledge of the mass flux regime of the observation is required, which is not necessarily the case. Keeping the above caveats in mind, I estimate the CRSF energy and magnetic field strength for X Persei, SRGA J124404.1-632232 and MAXI J0655−013 for each of the four obtained relations. The respective values are given in Table 4.9.

While the here obtained relations between CRSF and intersection energy and the subsequent result should only be seen as estimates, I will now provide brief suggestions to obtain more reliable results. The main limitation of this analysis is the few number of sources with known magnetic field strengths, for which observations in quiescence are available. To increase this number, two types of observations are required: firstly, observations during outbursts are needed to reliably constrain the cyclotron line energy. Secondly, observations during quiescence are needed in order to determine the spectral shape in quiescence and, if a double-hump spectrum is present, the intersection energy. For example, 1A 1118−61 (see, e.g., Eyles et al., 1975) is a transient BeXRB system, which was observed twice during its outburst in 2009 (see Maitra et al., 2012) and is known to exhibit a broad CRSF centered at ~55 keV (Doroshenko et al., 2010b), whose quiescent state has not yet been analyzed. There is a low number ($\lesssim$10) of other transient BeXRBs, for which observations in quiescence or following outbursts would be valuable for the investigation of the low luminosity state.

On the theoretical side, models like `polcap` provide the possibility to simulate spectra, model real observations and test routines such as the one shown in this work. Especially for this work a larger tabulated range of CRSF energies is required as for most sources with unknown CRSFs the above described routine predicts CRSFs at energies above `polcap`'s limit, which can only be checked for consistency by extending the tabulated CRSF energy.

5 | Conclusion and outlook

With this work I hope to provide a small contribution to the investigation of the quiescent state of Be X-ray binaries. Here I do not restrict the spectral investigation of BeXRBs in quiescence to a single source, but take a larger sample of BeXRBs as a basis, that is only limited by the availability of *NuSTAR* observations in the quiescent state. For all of them I have investigated whether the X-ray spectra differ from the typical cutoff-powerlaw shape found at higher luminosities and concluded that this is indeed the case. Instead, a double-hump spectral model, which is understood to consist of a thermal and nonthermal component originating in the NS atmosphere, reproduces the observed X-ray spectra well.

Apart from contributing evidence that accretion continues in the quiescent state, this work provides the most systematic study of hard X-ray emission and pulse profiles in quiescence. It further delivers a means to access cyclotron line energies, and most importantly magnetic field strengths, beyond *NuSTAR*'s energy range of 79 keV, which can help to extract even more information from typical observations of sources in the quiescent state than before. But also for CRSFs at energies below 79 keV this method proves useful as CRSFs often cannot be clearly identified due to low signal-to-noise ratios and subsequent low statistical confidences in them.

Undoubtedly, the relation obtained here between magnetic field strength and spectral components should not be understood as a precise law, but more as an estimate. It is primarily limited by the low number of broadband quiescent observations that are available and more generally by the low number of known BeXRBs that enter such a state. It can also be applied as a consistency test for other methods to estimate the CRSF energy; for example torque modeling, where models such as that by Ghosh & Lamb (1979) are used to infer the magnetic field strength from long-term observational campaigns or X-ray monitors, as done by Yatabe et al. (2018) for X Persei, who find a magnetic field strength in excess of 10^{13} G. Also, the modeling of pulsed fraction spectra is known to be a viable method to identify cyclotron lines and infer their centroid energy (see, e.g., Ferrigno et al., 2023).

This study does not directly allow to draw conclusions about the accretion mechanism in the quiescent state, whose investigation is beyond the scope of this work, but I give a brief outlook over ongoing research and proposed mechanisms, that explain the stable accretion at low luminosities.

Quiescent accretion in BeXRBs has already been discussed for individual sources such as GRO J1008−57 by Tsygankov et al. (2017), who have found that the source does not enter the propeller regime[1] at low luminosities and shows stable accretion with $\dot{M} \sim 10^{14}$–$10^{15}\,\mathrm{g\,s^{-1}}$. Tsygankov et al. (2017) suggest for the state of quiescent accretion, as observed in GRO J1008−57, that the accretion process could be supplied with matter originating from a cold ($T < 6500\,\mathrm{K}$) accretion disk around the compact object. Accretion from a cold disk has also been suggested

[1]Although not unambiguously defined in the literature, the propeller effect generally implies a centrifugal barrier, where matter is first gravitationally captured by the NS, then halted at the magnetospheric boundary, where it moves at a Super-Keplerian velocity, which prevents it from being accreted onto the neutron star (see, e.g., Illarionov & Sunyaev 1975 and Sokolova-Lapa 2023 for discussions of the propeller effect).

for multiple other sources: Tsygankov et al. (2019b) argue that IGR J19294+1816 accretes from a cold accretion disk between its regular type I outbursts; Rouco Escorial et al. (2018) and Doroshenko et al. (2014) discuss the accretion from cold disks for GX 304−1 and A0535+26, respectively. As noted by Rouco Escorial et al. (2018), accretion form non-ionised disks during quiescence is only possible for slowly rotating, magnetized NSs with rotation periods exceeding tens of seconds and surface magnetic field strengths of 10^{12}–10^{13} G as otherwise the propeller effect sets in. Furthermore, the modeling of accretion disks can also be used to explain the outburst decay of transient sources: the LMXB Aql X-1 showed a rapid flux decline near the end of its 2013 outburst, which Lipunova et al. (2022) successfully reproduce with their model of a hot accretion disk, where they interpret the flux decrease as a radial shrinking of the disk.

Apart from remnant accretion disks around the neutron star, the role of Be star decretion disks (see, e.g., Rivinius et al., 2013) has also been discussed in this context. While accretion from the decretion disk itself during periastron passage cannot explain the *stable* quiescent accretion during the whole NS orbit, they may play a crucial role to explain the outburst behaviour of transient BeXRBs. Okazaki & Negueruela (2001) apply a viscous decretion disk model and argue that for BeXRBs the truncation of the decretion disk is in some cases expected to be such that mass transfer onto the compact object during the periastron passages is too low for periodic type I outbursts to occur. Instead, the Be decretion disk grows until it becomes dynamically unstable, when mass is being transferred from the disk onto the neutron star in a not yet well understood process, which results in aperiodic type II outbursts. More recently, eccentric decretion disks have been shown to lead to oscillations between disk inclination and eccentricity (Martin & Franchini, 2019), which in some cases can lead to instabilities that result in giant outbursts; Martin & Franchini (2019) successfully reproduced the giant outburst behaviour of the BeXRB 4U 0115+63. It is still unclear to which extent the decretion disk is accreted by the NS during outbursts and on which timescales decretion disks are generally replenished. To investigate the latter, Ghoreyshi et al. (2018) analysed a four-decade optical campaign of Be star ω CMa, during which the decretion disk underwent four full cycles of formation and dissipation and allowed the authors to successfully apply a VDD.

Another challenge in the field of accreting BeXRBs in quiescence is the low number of known sources and comparably few high-quality observations that are available. The number of (potentially transient) BeXRBs accreting in quiescence can be increased by sensitive all-sky surveys such as *eROSITA*, which periodically scan the sky and are able to detect faint sources; eRASSU J012422.9-724248 is such a newly discovered BeXRB system in the SMC (see Maitra et al., 2023) for which a follow-up observation with *NuSTAR* was carried out. Also, new observations of already known BeXRBs in quiescence are valuable for the magnetic field estimation presented in this work regardless of whether the magnetic field strength is indirectly measurable in the form of cyclotron lines, as both sources with known and unknown magnetic field strength would constitute an interesting science case to either refine or test the obtained relation.

In the context of BeXRBs in quiescence, this work serves as a further indicator that accretion does not cease in the quiescent state and can be treated in a systematic way. It also has shown that the magnetic field strength can be estimated from typical *NuSTAR* observations, even when potential CRSFs are not within the instrument's energy range, which has the potential to provide a small contribution to our knowledge of Be X-ray binaries harboring accreting neutron stars in quiescence.

Bibliography

Albert J., Aliu E., Anderhub H., et al., 2007, ApJ 665, L51

Arnaud K.A., 1996, In: Jacoby G.H., Barnes J. (eds.) Astronomical Data Analysis Software and Systems V, Vol. 101. Astronomical Society of the Pacific Conference Series, p. 17

Avakyan A., Neumann M., Zainab A., et al., 2023, A&A 675, A199

Baade W., Zwicky F., 1934, Phys. Rev. 46, 76

Bailer-Jones C.A.L., Rybizki J., Fouesneau M., et al., 2021, AJ 161, 147

Ballhausen R., 2021, Ph.D. thesis, Friedrich-Alexander-Universität Erlangen-Nürnberg

Ballhausen R., Pottschmidt K., Fürst F., et al., 2017, A&A 608, A105

Ballhausen R., Thalhammer P., Pradhan P., et al., 2024, A&A 688, A214

Barthelmy S.D., Barbier L.M., Cummings J.R., et al., 2005, Space Sci. Rev. 120, 143

Baykal A., Inam Ç., Ali Alpar M., et al., 2001, MNRAS 327, 1269

Becker P.A., Klochkov D., Schönherr G., et al., 2012, A&A 544, A123

Bell S.J., Hewish A., 1967, Nature 213, 1214

Bodensteiner J., Shenar T., Sana H., 2020, A&A 641, A42

Bonnet-Bidaud J.M., Mouchet M., 1998, A&A 332, L9

Branch D., Tammann G.A., 1992, ARA&A 30, 359

Buckley D.A.H., Gromadzki M., Townsend L., et al., 2021, ATel 14364

Burrows A., Vartanyan D., 2021, Nature 589, 29

Burrows D.N., Hill J.E., Nousek J.A., et al., 2005, Space Sci. Rev. 120, 165

Cadonau R., Sandage A., Tammann G.A., 1985, LNP 224, 151

Cash W., 1979, ApJ 228, 939

Chadwick J., 1932, Proc. R. Soc. A 136, 692

Chaty S., 2011, ASPCS 447, 29

Chen X., Wang W., Tang Y.M., et al., 2021, ApJ 919, 33

Chernyakova M., Lutovinov A., Rodríguez J., Revnivtsev M., 2005, MNRAS 364, 455

Coburn W., Heindl W.A., Gruber D.E., et al., 2001, ApJ 552, 738

Coburn W., Heindl W.A., Rothschild R.E., et al., 2002, ApJ 580, 394

Coe M.J., Bird A.J., Hill A.B., et al., 2007, MRNAS 378, 1427

Coe M.J., Roche P., Everall C., et al., 1994, MNRAS 270, L57

Coleiro A., Chaty S., Zurita Heras J.A., et al., 2013, A&A 560, A108

Demtröder W., 2014, Experimentalphysik 4, Springer-Lehrbuch, Springer Berlin Heidelberg, 4. aufl. 2014 edition

den Herder J.W., Brinkman A.C., Kahn S.M., et al., 2001, A&A 365, L7

Dickey J.M., Lockman F.J., 1990, ARA&A 28, 215

Dönmez Ç.K., Serim M.M., İnam S.Ç., et al., 2020, MNRAS 496, 1768

Dorman B., Arnaud K., 2001, In: F.R., Jr. H., Primini F.A., Payne H.E. (eds.) Astronomical Data Analysis Software and Systems X, Vol. 238. Astronomical Society of the Pacific Conference Series, p. 415

Doroshenko V., Santangelo A., Doroshenko R., et al., 2014, A&A 561, A96

Doroshenko V., Santangelo A., Kreykenbohm I., Doroshenko R., 2012, A&A 540, L1

Doroshenko V., Santangelo A., Suleimanov V., et al., 2010a, A&A 515, A10

Doroshenko V., Staubert R., Maitra C., et al., 2022, A&A 661, A21

Doroshenko V., Suchy S., Santangelo A., et al., 2010b, A&A 515, L1

Einstein A., 1916, Ann Phys 354, 769

Eyles C.J., Skinner G.K., Willmore A.P., Rosenberg F.D., 1975, Nature 254, 577

Ferrario L., Wickramasinghe D.T., 2005, MNRAS 356, 615

Ferrigno C., Becker P.A., Segreto A., et al., 2009, A&A 498, 825

Ferrigno C., D'Aì A., Ambrosi E., 2023, A&A 677, A103

Foreman-Mackey D., Hogg D.W., Lang D., Goodman J., 2013, Publ. Astron. Soc. Pac. 125, 306

Frank J., King A., Raine D.J., 2002, Accretion Power in Astrophysics: Third Edition, Cambridge University Press, Cambridge

Fürst F., Falkner S., Marcu-Cheatham D., et al., 2018, A&A 620, A153

Fürst F., Pottschmidt K., Miyasaka H., et al., 2015, ApJ 806, L24

Fürst F., Suchy, S.Kreykenbohm, I.et al., 2011, A&A 535, A9

Gaia Collaboration 2016, A&A 595, A1

Gaia Collaboration 2023, A&A 674, A1

Gamow G., 1970, My World Line: An Informal Autobiography., Viking Press, New York, NY

Gamow G., Schoenberg M., 1941, Phys. Rev. 59, 539

Gehrels N., Chincarini G., Giommi P., et al., 2004, ApJ 611, 1005

Ghimiray M., Sharma P., Subba N., 2024, MNRAS 531, 3386

Ghoreyshi M.R., Carciofi A.C., Rímulo L.R., et al., 2018, MNRAS 479, 2214

Ghosh P., Lamb F.K., 1979, ApJ 234, 296

Giovannelli F., Graziati L.S., 1992, Space Sci. Rev. 59, 1

Goodman J., Weare J., 2010, Comm. Appl. Math. Com. Sc. 5, 65

Haigh N.J., Coe M.J., Fabregat J., 2004, MNRAS 350, 1457

Hanslmeier A., 2002, Einführung in Astronomie Und Astrophysik, Springer Berlin Heidelberg

Harrison F.A., Boggs S., Christensen F., et al., 2010, In: Arnaud M., Murray S.S., Takahashi T. (eds.) Proc. of Space Telescopes and Instrumentation (SPIE), Vol. 7732., p. 77320S

Harrison F.A., Craig W.W., Christensen F.E., et al., 2013, ApJ 770, 103

Hawking S.W., 1975, Commun. Math. Phys. 43, 199

Heindl W.A., 2000, In: AIP Conference Proceedings, Vol. 510., AIP, Portsmouth, New Hampshire (USA), p.173

Heindl W.A., Coburn W., Gruber D.E., et al., 1999, ApJ 521, L49

Hewish A., Bell S.J., Pilkington J.D.H., et al., 1968, Nature 217, 709

Hewish A., Okoye S.E., 1965, Nature 207, 59

HI4PI CollaborationBen Bekhti N., Flöer L., et al., 2016, A&A 594, A116

Houck J.C., Denicola L.A., 2000, In: Manset N., Veillet C., Crabtree D. (eds.) Astronomical Data Analysis Software and Systems IX, Vol. 216. Astronomical Society of the Pacific Conference Series, p. 591

Iben, Jr. I., Tutukov A.V., Yungelson L.R., 1995, ApJS 100, 217

Illarionov A.F., Sunyaev R.A., 1975, A&A 39, 185

Iwakiri W.B., Pottschmidt K., Falkner S., et al., 2019, ApJ 878, 121

Janka H.T., 2012, Annu. Rev. Nucl. Part. Sci. 62, 407

Janka H.T., Langanke K., Marek A., et al., 2007, Phys. Rep. 442, 38

Jansen F., Lumb D., Altieri B., et al., 2001, A&A 365, L1

Johnston S., Karastergiou A., 2017, MNRAS 467, 3493

Kaastra J.S., Bleeker J.A.M., 2016, A&A 587, A151

Kalberla P.M.W., Burton W.B., Hartmann D., et al., 2005, A&A 440, 775

Kaper L., van der Meer A., Najarro F., 2006, A&A 457, 595

Kaspi V.M., Beloborodov A.M., 2017, A&AR 55, 261

Kaspi V.M., Helfand D.J., 2002, In: Slane P.O., Gaensler B.M. (eds.) ASP Conference Series, Vol. 271., Boston, MA, p. 3

Kaspi V.M., Tavani M., Nagase F., et al., 1995, ApJ 453, 424

Kaspi V.M., Taylor J.H., Ryba M.F., 1994, ApJ 428, 713

Kennea J.A., Evans P.A., Negoro H., 2022a, ATel 15561

Kennea J.A., Gronwall C., Page K.L., et al., 2022b, ATel 15443

Kennea J.A., Krimm H., Romano P., et al., 2010, ATel 2962

Klochkov D., Doroshenko V., Santangelo A., et al., 2012, A&A 542, L28

Klochkov D., Santangelo A., Staubert R., Ferrigno C., 2008, A&A 491, 833

Koh D.T., Bildsten L., Chakrabarty D., et al., 1997, ApJ 479, 933

Koyama K., Kawada M., Tawara Y., et al., 1991, AJ 366, L19

Kretschmar P., El Mellah I., Martínez-Núñez S., et al., 2021, A&A 652, A95

Kreykenbohm I., Coburn W., Wilms J., et al., 2002, A&A 395, 129

Krimm H.A., Holland S.T., Corbet R.H.D., et al., 2013, ApJS 209, 14

Krivonos R., Wik D., Grefenstette B., et al., 2021, MNRAS 502, 3966

Krivonos R.A., Tsygankov S.S., Lutovinov A.A., et al., 2015, ApJ 809, 140

Kühnel M., Müller S., Kreykenbohm I., et al., 2013, A&A 555, A95

Landau L.D., 1932, Phys. Zs. Sowjet 1, 285

Lattimer J.M., Pethick C.J., Prakash M., Haensel P., 1991, Phys. Rev. Lett. 66, 2701

Leahy D.A., Elsner R.F., Weisskopf M.C., 1983, ApJ 272, 256

Leahy D.A., Kostka M., 2008, MNRAS 384, 747

Levenberg K., 1944, Q Appl Math 2, 164

Lewin W.H.G., Clark G.W., Smith W.B., 1968a, ApJ 152, L49

Lewin W.H.G., Clark G.W., Smith W.B., 1968b, Nature 220, 249

Li F., Rappaport S., Clark G.W., Jernigan J.G., 1979, ApJ 228, 893

Liang E.P., Nolan P.L., 1984, Space Sci. Rev. 38, 353

LIGO Scientific Collaboration and Virgo Collaboration 2016, Phys. Rev. Lett. 116, 061102

LIGO Scientific Collaboration and Virgo Collaboration 2017, Phys. Rev. Lett. 119, 161101

Lipunova G., Malanchev K., Tsygankov S., et al., 2022, MNRAS 510, 1837

Lutovinov A., Tsygankov S., Chernyakova M., 2012, MNRAS 423, 1978

Lutovinov A.A., Revnivtsev M.G., Tsygankov S.S., Krivonos R.A., 2013, MNRAS 431, 327

Lyne A.G., Jordan C.A., Graham-Smith F., et al., 2015, MNRAS 446, 857

Mackay D.J.C., 2003, Information Theory, Inference and Learning Algorithms, Cambridge University Press, Cambridge

Madsen K.K., Harrison F.A., Markwardt C.B., et al., 2015, ApJS 220, 8

Maitra C., Haberl F., Kaltenbrunner D., et al., 2023, ATel 15886

Maitra C., Paul B., Naik S., 2012, MNRAS 420, 2307

Malacaria C., Klochkov D., Santangelo A., Staubert R., 2015, A&A 581, A121

Manikantan H., Paul B., Rana V., 2023, MNRAS 526, 1

Marquardt D.W., 1963, J. Soc. Ind. Appl. Math. 11, 431

Martin R.G., Franchini A., 2019, MNRAS 489, 1797

Masetti N., Pretorius M.L., Palazzi E., et al., 2006, A&A 449, 1139

Mason B.D., Wycoff G.L., Hartkopf W.I., et al., 2001, Astron. J. 122, 3466

Mason K.O., Murdin P.G., Parkes G.E., Visvanathan N., 1978, MNRAS 184, 45P

McClintock J.E., Rappaport S.A., Nugent J.J., Li F.K., 1977, ApJ 216, L15

McCray R.A., Shull J.M., Boynton P.E., et al., 1982, ApJ 262, 301

Meszaros P., Nagel W., 1985 299, 138

Michell J., 1784, Philos. Trans. R. Soc. I 74, 35

Mihara T., 1995, Ph.D. thesis, University of Tokyo

Mihara T., Makishima K., Kamijo S., et al., 1991, ApJ 379, L61

Mihara T., Makishima K., Nagase F., 1995, In: American Astronomical Society Meeting Abstracts, Vol. 187., p. 104.03

Minkowski R., 1941, Publ. Astron. Soc. Pac. 53, 224

Miyasaka H., Harrison F.A., Cook W.R., et al., 2009, In: Siegmund O.H. (ed.) Proceedings of SPIE, Vol. 7435. Proceedings of SPIE, p. 74350Q

Motch C., Stella L., Janot-Pacheco E., Mouchet M., 1991, ApJ 369, 490

Mroz P., Udalski A., 2021, ATel 14361

Mushtukov A.A., Suleimanov V.F., Tsygankov S.S., Portegies Zwart S., 2021, MNRAS 503, 5193

Mushtukov A.A., Tsygankov S.S., Poutanen J., et al., 2023, MNRAS 524, 2004

Nabizadeh A., Mönkkönen J., Tsygankov S.S., et al., 2019, A&A 629, A101

Naik S., Paul B., Ali Z., 2011, ApJ 737, 79

Nakajima M., Negoro H., Mihara T., et al., 2019, In: Oskinova L.M., Bozzo E., Bulik T., Gies D. (eds.) Proceedings IAU Symposium, Vol. 346., International Astronomical Union, p.131

Neumann M., Avakyan A., Doroshenko V., Santangelo A., 2023, A&A 677, A134

Okazaki A.T., Negueruela I., 2001, A&A 377, 161

Orlandini M., Fiume D.D., 2001, In: White N.E., Malaguti G., Palumbo G.G. (eds.) X-RAY ASTRONOMY: Stellar Endpoints, AGN, and the Diffuse X-ray Background., Vol. 599. AIP Conference Proceedings, American Institute of Physics, Melville, NY, p.283

Orlandini M., Frontera F., Masetti N., et al., 2012, ApJ 748, 86

Ott C.D., Burrows A., Thompson T.A., et al., 2006, ApJS 164, 130

Pavlinsky M., Sazonov S., Burenin R., et al., 2022, A&A 661, A38

Perlmutter S., Aldering G., Goldhaber G., et al., 1999, ApJ 517, 565

Petre R., Serlemitsos P.J., 1985, Appl. Opt. 24, 1833

Pétri J., Guillot S., Guillemot L., et al., 2024, A&A 687, L13

Pols O.R., Cote J., Waters L.B.F.M., Heise J., 1991, A&A 241, 419

Possenti A., Cerutti R., Colpi M., Mereghetti S., 2002, A&A 387, 993

Postnov K.A., Mironov A.I., Lutovinov A.A., et al., 2015, MNRAS 446, 1013

Pourshahian S., 2017, J. Am. Soc. Mass Spectrom. 28, 1836

Predehl P., Andritschke R., Arefiev V., et al., 2021, A&A 647, A1

Pringle J.E., 1981, ARA&A 19, 137

Rai B., Tobrej M., Ghising M., et al., 2023, MNRAS 524, 1352

Raman G., VarunPradhan P., Kennea J., 2023, MNRAS 526, 3262

Rawls M.L., Orosz J.A., McClintock J.E., et al., 2011, ApJ 730, 25

Repetto S., Igoshev A.P., Nelemans G., 2017, MNRAS 467, 298

Rivinius T., Carciofi A.C., Martayan C., 2013, A&AR 21, 69

Rodi J., Natalucci L., Fiocchi M., 2024, A&A 689, A186

Roming P.W.A., Kennedy T.E., Mason K.O., et al., 2005, Space Sci. Rev. 120, 95

Rosenberg F.D., Eyles C.J., Skinner G.K., Willmore A.P., 1975, Nature 256, 628

Rouco Escorial A., van den Eijnden J., Wijnands R., 2018, A&A 620, L13

Rykoff E.S., Miller J.M., Steeghs D., Torres M.A.P., 2007, ApJ 666, 1129

Sartore N., Jourdain E., Roques J.P., 2015, ApJ 806, 193

Schödel R., Ott T., Genzel R., et al., 2002, Nature 419, 694

Semena A., Doroshenko V., Arefiev V., et al., 2021, ATel 14357

Serino M., Negoro H., Nakajima M., et al., 2022, ATel 15442

Seward F.D., Charles P.A., 1995, Exploring the X-Ray Universe, Cambridge University Press

Shapiro S.L., Salpeter E.E., 1975, ApJ 198, 671

Shidatsu M., Pike S., Mihara T., et al., 2022, ATel 15495

Shrader C.R., Sutaria F.K., Singh K.P., Macomb D.J., 1999, ApJ 512, 920

Skrutskie M.F., Cutri R.M., Stiening R., et al., 2006, AJ 131, 1163

Sokolova-Lapa E., 2023, Ph.D. thesis, Friedrich-Alexander-Universität Erlangen-Nürnberg

Sokolova-Lapa E., Gornostaev M., Wilms J., et al., 2021, A&A 651, A12

Sokolova-Lapa E., Stierhof J., Dauser T., Wilms J., 2023a, A&A 674, L2

Sokolova-Lapa E., Zalot N., Stierhof J., et al., 2023b, ATel 16171

Staubert R., Shakura N.I., Postnov K., et al., 2007, A&A 465, L25

Staubert R., Trümper J., Kendziorra E., et al., 2019, A&A 622, A61

Stella L., White N.E., Rosner R., 1986, ApJ 308, 669

Stephenson F.R., Green D.A., 2003, J. Astron. Hist. Herit. 6, 46

Stollberg M.T., Finger M.H., Wilson R.B., et al., 1993, IAU Circ. 5836

Strüder L., Briel U., Dennerl K., et al., 2001, A&A 365, L18

Sunyaev R.A., Titarchuk L.G., 1980, A&A 86, 121

Tanaka Y., 1986, In: Mihalas D., Winkler K.H.A. (eds.) Radiation Hydrodynamics in Stars and Compact Objects, Vol. 255. Lecture Notes in Physics, Springer Berlin, Heidelberg, p. 198

Tauris T.M., van den Heuvel E.P.J., 2006, Formation and Evolution of Compact Stellar X-ray Sources. In: Lewin W., van der Klis M. (eds.) Compact Stellar X-ray Sources, Vol. 39. Cambridge Astrophysics Series, Cambridge, p.623

Tauris T.M., van den Heuvel E.P.J., 2023, Physics of Binary Star Evolution. From Stars to X-ray Binaries and Gravitational Wave Sources, Princeton Series in Astrophysics, Princeton University Press, New Jersey

Thalhammer P., Ballhausen R., Sokolova-Lapa E., et al., 2024, A&A 688, A213

Titarchuk L., 1994, ApJ 434, 570

Tsygankov S.S., Doroshenko V., Mushtukov A.A., et al., 2019a, MNRAS 487, L30

Tsygankov S.S., Doroshenko V., Mushtukov A.A., et al., 2019b, A&A 621, A134

Tsygankov S.S., Doroshenko V., Mushtukov A.A., et al., 2023, A&A 675, A48

Tsygankov S.S., Doroshenko V., Poutanen J., et al., 2022, ApJ 941, L14

Tsygankov S.S., Mushtukov A.A., Suleimanov V.F., et al., 2017, A&A 608, A17

Tsygankov S.S., Rouco Escorial A., Suleimanov V.F., et al., 2019c, MNRAS 483, L144

Turner M.J.L., Abbey A., Arnaud M., et al., 2001, A&A 365, L27

Ulmer M.P., Baity W.A., Wheaton W.A., Peterson L.E., 1973, AJ 184, L117

Vybornov V., Klochkov D., Gornostaev M., et al., 2017, A&A 601, A126

Walter R., Lutovinov A.A., Bozzo E., Tsygankov S.S., 2015, A&AR 23, 2

Weisskopf M.C., Tananbaum H.D., Van Speybroeck L.P., O'Dell S.L., 2000, In: Truemper J.E., Aschenbach B. (eds.) Proceedings of SPIE, Vol. 4012., p.2

Werner W., 1977, Appl. Opt. 16, 764

White N.E., Mason K.O., Sanford P.W., Murdin P., 1976, MNRAS 176, 201

Wik D.R., Hornstrup A., Molendi S., et al., 2014, ApJ 792, 48

Willingale R., Starling R.L.C., Beardmore A.P., et al., 2013, MNRAS 431, 394

Wilms J., Allen A., McCray R., 2000, ApJ 542, 914

Wilms J., Nowak M.A., Pottschmidt K., et al., 2006, A&A 447, 245

Wilson R.B., Harmon B.A., Fishman G.J., et al., 1994, In: Holt S., Day C.S. (eds.) The Evolution of X-ray Binaries, Vol. 308. AIP Conference Proceedings, American Institute of Physics Press, p. 451

Wolff M.T., Becker P.A., Gottlieb A.M., et al., 2016, ApJ 831, 194

Woosley S.E., Heger A., Weaver T.A., 2002, Rev. Mod. Phys. 74, 1015

Yakovlev D.G., Haensel P., Baym G., Pethick C., 2013, Physics Uspekhi 56, 289

Yamamoto T., Nakajima M., Yamaoka K., et al., 2010, ATel 3070

Yamamoto T., Sugizaki M., Mihara T., et al., 2011, Publ Astron Soc Jpn 63, S751

Yamaoka K., Nakahira S., Negoro H., et al., 2010, ATel 2959

Yatabe F., Makishima K., Mihara T., et al., 2018, Publ Astron Soc Jpn 70, 89

Zalot N., Sokolova-Lapa E., Stierhof J., et al., 2024, A&A 686, A95

Zaznobin I.A., Sazonov S.Yu., Mereminskiy I.A., et al., 2022, ATel 15582

Zel'dovich Ya.B., Shakura N.I., 1969, Soviet Astronomy 13, 175

A | Luminosity comparisons to other works

In this appendix, I briefly comment on discrepancies between the here determined X-ray luminosities and those from other works. A0535+26 here serves an example for this comparison as it is both analyzed in this work as well as previously by Tsygankov et al. (2019a). At first glance, the luminosity determined here, $1.39 \times 10^{34}\,\mathrm{erg\,s^{-1}}$, is lower by 70% in comparison to the value determined by Tsygankov et al. (2019a) of $\sim 7 \times 10^{34}\,\mathrm{erg\,s^{-1}}$. This discrepancy becomes even more puzzling when considering that both works obtain a statistically acceptable description of the X-ray spectrum ($\chi^2_{\mathrm{red}} = 1.22$ here and $\chi^2_{\mathrm{red}} = 0.96$ in Tsygankov et al., 2019a).

In this appendix, I will briefly outline how luminosities are calculated and which differing assumptions in the process affect the obtained values.

The X-ray spectrum and its modeling

In their work, Tsygankov et al. (2019a) model the 3.5–79 keV X-ray spectrum of A0535+26 with two Comptonizing plasma components (`comptt`, see Titarchuk, 1994) and also take the Fe $K\alpha$ line emission as well as cyclotron resonant scattering feature at ∼45 keV into account. In this work however, I restrict to modeling the thermal hump and the *red wing* of the nonthermal component. I consequently restrict the spectral range to 3.5–40 keV and do *not* account for a cyclotron resonant scattering feature. This seemingly minor difference can have drastic effects on the obtained luminosity: whereas the model in this work sharply drops off above 40 keV, Tsygankov et al.'s spectral model includes strong emission at energies exceeding the cyclotron line energy. This becomes especially evident in their Fig. 1 and in the here reproduced Fig. 2.6, red and blue data points.

The energy range

The X-ray luminosity is computed as

$$\mathcal{L} = 4\pi D^2 \cdot \int_{E_{\mathrm{min}}}^{E_{\mathrm{max}}} E \times S(E)\mathrm{d}E, \tag{A.1}$$

where D is the distance to the source, $E_{\mathrm{min/max}}$ are the lower and upper bound of the luminosity energy range and $S(E)$ is the photon flux. As the distance enters the above equation quadratically, the luminosity is highly sensitive to it. For all sources considered in this work, I make use of the photogeometric distance as computed by Bailer-Jones et al. (2021) based on *Gaia* data (Gaia Collaboration, 2016, 2023). For A0535+26 one finds a value of $1.77^{+0.07}_{-0.06}$ kpc. Tsygankov et al. (2019a) on the other hand use a distance of 2 kpc. This seemingly minor difference has a large effect: using a distance of 2 kpc instead of 1.77 kpc systematically increases the obtained luminosity by 27%.

Naturally, increasing the energy interval over which the luminosity is computed increases it, especially the inclusion of high-energy radiation up to ~100 keV can alter the obtained value significantly due to its high contribution in the integral. For example, the `doublehump` fit to A0535+26 evaluated from 0.5–100 keV yields a luminosity of 1.89×10^{34} erg s^{-1}, which is 35% higher than the value obtained for the 5–50 keV interval.

Tsygankov et al. (2019a) state a flux level of 1.4×10^{-10} erg s^{-1} cm^{-2} for their spectral model in the 0.5–100 keV range, which corresponds to a luminosity of 6.7×10^{34} erg s^{-1} assuming a distance of 2 kpc.

Further assumptions

The estimated X-ray luminosity further depends on the reference frame used. By modeling *observed* spectra, one is naturally inclined to give the X-ray luminosity also in the observer's frame. To convert the X-ray luminosity to the neutron star's rest frame, the gravitational redshift, time dilatation and surface magnification have to be taken into account, which increases the luminosity by a factor of $(1 + z)^4$, where $z = 0.24$ for neutron stars with $M = 1.4M_\odot$ and $R = 12$ km.

Furthermore, the X-ray luminosity can be given as the actual observed and absorbed luminosity or as the un-absorbed luminosity, which can be obtained by removing the absorption component from the spectral model prior to calculating the luminosity. For A0535+26 this effect is expected to be nearly negligible, as the Galactic absorption column density utilized in this work of 0.44×10^{22} cm^{-2} and the value obtained by Tsygankov et al. (2019a) of 0.08×10^{22} cm^{-2} are both low in comparison and the spectra are therefore understood to be only weakly absorbed.

Comparison

In order to show that the here obtained luminosity is not in disagreement with the higher value found by Tsygankov et al. (2019a), I reproduce their spectral model. Differences in normalisation and detector cross-calibration constants are expected due to different extraction regions. For this exercise I also employ the optimal rebinning routine by Kaastra & Bleeker (2016) and use the W-statistic as fit statistic. I obtain a statistically acceptable description with $\chi^2/\mathrm{d.o.f.} = 670/590 = 1.14$ and an unusually deep cyclotron line with optical depth of 3.2. Assuming a distance of 2 kpc, I obtain an absorbed X-ray luminosity of 3.8×10^{34} erg s^{-1} in the 0.5–100 keV range. Evaluating this model over the energy range of 5–50 keV and assuming a distance of 1.77 kpc, the absorbed luminosity is on the order of 1.35×10^{34} erg s^{-1}, which is very close to the value obtained in this work with the `doublehump` spectral model of 1.39×10^{34} erg s^{-1}.

In this appendix, I have shown that the luminosity derived from a spectral model depends on multiple different parameters and assumptions, which should ideally be given wherever luminosities are stated. I have further shown that the apparent discrepancy of the luminosity in A0535+26 between this work and Tsygankov et al. (2019a) is primarily based on different assumptions and input values. When using the same method to calculate the luminosity, both spectral models give nearly identical results.

Acknowledgments

I thank all the great people who have the past three years at the Remeis observatory so exceptional and enjobable.

First and foremost, I thank **Jörn Wilms** for giving me the opportunity to study and work at the Dr. Karl Remeis-Observatory for the past three years and his advice on this work as well as the paper on GX 301−2.

Furthermore, I thank **Ekaterina Sokolova-Lapa** for her advice both on this thesis as well as the paper on GX 301−2 and for introducing me to accreting X-ray binaries in quiescence.

I am grateful to all members of the *Zoom for Advancing the Link between Observation and Theory* meeting. I thank **Katja Pottschmidt** for her helpful advice and guidance on the GX 301−2 paper and all things *NuSTAR*, **Ralf Ballhausen** for providing the me with the opportunity to work on this peculiar source in the first place and his help over the years, **Aafia Zainab** for her valued help on both physics and language endeavours, **Jakob Stierhof** for his aid in solving countless coding problems, critical view and out-of-the-box thinking, **Philipp Thalhammer** for his patient answers to my many questions, however trivial they may have been, **Katrin Berger** for many valuable conversations and discussions of our two papers, and to **Deniz Demirci** for the productive collaboration Cepheus X-4.

The Remeis observatory is a great place to study and work because of the amazing people that work there. Specifically, I thank **Aafia Zainab** and **Philipp Thalhammer** for all the four trips to Seven Hills and fun times. I thank **Amy Joyce** for a great time in Karlovy Vary, **Florian Steynberg** for countless interesting discussions in our shared office, **Ingo Kreykenbohm** and **Philipp Weber** for keeping everything running, **Steven Hämmerich** for a steady supply of coffee and all the memes, **Caro Collischon** and **Shruti Tripathi** for keeping me company in the republic, and **Martin Mayer** for all the memes and scientific advice.

I thank the **radio lab team** for the team effort to keep the radio telescope operational and all the shared pain over the errors we encountered.

I further extend my gratitude to the **XMAG collaboration** for many productive discussions and comments on my work; in particular **Peter Kretschmar**, **Felix Fürst**, **Nazma Islam**, **Camille Diez**, **Richard Rothschild**, and **Christian Malacaria**, with whom I had the pleasure to collaborate on my paper on GX 301−2.

I am very grateful to **Amy Joyce**, **Ekaterina Sokolova-Lapa**, **Jakob Stierhof**, **Philipp Thalhammer**, and **Aafia Zainab**, for giving me feedback and comments on the manuscript, which improved its content.

To my lab course partner **Simon Hillmann** I am grateful for his company and the many mostly enjoyable hours we spent in the laboratory. Also, I thank **Isabella Probst** and **Lisa Fischer** for the fun times we shared inside and outside of lecture halls! **Jonathan Fleischmann**, I thank you for accompanying me to football matches at subzero temperatures and for being an generous host and great friend.

I am thankful to have had the chance to take part in an excursion to the CERN experiment in Geneva, which was generously funded by the **Department of Physics** at **FAU**.

As a part of the Deutschlandstipendium, **d-fine** supported me during my studies, for which I am truly grateful. I especially want to acknowledge the support by **Lioba Jungk** and **Dr. Tino Schulz**.

I am further grateful for the support of my family and friends, my father **Thomas Wrobel**, who got me interested in computers and technology many years ago, my mother **Elisabeth Zalot**, who shares my passion and excitement for astronomy, and my sister **Katharina Zalot**, for motivating me to start running again and her support. Ein ganz besonderer Dank gilt meiner Großmutter **Theresia Zalot**. I further thank **Saskia Vollhardt**, for everything.

This research has made use of a collection of ISIS functions (ISISscripts) provided by ECAP/Remeis observatory and MIT (`http://www.sternwarte.uni-erlangen.de/isis/`), the Astrophysics Data System, funded by NASA under Cooperative Agreement 80NSSC21M00561, data and software provided by the High Energy Astrophysics Science Archive Research Center (HEASARC), which is a service of the Astrophysics Science Division at NASA/GSFC and the `sltikz` plotting package developed by Jörn Wilms. This work has made use of data from the European Space Agency (ESA) mission *Gaia* (`https://www.cosmos.esa.int/gaia`), processed by the *Gaia* Data Processing and Analysis Consortium (DPAC, `https://www.cosmos.esa.int/web/gaia/dpac/consortium`). Funding for the DPAC has been provided by national institutions, in particular the institutions participating in the *Gaia* Multilateral Agreement.

Statutory declaration

I declare that I have written the present work and conducted the research for it myself. I have not used sources or means without declaration in the text.

Erlangen, October 20, 2024

Nicolas Zalot